Breakage mechanics in large granular flow problems

by

Chunshun Zhang



THE UNIVERSITY OF SYDNEY

A thesis submitted for the degree of Doctor of Philosophy
at The University of Sydney

2012

Abstract

This thesis makes a first attempt to tackle large granular flow problems with grain crushing within a continuum mechanics framework. That is, a special finite element (FE) technique, the Eulerian method, is employed to allow the modelling of granular materials to flow through fixed meshes. The flowing materials are modelled using a linear elastic breakage model, which is derived from the continuum breakage mechanics theory (Einav 2007a, b). This enables the macroscopic behaviour of the flowing materials to be captured, in association with the evolving grain size distribution (GSD).

Two typical granular flow processes are studied: crushable granular materials displacing around a penetrating pile during installation, and mineral materials flowing through a roller mill. The former aims to study the pile end-bearing capacity at steady state penetration; while the latter focuses on the energy-size reduction relationship in mineral comminution. In addition, a cavity expansion process in a brittle granular medium is also studied, with an emphasis on the eventual dissipation of fluid in petroleum application.

The study highlights the fundamental connection between micro-structure and mechanics of brittle granular materials. It is demonstrated that tracking the evolution of the GSD can be useful in the continuum modelling of many applications, which is currently missing out from most existing studies. As a result of this research, a new formula to better predict the end-bearing capacity of piles is proposed and compared with previous equations. Another finding is the derivation of a correlation between the evolving GSD and permeability reduction during undrained cavity expansions. This is followed by establishing a relationship between generation/dissipation of excess pore pressures and grain crushing. Finally, the approach of this thesis is shown to enable us to find optimum roller gaps, which represent the maximum area of new surface to be created with the minimum level of work input; and the influence of increasing grinding speeds on new surface area creation.

Acknowledgement

My deepest gratitude goes to my supervisor, Prof. Itai Einav and Dr Giang Dinh Nguyen for sparking my interest in scientific research and for their invaluable supervision, encouragements, and guidance during my study at University of Sydney. I deeply appreciate all their patience, time, ideas, and funding to make my Ph.D. experience productive and stimulating, without which this thesis could not have been done.

Special thanks to Prof. Harry Poulos for introducing me to Itai when I was looking for a PhD position; also for Harry's care over the period of my PhD study; to Prof. David Airey for explaining me some fundamental soil mechanics problems; to Mr. Ross Barker and Mr. Antonio Reyno for their assistance in my Lab tutorial class; to Mr Rob Ashton for his careful proof reading for whole thesis.

I am also very grateful to work with Dr Pierre Rognon, Dr Yixiang Gan , Dr Irene Guiamatsia, Dr Rachel Gelet and Dr Ben-Nun Oded for their kind help and concern for my study and life.

I am grateful for time spent with my friends in the basement and blue room: Arghya Das, Shiao Huey Chow, Yahya Nazhat, Fahim Nawroz Tonmoy, Farzad Meysami Azad, Shakera Khan, Benjy Marks, Tom Miller, Faham Tahmasebinia, Rakesh Khanal, Gareth Huxham, Shabnam Shayan, Charles Loo Chin Moy, Sally Williams, Mohsen Masoudian Saadabad, Mohammad Mojtahedi, Seyed Yaser Banihashemi Chaharom, Alexander Soo, Zhenyu Eric Yao, Niu Shuang, Xi (David) Zhang, Chongda Wu, Li Ling, Yongling Zhao, and Geng Yue. I really appreciate our wonderful friendship.

Thank also to my parents for their love and encouragement during the course of my PhD study. Their unconditional supports throughout my life give me greatest strengthen to overcome life's challenges.

Finally, a big thank you to my loving and patient wife Rong Hu whose understanding and faithful support during the stage of this PhD is so appreciated.

Publications related to this thesis

1) Zhang, C.S., Einav, I and Nguyen, G. D. (2011). "A study of grain crushing around penetrating piles using a micromechanics-based continuum model". *The Second International Symposium on Computational Geomechanics (ComGeo II)*, Pietruszczak and Pande eds., Cavtat-Dubrovnik, pp. 714-720.
2) Zhang, C.S., Nguyen, G. D., and Einav, I. (2010). "Steady state permeability profiles surrounding penetrating piles in crushable granular media." *Proceedings of the international symposium on Geomechanics and Geotechnics: From Micro to Macro*, Jiang et al., eds., Shanghai, pp. 789-795.
3) Zhang, C. S., Nguyen, G. D., and Einav, I. (2012). "The end bearing capacity of piles penetrating into crushable soils." *Geotechnique*, In Press.
4) Zhang, C. S., Nguyen, G. D., and Einav, I. (2012). "Extracting relationships of energy-size reduction in comminution using continuum mechanics principles." *International Journal of Mineral Processing*, submitted.
5) Zhang, C. S., Nguyen, G. D., and Einav, I. "Hydro-mechanical response of expanding cavities in crushable granular soils: an analysis using breakage mechanics." To be submitted.

Table of content

Chapter I - Introduction

1. Background 1

2. Aim and scope of the dissertation 2

3. Organisation of the dissertation 3

Chapter II - Review of the literature

1 Introduction 5

2 Grain crushing in geotechnical engineering: Mechanical and hydraulic responses ... 7

2.1 Pile end-bearing capacity in crushable soils 8

2.1.1 The significance of grain crushing in pile foundation design 8

2.1.2 Experimental study 9

2.1.3 Theoretical research 11

2.2 Permeability and excess pore pressure in brittle granular soils 12

3 Grain comminution in the mining industry: Energy–size relationship 14

3.1 Classical grinding laws 15

3.2 Advanced grinding models 17

3.2.1 Charles model 17

3.2.2 Models based on the population balance principle 18

3.2.3 Models derived from energy dissipation assumptions 20

3.3 Discussion 21

4 Models for granular crushing 22

4.1 Continuum modelling of granular materials 22

4.2 Importance of GSD 23

4.3 Evolution of GSD 25

4.4 Breakage index 28
4.5 Breakage mechanics theory and models 28
5 Computational methods in large deformation problems 29

Chapter III - Continuum breakage mechanics: Review of theory and models

1 Introduction 31
2 Breakage 32
3 Statistical homogenisation 34
4 Energy split hypothesis 35
5 Thermodynamic formulation of breakage mechanics 37
5.1 Energy balance equation 37
5.2 Breakage energy and residual breakage energy 39
5.3 Breakage growth assumption 40
5.4 Yield functions 40
5.4.1 Breakage yield function in an elastic-breakage model 40
5.4.2 Coupled yield function 41
6 Models developed from breakage mechanics theory 43
6.1 Breakage model based on linear elasticity (i.e., linear elastic breakage model) 43
6.2 Breakage model based on pressure-dependent elasticity 45
6.3 Breakage model for unsaturated granular materials 48
6.4 Breakage model based on large strain deformation 49
6.5 Mixture breakage model 50
6.6 Current development of a breakage model with cementation 50
6.7 Discussion 50
7 Summary 52

Chapter IV - Finite element numerical implementation of the linear elastic breakage model

1 Introduction 54
2 Brief review of stress return algorithm 55

3 Finite element implementation 56

4 Tangent stiffness matrix 59

5 Verification of implementations 61

5.1 Isotropic loading condition 62
5.2 Isotropic loading-unloading-reloading condition 63
5.3 Conventional drained loading with constant confining pressure 64
5.4 Conventional undrained loading with constant confining pressure 65
5.5 Accuracy verification 65

6 Model prediction 66

7 Summary 68

Chapter V - End-bearing capacity of pile into crushable soils

1 Introduction 69

2 Analysis of cone-ended model pile test 71

3 Analysis of pile penetration 75

4 A new formula for end-bearing capacity factor 79

5 Summary 85

Appendix V-1 86

Chapter VI - Hydro-mechanical response of expanding cavities in crushable granular soils

1 Introduction 88

2 Permeability reduction using breakage mechanics 90

3 Finite Element model for cylindrical cavity expansion 92

4 Exploration in stage I: Cavity expansion 94

4.1 Variations of stress and excess pore pressure during expansion 94
4.2 Generation of maximum pore pressure at the cavity interface 96

5 Exploration in stage II: Consolidation 97

5.1 Variations of stress and excess pore pressure during dissipation 97
5.2 Dissipation of maximum pore pressure at the cavity interface 102

6 Summary 104

Chapter VII - Extracting relationships of energy-size reduction in comminution using continuum mechanics principles

1 Introduction 105

2 FEA of comminution of granular materials in a roller mill 107

3 Interpretation of numerical results 109

4 Results of product cumulative GSD and assumed moment (rotation) work 111

5 Exploration of energy-size reduction relationship 114

6 Conclusions 116

Chapter VIII - Summary and further research

1. Summary 118

1.1 End-bearing capacities of piles in crushable soils 118

1.2 Generation and dissipation of excess pore pressure in cavity expansion 119

1.3 The energy-size reduction relationship in comminution in a roller mill 120

2. Further research 121

2.1 Enhancements in the model behaviour 121

2.2 Engineering application aspects 122

References 125

Appendix A 146

Chapter I

Introduction

1. Background

Grain crushing is associated with various granular processes, e.g. surrounding pile penetration in crushable soils, mineral engineering, deformation of fault gouges, etc. While the main concern in various disciplines might be different (e.g., bearing capacity and permeability reduction in geomechanics, energy efficiency in mineral engineering, and the budget of energy flow and generation in earthquakes), all share one unique feature: the evolution of grain size distribution (GSD). The study of any of the above processes would benefit greatly by making the evolution of grain size distribution an intrinsic feature of the models used. This issue is usually overlooked in the literature.

A rigorous way to integrate the grain size distribution (GSD) into a continuum constitutive relationship, in order to study the grain crushing process, has been developed by Einav (2007a, b) in his 'breakage mechanics theory'. This theory was formulated with recourse to the micromechanics of grain crushing, resulting in good quantitative and qualitative estimates of both the macroscopic behaviour and microstructural changes of crushable granular material (see Chapter III). In addition, the fact that the breakage mechanics theory was formulated within the rigorous confinement of thermodynamics makes all derived models thermodynamically consistent. One of those models, the 'linear elastic breakage model', is employed in this thesis.

The linear elastic breakage model has been implemented into finite element (FE) codes (see Chapter IV), targeting large deformation problems where materials can flow. For instance, in Chapter V, the large pile penetration process is modelled by allowing granular materials to flow around piles, such that a steady state of pile

penetration could be numerically achieved. The other application, studied in Chapter VII, is where modelled quartz sands flow through a roller mill, subject to comminution. It is worth noting that the above-mentioned FE simulations are based on the so-called Eulerian method that allows material to flow through the meshes that stay fixed in space. In addition, the thesis also analyses the permeability reduction and excess pore pressures surrounding expanding cavities in brittle granular materials in Chapter VI for completeness of the research purpose.

2. Aim and scope of the dissertation

The aim of this thesis is to analyse various granular flow processes involving grain crushing by using the breakage mechanics theory and large FE techniques.

The first part focuses on the correlation between crushability and pile end-bearing capacity in crushable soils. It has been widely recognised that for crushable soils, the predicted pile capacity—based on conventional theory and limiting design values—may result in unconservative designs. This is because the conventional methods did not incorporate the soil crushability and related factors into the design formulae. In this thesis those factors are taken into account, based on the breakage mechanics theory. Two FE simulation techniques dealing with large deformations are used, i.e., the Arbitrary Lagrangian Eulerian (ALE) and Eulerian methods. The theoretical predictions are compared with experimental observations and a new equation is formulated for predicting the pile end-bearing capacity in crushable granular soils.

The second subject is mainly concerned with variations of excess pore pressure in an instant cavity expansion in brittle granular materials. Due to considerable crushing of brittle particles, the permeability of the medium largely reduces. Consequently, the excess pore pressure increases rapidly and dissipates slowly. These changes are quantified by using a cylindrical cavity expansion, under undrained followed by drained conditions.

The last, but not least focus is the study of the energy-size relationship in comminution. The linear elastic breakage model is used to represent the behaviour of modelled quartz sands in a roller mill. Driven by gravity and the rollers' friction, the modelled sands flow in and out of the space between a pair of rollers. Such a space is

discretised with meshes that are fixed, eliminating the mesh distortion problem usually encountered in small strain FE simulations. This clearly distinguishes itself from the traditional grinding laws, or the population balanced grinding models (PBMs), which largely depend on empirical curve fitting of the experimental data.

3. Organisation of the dissertation

The structure of the thesis is as follows.

Chapter II reviews the existing research about grain crushing. This is followed by a critical assessment that paves the way for suggested new developments.

Chapter III reviews the systematic approach to the development of continuum breakage mechanics. A linear elastic breakage model used in this thesis is also introduced and explained in detail, which provides a sound theoretical basis for the study in this thesis.

Chapter IV elaborates on the FE implementation of the constitutive model used in this study. The implementations are then verified under four different loading paths. This is followed by a series of tests to show the model's capabilities.

Chapter V incorporates the breakage model into the FE simulation of pile foundation. The numerical results are compared favourably to experimental observations in terms of grain crushing distribution around the pile, soil deformation and end-bearing capacities with pile driving. This is followed by a parametric study about various fundamental mechanical soil parameters and the results of a new end-bearing capacity formula that has found to be superior to many existing equations.

Chapter VI focuses on the breaking of crushable granules when subjected to sufficient undrained cavity expansion. The permeability reduction and generation/dissipation of pore pressure at the cavity interface are emphasized, which is quantitatively connected with the granular crushability and related factors .

Chapter VII employs the breakage model to study the mineral comminution in a roller mill. Correspondingly, a FE model of a roller mill is established and the numerical prediction of the product size distribution and the assumed moment work are in good

agreement with experiments. Next, a parametric study is carried out to quantify the connection between the moment work rates and surface production rates.

Chapter VIII highlights the main findings in this thesis, the shortcomings of the current research, and recommendations for further research.

Chapter II

Review of the literature

1 Introduction

The best way to start a new day, for many people, is with a cup of fresh coffee. To get fresh coffee, coffee beans first need to be ground into a fine powder using, for instance, a coffee grinder (Figure 2.1[1]). This is one of the most common examples of the comminution phenomena found in people's daily lives. Another example of the comminution is in a grain-crushing wheel (Figure 2.2[2]) that has been traditionally used to grind wheat, corn, and rice into a floury endosperm. Other examples of comminution include brewing beverages and beers that require finely ground grains.



Figure 2.1 Coffee bean grinder



Figure 2.2 Grain-crushing wheel

Comminution leads to a change in grain size distribution (GSD) over time by processes such as crushing, grinding, shaking, striking, and explosions. It occurs naturally during earthquakes, when parent rocks degrade into granular cataclasite that may be further crushed during the formation of a fault gouge (Figure 2.3, from

1 http://chrisvonada.com/category/breathing-life/page/10/ (access on 14/11/2011)
2 http://www.fotothing.com/rescue193uk/photo/1d421858c59dc728ea2048207ca55a14/ (access on 14/11/2011)

Nguyen and Einav 2009). In the mineral processing industry, size reduction is achieved by grinding coarse granular minerals to produce fine particles, which frees the desired mineral matter from the gangue (for example, the roller mill shown in Figure 2.4[3]). The fine particles produced by this method serve many industrial applications, including cement production.

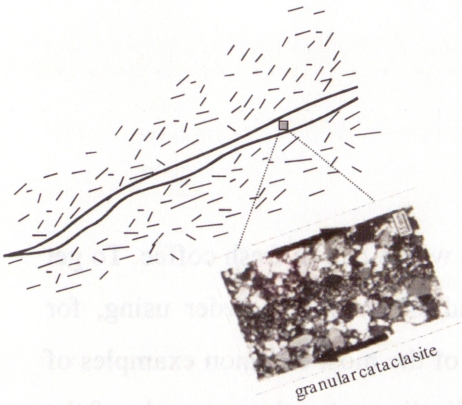

Figure 2.3 Granular cataclasite during earthquake

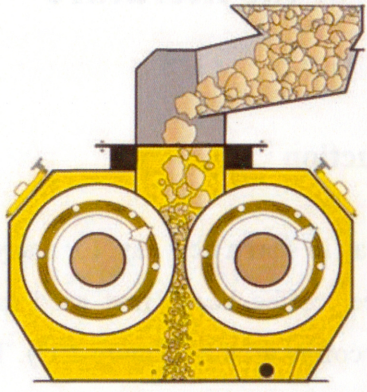

Figure 2.4 Mineral comminution

In geotechnical engineering, grain crushing also confronts foundation designers. A typical problem in foundation design occurs when piles penetrate calcareous or carbonate sediments (Figure 2.5) and large quantities of grains may break as a result. This is due to the weak mineral composition and collapsible structure that make these soils very fragile and easy to crush even under relatively light stresses. While the crushing of grains is typically associated with the presence of weak strata in the soil profile, it is by no means restricted to such soils. Even for relatively hard granular soils, such as silica and quartz sands, if the penetration depth is sufficiently low, these seemingly stiff granular particles may also break under high stresses. Another geotechnical problem of grain crushing is encountered in rockfill dams where grains may break under the high pressure found at the bottom of the dams (Alonso and Cardoso 2010). The rearrangement of particles due to crushing, which is associated with the granule creep behaviour, may increase the deformation (or rate of deformation) of the dam to a greater degree than would otherwise be predicted.

3 http://yufmachine.com/113.html (access on 14/11/2011)

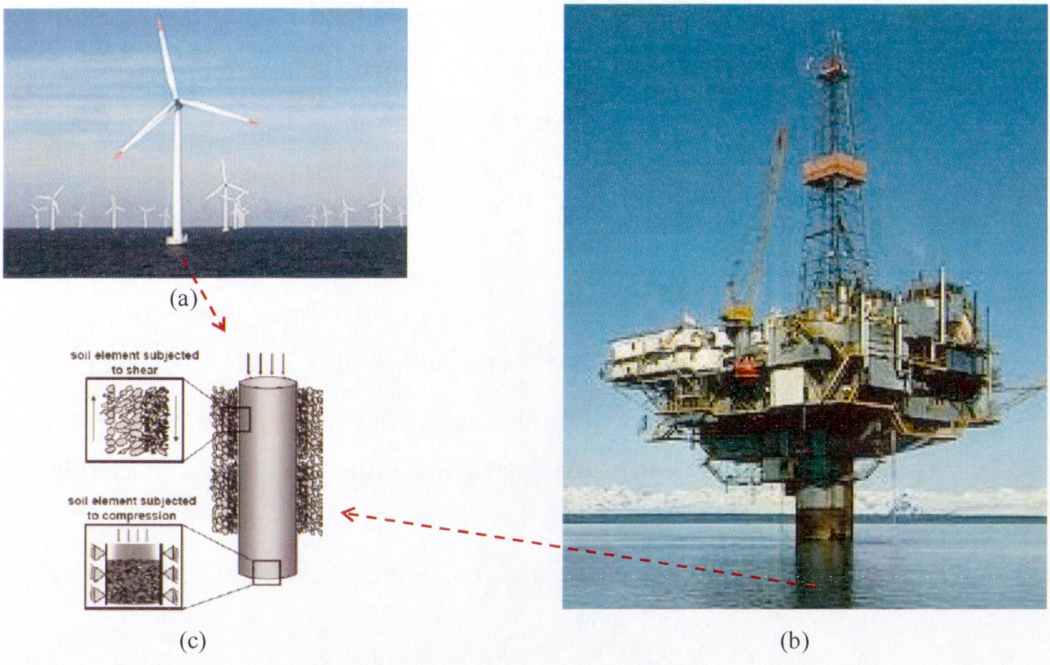

Figure 2.5 (a) Wind turbines[4] and (b) an oil platform built on pile foundations[5] placed on offshore sediments, which could easily be penetrated by a pile as seen in (c) (courtesy of Ben-Nun 2010)

This chapter, a literature review, comprises three main sections. In following Section 2, research on grain crushing in geotechnical problems is reviewed, with an emphasis on pile foundation and cavity expansion in crushable granular materials. In Section 3, investigations on mineral comminution in the mining industry are presented and discussed. In Section 4, constitutive modelling of crushable granules is overviewed and the breakage mechanics theory employed in this thesis will also be briefly introduced.

2 Grain crushing in geotechnical engineering: Mechanical and hydraulic responses

In geotechnical engineering, the macroscopic behaviours have been found to be strongly associated with microstructural changes of the grains constituting the material, i.e. grain crushing (or GSD evolution). This change may affect soil strength, porosity, permeability, and excess pore pressure, etc (e.g., Hardin 1985; Lade et al. 1996; McDowell and Bolton 2000) as well as the performance of structures supported

4 http://www.german-oilgas-expo.com/e-news-eon-wind.html (access on 14/11/2011)
5 http://www.alaska-in-pictures.com/monopod-oil-platform-3221-pictures.html (access on 14/11/2011)

by the soil. For example, soil resistance might not be enough to support the structure loads transmitted through piles when considerable grain crushing is found ahead of the pile tip in crushable soils. For this reason, some pile foundations built in weak offshore sediments collapse during construction (see accident reports from McClelland 1988, and Alba and Audibert 1999).

Grain crushing also results in low permeability and dissipation rates, and high excess pore pressure in the soil (Okada et all. 2004). This may trigger the soil liquefaction that is the cause of many collapses of foundations and slopes (Sassa et al. 1996; Wang and Sassa 2000; Okada et al. 2000). A particular common interest are those sharing the similarities with expanding cavities, such as in situ soil testing, deep foundations, tunnels, underground excavations in soil and rock, and gas- and oil-producing perforations (Yu 2000).

Sections 2.1 and 2.2 will focus on the existing investigations of the influence of grain crushing on these two engineering problems: the pile end-bearing capacity and excess pore pressure behaviour in crushable granular materials.

2.1 Pile end-bearing capacity in crushable soils

2.1.1 The significance of grain crushing in pile foundation design

As a popular foundation form, piles have been widely used in various applications. A particularly common application is in the offshore industry, where piles are built under oil platforms and wind turbines. These piles transmit the structure loads to deep sediments under the sea. However, these sediments may contain a large quantity of shell fragments and high carbonate contents, which are usually very compressible or generally weak. In such easily crushable soils a difficult problem confronting the engineering design is to predict whether the end-bearing capacities of weak sediments are sufficient to resist the vertical loads transmitted by the piles. This problem is becoming more pressing with the rapid introduction of engineering constructions into deep water to explore for oil and to build wind turbines.

Traditional methods of evaluating pile end-bearing capacity in crushable soils have lagged far behind the practice (Poulos and Chua 1985; Golightly and Hyde 1988; Yu

2000): they only considered the friction angle of the soils as an exclusive or primary parameter for evaluating bearing capacity (e.g., Prandtl 1921; Terzaghi 1943; Meyerhof 1963; Vesic 1973). As a result, the higher the friction angle, the higher the end-bearing capacity is supposed to be. This appears to hold when applying traditional equations to predict the pile end-bearing capacity in normal soils consisting of coarse and relatively hard minerals such as quartz. However, in relatively weak soils (i.e. calcareous sand), though with relatively high friction angles, traditional equations usually overestimate pile end-bearing capacity (Angemeer et al. 1973; Poulos 1985; Golightly and Hyde 1988; Randolph 1988; Alba and Audibert 1999; Ohno et al. 1999). Consequently, many offshore pile foundations fail during construction due to the inappropriate use of traditional methods (for example see Alba and Audibert (1999)).

This unusual occurrence (i.e. high friction but low end-bearing capacity) is largely due to granular crushability. Crushable sediments may break due to pile penetration, For example, a pile driving into a typical fragile soil, such as calcareous sand, would cause significant granular crushing within the vicinity of the pile (Klotz and Coop 2001; White and Bolton 2004). This unique feature explains the relatively small end-bearing capacity of crushable soils, whose friction angles are generally high. It is therefore essential to consider granular crushability when estimating pile end-bearing capacity (Yeung and Carter 1989; Yasufuku and Hyde 1995; Alba and Audibert 1999; Kuwajima et al. 2009).

2.1.2 Experimental study

Grain crushability and its effect on engineering design have been extensively studied experimentally, with particular attention given to model pile tests (e.g., Yasufuku and Hyde 1995; McDowell and Bolton 2000; Kuwajima et al. 2009). In McDowell and Bolton's experiments, the ultimate resistance to piles penetration was found to be higher in well-graded soils than in uniformly graded soils. This highlights the direct connection between the GSD and pile end-bearing capacity. This observation appears reasonable since the GSD has been found to greatly influence the strength and stress-strain behaviour of a soil (Hardin 1985; Lade et al. 1996) and naturally affects the end-bearing capacity of a pile, e.g., the peak strength and the ultimate tip resistance are reached at relatively high strains or displacements (Kuwajima et al. 2009).

Another significant consequence of grain crushing is that it causes a high volumetric strain reduction. The volumetric reduction of crushable soils is usually measured through curve fitting of the data by elementary soil tests (e.g., one-dimensional or isotropic compression tests) and is defined as soil compressibility. For comparable tip resistances, such high compressibility in weak soils requires much larger pile displacements than in relatively hard soils (Golightly and Hyde 1988; Kuwajima et al. 2009). To emphasise this, Kuwajima et al. (2009) carried out model pile tests for a carbonate soil and silica sand. They found clear densification and a corresponding contraction in carbonate sand due to broken grains, while for a silica sand some heave occurred in the layers adjacent to the pile without grain crushing. Because of these two distinct failure mechanisms for weak and relatively hard soils, the developments of tip resistance in each case should be different. Thus, employing classical solutions to calculate pile end-bearing capacity in crushable soils is not a valid measure. Similar model pile tests have been studied by a number of other investigators (e.g., Poulos 1985; Semple 1988; Nutt and Houlsby 1991; Yasufuku and Hyde 1995; Alba and Audibert 1999; White and Bolton 2004). Together with those existing model pile tests, two conclusions emerge:

(1) Granular crushability is the main cause of the high compressibility of crushable soils evidenced through the evolution of the GSD;

(2) The resulted high compressibility is the main reason to cause much larger displacements in crushable soils than in normal or relatively hard soils.

It is important to note that while the grain crushing phenomenon is normally associated with the presence of weak soils, it is by no means exclusively restricted to such soils. Relatively hard granular materials, i.e. quartz and silica sands, may also break when they are under sufficiently high pressures in various loading conditions (e.g., Miura and O-hara 1979; Bopp and Lade 1997; Hyodo et al. 1996; Nakata et al. 1999). As an example, a clear shear zone consisting of a considerable quantity of fine broken quartz particles was observed to tightly cover the displaced pile in the experiments by Yang et al. (2010).

2.1.3 Theoretical research

Vesic (1973) presented a pioneering theoretical work regarding the end-bearing capacity of pile driving in loose sands. This work however does not cover crushable soils with evolving GSD. Vesic argued that the slight compressibility was due to the rearrangement of the particles under confining pressures; while for dense soils, the compressibility could be ignored. Based on classical methods, e.g., Prandtl's (1921) equation, Vesic introduced a rigidity index and average volumetric strain in the plastic zone to represent the soil compressibility. As a result, his equations are dependent on the confining pressure (through a relationship with initial vertical stress). Reasonably, his propositions are better than classical ones in end-bearing capacity prediction.

Vesic derived his equations using simple models of cavity expansion rather than employing rigid-plasticity theory as used for the traditional equations by Prandtl (1921) and Terzaghi (1943). This cavity expansion solution was found to be useful in estimating ultimate end-bearing capacity in loose silica sand that may be moderately compressible (Vesic 1977). For crushable soils that are largely compressible, the failure patterns under the pile are observed to be spherical (e.g., Kuwajima et al. 2009). Therefore, the cavity expansion theory may be reasonable to crushable soils. Yasufuku and Hyde (1995) related the pile end-bearing capacity with the cavity expansion pressure by using Vesic's solution. Their proposed equation requires the introduction of a so-called secant friction angle in order to capture the observed pressure-dependence of the end bearing capacity; the secant friction however is not a fundamental soil property and therefore cannot explain why the bearing capacity varies with crushability and GSDs.

The cavity expansion theory is also used to interpret the soil tests with grain crushing, such as in the cone penetration test (CPT) and pressuremeter test (PMT). For instance, Russell and Khalili (2002) found in their numerical simulation a reduction in the void ratio and limiting stress and radial stress at the cavity wall due to grain crushing. Regardless of the merit and some successful applications of cavity expansion theory, no result to date can predict the influence of the GSD (or grain sizes) in altering the end-bearing capacity of piles in crushable soils.

The end-bearing capacity of piles has also been tackled with critical state soil mechanics (CSSM) models, the concept of which originated from clay behaviour. When these models are applied to describe the sand behaviours, their essential parameters λ (particular fitted slope) and yield transition become largely dependent on curve-fittings from extensive laboratory testing. In addition, the CSSM models are very sensitive to microstructural changes of the grains due to the lack of physical connection of these models to the actual material. For instance, altering the initial GSD of the sand means that the whole set of parameters would need to be altered. On this basis, it is clear that CSSM models, while useful, are limited to the choice of unique tests and load paths in hand. In short, they lack predictive capabilities with respect to the evolution of the GSD.

2.2 Permeability and excess pore pressure in brittle granular soils

Permeability reduction and excess pore pressure generation due to grain crushing are important concerns in various designs and constructions. In this context the evolving GSD may lead to the increase of specific surface and/or the loss of porosity of the granular ensemble. Particularly in undrained conditions where there is no porosity reduction, since the specific surface of the sample still increases as the GSD evolves, the local permeability reduces. This generates excess pore pressure which dissipates slowly (Okada et al. 2004). An adverse impact is soil liquefaction, which is of particular importance in many failures of foundations and slopes (Sassa et al. 1996; Wang and Sassa 2000; Okada et al. 2000). Therefore, a good understanding of the correlation between grain crushing, permeability and excess pore pressure is important for the understanding of liquefaction failures in various engineering applications. Of particular interest are those sharing the similarities with cavities expansion problems, such as in situ soil testing, deep foundations, tunnels, underground excavations in soil and rock, and gas- and oil-producing perforations (Yu 2000).

Some experiments have been conducted to study the influence of grain crushing on permeability reduction. Zhu and Wong (1997) compressed sandstone, at different effective confining pressures, to measure permeability. They found that permeability decreased by up to more than three orders of magnitude. A recent ring shear test result was reported by Okada et al. (2004) in terms of two samples of a fine silica sand and

Osaka-group coarse sandy soil (i.e. a Japanese crushable sand). Their results quantified the influence of grain crushing in decreasing permeability and generating excess pore pressure. In detail, the level of permeability was found to decrease by around two orders of magnitude for silica sand samples, and by up to four orders of magnitude for the Osaka-group coarse sandy soil where much more grain crushing occurred, viz., the broken sand behaves similarly to typical clay as the fine size of fragments dramatically reduces the permeability (e.g. 10^{-9} m/s for clay (Purushothama Raj 2008)). This results in a much greater excess pore pressure with a slower dissipation rate than in the virgin, unbroken silica sand.

Many theoretical formulae have been proposed to find the connection between the permeability and various grain sizes. Hazen (1892) proposed an empirical formula (probably the first) to link the permeability, k to the grain size, D_{10} (a grain size for which 10% of the grains by mass are finer) using an empirical coefficient, c:

$$k = cD_{10}^2 \tag{2.1}$$

Equation (2.1) was later slightly modified based on statistical power regression analyses on 19 sets of published data (Shepherd 1989):

$$k = cD_{10}^{1.65 \text{ to } 1.85} \tag{2.2}$$

Other forms have been suggested. For instance, Sperry and Peirce (1995) developed a linear model to estimate permeability based on the grain size of D_{50} (grain size for which 50% of the grains by mass is finer). Alyamani and Şen (1993) used both D_{10} and D_{50} (grain size for which 50% of the grains by mass is finer) in their equation. A highly effective and popular form is to adopt the Kozeny-Carman (Matyka et al. 2008) equation:

$$k = c_0 \frac{n^3}{T^2 S^2} \tag{2.3}$$

In the above c_0 is a constant; $T = T(n)$ is the tortuosity as a function of the porosity n; S is the specific surface area of the grains, which can be represented by the GSD.

Nevertheless, further study is required to link the grain sizes and the soil permeability to the mechanical/hydraulic responses. An example was proposed by Papamichos et al. (1993). Its aim was to analyse the inter-granular stresses for estimating the local permeability reduction, which is dependent on a single size of D_{50}. Instead of a single size, more recently Einav et al. (2011) used an entire evolving GSD to predict the permeability reduction and granular mechanics of stresses and strains. Their methodology is based on "breakage mechanics" with a breakage model (Einav 2007a, b), together with the solution of the cavity expansion theory. The validation shows their proposed closed-form solution is identical to finite element numerical results, highlighting the superior performance of such a mechanical approach to other existing models.

3 Grain comminution in the mining industry: Energy–size relationship

In mineral comminution, the relationship between energy and size reduction is always an important initial consideration as the particle comminution is highly expensive in energy consumption. More than half of the energy expended by the cement industry and mineral processing plants was reported to be associated with size reduction operations. However, less than 10% of that energy is associated with the comminution of the materials (Tavares and King 1998).

Extensive surveys have been carried out to explore this relationship, mostly in ball mills and roller mills (e.g., Dutkiewicz et al. 1986; Seebach 1987; Schönert 1988; Fuerstenau et al. 1991; De 1995; Sander 1999; Abouzeid and Fuerstenau 2000; Abouzeid and Fuerstenau 2009; Morrell 2010; Farber et al. 2011; Benzer et al. 2011; Bitra et al. 2009). Taking a roller mill for example, the product size distribution usually possesses a self-similar form, such that log mean size decreases linearly with the amount of fines generated and the inverse of the median size increases directly with energy input (e.g., Fuerstenau et al. 1991; De 1995). Interestingly, the mean size, D_{50}, has also been widely adopted as a specific measurement in energy–size relationship (e.g., Campbell et al. 2001; Stamboliadis 2007). To fit the self-similarity behaviour of the GSD curve, several mathematical solutions are proposed, among which the famous ones are Rosin–Ramler (R–R) and Gate–Gaudin–Schuhmann

(GGS). However, they all fail to calculate the specific surface area of the product materials because there is no minimum size in their formulae (Stamboliadis 2007). As a result, the surface area becomes very large and tends to infinity as the size approaches zero.

To explain and predict the complex relationship of size reduction and energy, an appropriate grinding model is required. Different models have been developed ever since Rittinger's (1867) theory of comminution was published. Generally, these existing models may be classified in two ways: classical, and advanced grinding models. Classical models deal only with the energy required to break a single particle into a smaller size. Advanced models incorporate the GSD of the comminution products to the energy consumed. Sections 3.1 and 3.2 will review the existing models. This is followed by a critical assessment of these models in Section 3.3.

3.1 Classical grinding laws

The first grinding law is that proposed by Rittinger (1867), which has been called the first law of comminution. Rittinger stated that the energy consumed is proportional to the new surface created:

$$E_R = C_R\left(\frac{1}{D_p} - \frac{1}{D_f}\right) \tag{2.4}$$

where E_R is the specific energy (energy per unit weight or volume) for the size reduction from feeding particle D_f to product one D_p, and C_R is called Rittinger's constant.

Kick (1885) later developed a second law of comminution. Instead of Rittinger's argument of the energy proportional to the new surface created, he claimed that the specific energy required for breakage remain constant. He thereby derived the following type of logarithmic law:

$$E_K = C_K \log\left(\frac{D_f}{D_p}\right) \tag{2.5}$$

The notations have the same meanings as those in (2.4), except that subscript K refers to the name of Kick. However, Kick's statement has been proved to be true only for relatively large particles, as shown in Tavares and King's (1998) experiments. Regarding this limitation, Stamboliadis (2005) recently gave an explanation with regard to energy distribution by surface energy and internal energy. He believed that for large particles the surface energy for elastic deformation of a particle was negligible compared to the internal energy required for breakage. This naturally leads to the conclusion that the specific energy for breakage is a constant. However, for small particles, the surface energy for elastic deformation is reasonably great, or even greater than the internal energy for breakage at some point. In this case, Kick's statement is no longer suitable. Similarly, Rittinger's statement suffers the same limitation as Kick's (Stamboliadis 2004).

Bond (1952) later proposed another relation, called the third law of comminution. He stated that the net energy required is proportional to the total length of the new cracks formed:

$$E_B = C_B\left(\frac{1}{\sqrt{D_p}} - \frac{1}{\sqrt{D_f}}\right) \tag{2.6}$$

Alternatively, in a more general form:

$$E_B = C_B\left(\frac{10}{\sqrt{D_{p80}}} - \frac{10}{\sqrt{D_{f80}}}\right) \tag{2.7}$$

Notations in (2.6-2.7) again have the same meaning as those in (2.4), except the subscript B refers to the name of Bond; and D_{p80} and D_{f80} are the 80% passing size of the product and feed material. Bond's proposition has proven to be more useful than Kick's and Rittinger's models in the ball mill circuits (Stamboliadis 2007), although it is a partial case of Rittinger's statement (Charles 1957). Several modifications or extensions of Bond's equation were later proposed for its application in ball mills (Morrell 2004 and 2006).

It is worth noting that the above three laws of comminution can be summarised using an incremental form (Walker and Shaw 1954):

$$dE = -C\frac{dD}{D^m} \tag{2.8}$$

where C and m are constant and the minus sign denotes the specific energy increases with decreasing sizes. D is a characteristic particle size, being an explicit function of either the surface area or some other parameters of the GSD. Soon after, many researchers (e.g., Charles 1957; Brown et al. 1960; Hukki 1962) showed that the exponent m is actually not a constant but a variable whose value is a function of characteristic particle size, $f(D)$. Li and Xu (1992) employed fractal theory to elaborate on the choice of this function. However, this function is still very empirical with minimal theoretical explanation.

3.2 Advanced grinding models

3.2.1 Charles model

The above mentioned classical models are not related to the size distribution of the comminuted products and deal only with the energy required for single grain breakage. To take into account the size distribution, starting from equation (2.8), Charles (1957) first proposed the well-known energy–size reduction relationship:

$$E = \int_0^{D_{p\max}} dF \int_{D_{f\max}}^{D} \left(-C\frac{dD}{D^m}\right) \tag{2.9}$$

where D_{pmax} and D_{fmax} refer to the product maximum size and feed maximum size respectively. The cumulative grain size distribution function, F, is:

$$F = \left(\frac{D}{D_{p\max}}\right)^{\alpha} \tag{2.10}$$

Thus, the size frequency dF is given by:

$$dF = \alpha\frac{D^{\alpha-1}}{D_{p\max}^{\alpha}}dx \tag{2.11}$$

in which α is the power law parameter. The power law distribution in (2.10) is the so-called GGS which has been widely used in the comminution industry (Kapur 1971;

Stamboliadis 2002). Interestingly, the GGS distribution has the same form as the fractal equation proposed by Turcotte (1986) in describing the ultimate cumulative GSD by mass in earthquake studies of fault gouges.

A problem in Charles's equation is the lack of explanation for the selection ranges of α and m. The detailed explanation of the ranges of α and m are later pointed out by Stamboliadis (2007), in which α is dependent on whether m is equal to 1 or not. Furthermore, some other disadvantages in the derivation of Charles's equation were identified by Kapur (1971), e.g., that the assumption of zero-order rate of breakage of particles is experimentally untenable, which suggests that it is inappropriate to use the Walker and Shaw equation (2.8) for the derivation of Charles's law.

3.2.2 Models based on the population balance principle

More rigorous grinding models were derived based on the principle of population (or mass) balance over particulate entities (Ramkrishna 2000). The population balance principle in mineral comminution can be expressed briefly by stating that the mass of material in a size interval = sum of material broken into the interval from larger sizes + material in the interval initially – material broken out of the interval (Austin 1972; Campbell et al. 2001). From this principle, together with the additional assumption of selection and breakage function, which are related to the energy distribution inside the mills, many grinding models can be derived. These models are called population balance models (PBMs) (e.g., Kapur 1971; Kapur and Fuerstenau 1987; Kapur 1990; Fuerstenau et al. 1991).

A good example of a PBM was given by Kapur (1971) who incorporated the GGS distribution in the population balance equation, deriving a general form of Charles's equation as shown in equation (2.12), in relation to the time as an independent variable:

$$\frac{\mathrm{d}F(D,t)}{\mathrm{d}t} = -S(D,t)F(x,t) + \int_D^{\infty} S(v,t)B(v,D)F(v,t)\mathrm{d}v \qquad (2.12)$$

where $F(x,t)$ is mass fraction of particles of size D at grinding time t. The selection function, $S(D, t)$ implies the rate of breakage of particle size D, and $B(D, t)$, the breakage function, is the mass fraction of product of size D when particles of size v

are broken. Together with the mathematical assumption of $S(D, t)$ and $B(D, t)$, the analytical solution of the equation (2.12) can be worked out. According to Kapur's model, the Charles equation in equation (2.9) is only a particular case without time effect.

It is important to note that equation (2.12) might be suitable for ball and tumbling mills where the size distributions evolve with increasing running grinding time. However for roller mills, with only a limited time for solids to pass through the rollers, the size distribution would be more appropriately formulated with cumulative input energy. Based on this idea, Fuerstenau et al. (1991) derived a different grinding model by modifying the energy dissipation in Kapur's equation. As a result, the time variable was replaced with specific energy input E:

$$\frac{\mathrm{d}F(D,E')}{\mathrm{d}E} = -k^0(D)F(D,E') + \int_D^\infty k^0(v)\frac{\mathrm{d}B(v,D)}{\mathrm{d}x}F(v,E')\mathrm{d}v \qquad (2.13)$$

the notations F and B in the above equation have the same meaning as those in equation (2.12) while E' defines a rescaled energy term of the specific energy input. $k^0(D)$ is the breakage constant normalised with energy input rate. By assuming the forms of $k^0(D)$ and $B(v, D)$, equation (2.13) can be solved analytically.

Regardless of the natural merits of various PBMs in reflecting conservation of distributions, it is usually difficult to determine appropriate selection functions. At present, most selection functions are derived from empirically fitting to the experimental data. If changes to the mill operation occur, e.g., various grinding speeds, the parameters for selection functions might need to be entirely recalibrated. In some cases, such recalibration may results in selection functions incorrect or even meaningless (Austin 1972). Consequently, the breakage functions based on the selection functions would become inappropriate as well.

Campbell et al. (2001) developed a new mathematical relationship between the feed and product GSDs of a roller mill. Their method is to separate elements of the breakage equation into a matrix form by using different size ranges to describe the inlet and outlet GSDs, which removes some of the ambiguity of the election function. From their limited tests, good agreement between the experimental data and predictions were found.

3.2.3 Models derived from energy dissipation assumptions

In addition to the population balance principles, some assumptions regarding energy dissipation are proposed to establish new models. For instance, Stamboliadis (2007) assumed specific surface, s (dimension: m^2/kg) that obeys a power law relationship with the net specific energy, E (dimension: J/kg):

$$s = a \cdot E^n \tag{2.14}$$

with maximum specific surface, s_{max} when n=1 in equation (2.14). he defined the breakage efficiency ratio as $Y = s / s_{\max} = E^{n-1}$. Furthermore, he introduced an energy transmission efficiency of system, f_0 to relate the net energy available for comminution and total energy consumed in the system. Thus the more accurate breakage efficiency is defined as $f = Y \cdot f_0 = E^{n-1} \cdot f_0$ and the net specific energy for comminuting is simply $E_{net} = E \cdot f$. This E_{net} is assumed to increase linearly with s with a constant γ (dimension: J/m^2):

$$E_{net} = \gamma \cdot s \tag{2.15}$$

On the other hand, s is associated with the equivalent size, D_s, simply through the equation: $D_s = 6/(\rho \cdot s)$. Interestingly, the characteristic size, D_{50} was found to show a power law relationship with D_s:

$$D_{50} = b \cdot D_s^{\,m} \tag{2.16}$$

After rearrangement of the above equations, the specific energy is expressed as:

$$E = \left(\frac{6 \cdot \gamma \cdot b^{1/m}}{\rho \cdot f_0} \right)^{1/n} \cdot \frac{1}{D_{50}^{\,1/(m \cdot n)}} \tag{2.17}$$

and thus the specific energy E_{12} required to grind a sample of equivalent size $D_{1,s}$ to the size, $D_{2,s}$ is simply the deduction based on equation (2.17):

$$E_{12} = \left(\frac{6 \cdot \gamma \cdot b^{1/m}}{\rho \cdot f_0} \right)^{1/n} \cdot \left(\frac{1}{d_{1,50}^{\,1/(m \cdot n)}} - \frac{1}{d_{2,50}^{\,1/(m \cdot n)}} \right) \tag{2.18}$$

It is noted that when $1/(m \cdot n)$ equals to 1 and 0.5, the equation (2.18) would have similar form with Rittinger's and Bond's equations, respectively

3.3 Discussion

Strictly speaking, none of the three classical approaches works as expected. This has been realised long ago (e.g., Hukki 1962). One problem might be the selection of grain size: what is the reference size (or characteristic size)? With plenty of mineral particles, there is no single size, but rather various sizes. For different sizes taken as criteria (e.g., passing sizes of D_{10}, D_{50} or D_{80}), the energy–size relationship would be very different. As stated by Hukki (1962), each of these laws might be applicable for different narrow size ranges: Rittinger's model is more applicable for finer grinding, Kick's for crushing, and Bond's for conventional milling. These limitations could be improved by using advanced models (e.g., PBMs), which consider size reduction by representing the full GSD. However, there are too many unphysical parameters required in those models, e.g., eight parameters for Fuerstenau et al's (1991) model (analytical solution of equation (2.13)). Particularly for different grinding systems, many calibrations are desirable to determine the new values of those parameters. Further, the selection functions and breakage functions used are not physically understood; they are mostly mathemetically constrained to satisfy the experimental data and may even become negative, which is meaningless (Austin 1972). Although the matrix expression proposed by Campbell et al. (2001) can avoid problems such as that of irrational selection function, their predictive abilities rely on many series of grinding tests before constructing the matrix expression. In brief, these advanced models, despite their theoretical merit over classical models, seem difficult to use in practice.

Another problem is how to really know how much energy is exclusively consumed by breaking particles. When the fractures occur in grains, there is not only the energy consumed by the surface created but also much energy is dissipated from friction, sound emission, heat transfer and dissipation via energy redistribution (Nguyen and Einav 2009; Russell 2011). However, since necessary information on the flow of energy and its distribution in the mill is lacking, a detailed and accurate energy audit is not possible. As a consequence, a useful and meaningful energy law can only be

formulated in terms of the overall net energy expended in operating the comminution machine (Kapur and Fuerstenau 1987). However, this is beyond the ability of PBMs since they are based on mass balance, not energy. From the point of view of soil mechanics, the energy problem can be explored by employing an appropriate constitutive model that underpins grain crushing mechanisms within the framework of the thermodynamic laws.

In addition, the existing models dealing with mineral commintuion have not considered boundary conditions, such as grinding speeds, roller gaps, rollers' friction, etc. Those boundary conditions, of course, influence the energy–size reduction relationship in comminution. For example, increasing the rollers' gaps to a large extent will eventually stop producing new surface areas. However, such changes could not be monitored by existing comminution models since they (the models) do not account for the effect of boundary conditions.

In general, the fundamental questions in size–reduction relationships might be summarised as follows: 1) what is the distribution of the products from a mill if the size distribution of the feed granule is known? 2) how to set up an efficient operation to obtain a required product of fine sizes from coarse feed material? These are the research aims in Chapter VII using the novel continuum breakage mechanics theory.

4 Models for granular crushing

From the point of view of geotechnical engineering, an appropriate constitutive model for granular materials might be helpful for various engineering problems involving grain crushing. In this section, existing granular models are reviewed. Particular attention is given to the study of GSD and its evolution that has been recognised as important in the macroscopic response of granular materials.

4.1 Continuum modelling of granular materials

Recent advances in granular mechanics encourage the development of models in the analysis of grain crushing. A good attempt was recently proposed by McDowell et al. (1996). Based on the assumption of fractal crushing of granular materials, they developed an approach called "clastic mechanics" that has been later extensively

studied (McDowell and Bolton 1997; McDowell and Bolton 1999). In their formulation of the energy equilibrium equation, the energy dissipation due to breakage and new surface area is included. This means that their theory is able to explain the soil hardening as the result of fragmentation, the so-called "clastic hardening". In addition, their theory provides a physical justification to the critical state parameter, λ, which was used in the Cam Clay model. However, their energy equilibrium equation missed the consideration of energy dissipation due to load redistribution. This dissipation is significantly larger than energy dissipation due to the creation of surface (Russell 2011). Another effort by Ueng and Chen (2000) assumed a linear connection between the energy dissipation and surface areas due to grain crushing. On this assumption, Ueng and Chen were able to interpret the results of confined shear deformation. Alternatively, Lade et al. (1996) connected the input energy with the growth of various breakage measures to study the experimental constitutive relations of crushable grains through many drained and undrained triaxial shear tests under high pressure. One of the breakage measures, Marsal's breakage index, has been adopted by Indraratna and Salim (2002) to establish a model that links the energy consumption due to crushing linearly with the breakage index. However, this brought additional phenomenological parameters from curve-fitting tests, which replaced the role of the breakage index as an independent state parameter. Therefore, this model did not provide the required solution: a model dependent only on physically understood parameters, which, by itself, could predict the evolving GSD.

4.2 Importance of GSD

The above mentioned contributions have different levels of complexity and applicability; however none of those works enable us to formulate a complete constitutive equation that links between the rates of the stress and strain tensors. This provides motivation for researchers to develop a rigorous constitutive model that incorporates important experimentally observed features during grain crushing. One of these naturally observed features is the evolution of GSD in any kind of comminution (Vesic and Clough 1968; Hardin 1985; Coop 1990; Hagerty et al. 1993; Lade et al. 1996; McDowell et al. 1996; McDowell and Bolton 1998; Nakata et al. 1999; Nakata et al. 2001). As crushing continues, the GSD shifts towards the ultimate

state and particles become less likely to be further broken. Therefore, there is a need to establish a connection between the evolving GSD and the overall granular response.

GSD has been recognised to be particularly important in determining the macroscopic behaviour of granular materials (Hardin 1985; McDowell and Bolton 1998; Lade et al. 1996). Taking one-dimensional compression tests of sand for example, the compression curves are different for the same void ratio but variable GSDs, as shown in Figure 2.6a. Based on those results, two main distinguished features can be shown:

(1) Different yield strengths, p_{y0} are found, representing the turning points in each curve

(2) Unlike clay, compressing sand would not develop a unique critical state relation in the e-log (σ_v) scale (Yamamuro and Lade 1998; Mooney et al. 1998).

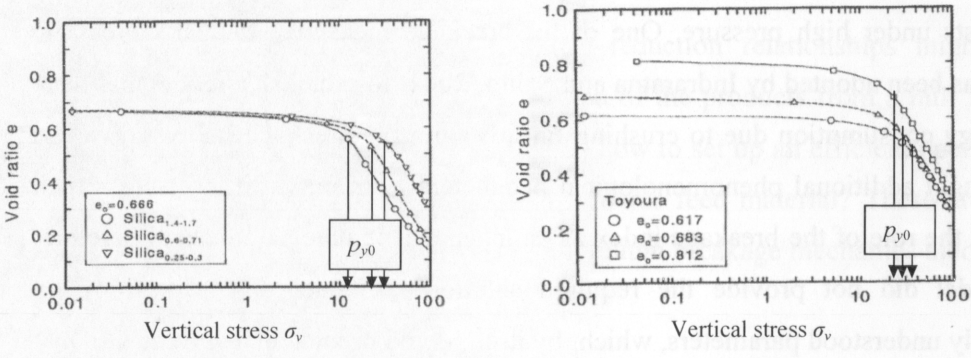

(a) (b)

Figure 2.6 Effect of (a) particle sizes and (b) void ratios on initial yielding stress and post-yield slope (Nakata et al. 2001)

Those changes can also be found if the initial grain sizes are kept the same and different void ratios are used at the start as shown in Figure 2.6b. If the same test was conducted on other granules, say pasta, the same effect of GSD could also be found (McDowell and Daniel 2001). Therefore, there is a motivation for researchers to explain these curves in terms of tracking the evolution of GSD. The models with this ability might potentially form the physical foundations for clarifying many geo-phenomena, and improve the confidence of geotechnical engineers in using constitutive models for sands (Einav 2007a).

4.3 Evolution of GSD

In view of the importance of evolving GSD, much effort has been devoted to capturing such shifting from the initial stage to the ultimate condition. In general, the methods to determine the GSD fall into two categories: constrained (e.g., Sammis et al. 1987) and unconstrained approaches (e.g., Gilvarry 1961; Palmer and Sanderson 1991). The unconstrained method assumes that particle crushing is dependent not on their neighbouring particles but on intrinsic strength. Based on this idea, Gilvarry (1964) proposed an expression to connect cumulative GSD with the Poisson distribution of flaw sizes. An alternative unconstrained model was developed by Epstein (1949), who assumed the same probability of breakage for various sizes of grain. This results in the conclusion that any initial GSD would approach to a self-similarity distribution under extremely large compression conditions.

The unconstrained models might be suitable for a small number of particles (particularly for a single grain) while for large quantities of grain, the evolving GSD becomes more complicated to predict. In such a situation, the grain crushing is not only affected by the particle's intrinsic strength but also by the configuration of neighbouring particles. In other words, the most relevant factors contributing to the grain's fracture are the size and strength of the surrounding particles. Models based on this idea are called constrained methods. This idea, compared with unconstrained models, has been shown to be able to explain the widely observed crushing phenomena such as cushion effect, self-similar distribution and ultimate fractal distribution of the grain sizes.

(1) Cushion effect and self-similar distribution

Generally, a bigger particle is easier to break than a smaller one due to the higher probability of flaws in bigger grain. However, this is not always true. In some cases, bigger particles might be surrounded by smaller grains as they migrate into the pore space among the bigger particles. These smaller particles therefore form a sort of cushion, preventing the bigger grains from further crushing (see Figure 2.7). This cushion is believed helpful to form the self-similar distribution (e.g., Sammis et al. 1986). Such distribution, for instance, is represented in Figure 2.8 (Ben–Nun and Einav 2010). According to Sammis et al., once this distribution is achieved, particles

with various sizes would have the same probability of failure and hence the self-similarity would be maintained. Eventually, even under extremely large deformation, some bigger particles might still survive. This illustration seems to agree with the assumption proposed by Epstein (1949).

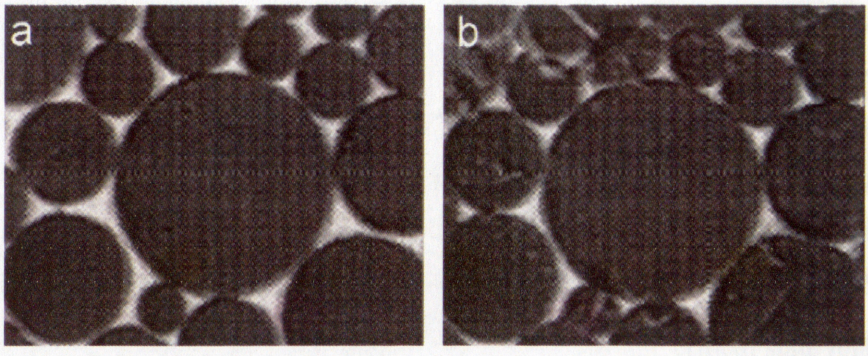

Figure 2.7. Experimental observation of 'cushioning effect' in disks assembly Tsoungui et al. (1999)

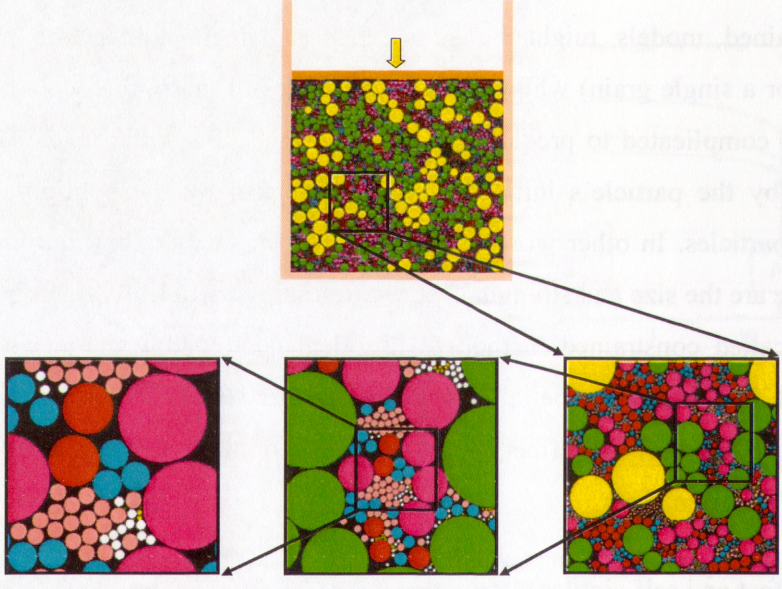

Figure 2.8 Self-similarity appears across the scales (Ben–Nun and Einav 2010)

(2) Ultimate GSD

To study the ultimate GSD, extremely large deformation tests are required. These can be realised in ring shear tests where unlimited shear deformation can be achieved. By extensively using such tests, the final distributions of fragment are usually observed to be self-similar and to follow a power law with power coefficient from 2.7 to 3.0. In constrained large-strain problems where the collision probability is independent of the size of the particles α appears to approach 3.0 (Sammis and King 2007). This is the

so-called fractal distribution by mass (seen an example in Figure 2.9). Although not absolutely necessary, it is practical to employ a fractal power law $F_u(x)$ (Sammis et al. 1986; McDowell et al. 1996; Coop et al. 2004).

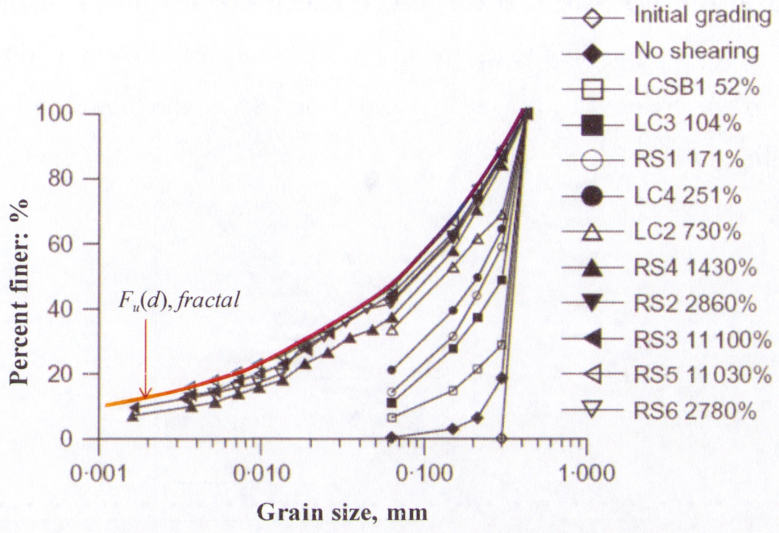

Figure 2.9 Experimental evolution of grain size distribution of Dog's Bay sand during ring shear tests to a vertical stress of 650-930 kPa by Coop et al. (2004), with additional ultimate distribution F_u (Einav 2007a)

(3) Minimum ultimate grain size

It can be expected that under extremely large deformations, the minimum size of grains should tend to zero. However, it is found that very fine particles usually deform plastically rather than fracturing, which sets the theoretical limit at about 1 μm size (Kendall 1978). Although supported theoretically by fracture mechanics (Kendall 1978), the value of 1 μm can only be regarded as a putative limit. The real size limit is surely dependent on the material and the comminution process, and the question of what should be this limit is therefore open. For example, the limit of 0.2 μm was observed in steam jet milling[6]. On the other hand, the limit of 1 μm is widely adopted by the mineral processing community (Prasher 1987). Therefore, we proceed with this size as the minimum. This is essential because in the absent of any minimum size limit the resulting product specific surface areas (surface divided by volume) will tend towards an unreasonable infinite value (Stamboliadis 2007) since at this extreme case the volume vanishes relative to the surface area.

6 http://www.ceramicindustry.com/articles/print/92186 (access on 24/07/2012)

4.4 Breakage index

Many different measures have been proposed to measure the amount of fragmentation of crushable material; a widely used measure is that following Hardin's (1985) proposition of a relative breakage index B_r. In his statement, the ultimate grain size under extremely large compression tends to be a cut-off value of 0.074mm (silt size). In other words, no grain would be bigger than 0.074mm. Thus, the breakage index is defined as the ratio of the areas in Figure 2.10.

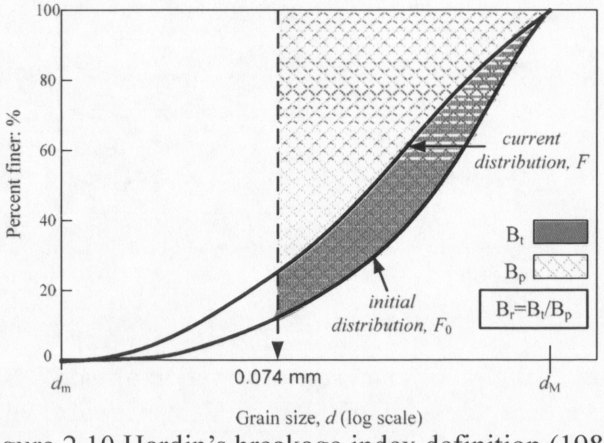

Figure 2.10 Hardin's breakage index definition (1985)

4.5 Breakage mechanics theory and models

From Sections 4.2 to 4.4, it can be seen the incorporation of the GSD into constitutive modelling is essential, such that the evolving GSD under different compression conditions could be predicted. However, existing constitutive models for granular materials reviewed in Section 4.1 are not capable of achieving this.

A recently developed continuum mechanics theory called breakage mechanics (Einav 2007a) opens a new potential for constitutive modelling of crushable granular materials by allowing for the prediction of evolving GSD at any time. Such evolution is further connected with mechanical stress-strain response of the material. This is one of the key features of breakage mechanics. In addition, unlike most relationships that connect the stresses and strains in a purely phenomenological way, breakage mechanics depend on only a few physically measurable parameters and are cast in a consistent thermodynamic framework. Consequently, the critical phenomena (e.g., the dependence on initial grading and pre-consolidation pressure) of granular materials

can be better explained at the physical microscopic level of crushing, such as isotropic hardening behaviour and progression of the yielding strength.

Various models of breakage mechanics have been derived and validated in different engineering disciplines (see examples in Einav and Valdes 2008; Nguyen and Einav 2009; Das et al. 2011; Zhang et al. 2012; Buscarnera and Einav 2012; Rubin and Einav 2011). Good introductory reading on the breakage mechanics theory and breakage models can be found in the above references while for fundamentals of this theory, references to Einav (2007a, b), are useful.

5 Computational methods in large deformation problems

To make full use of breakage mechanics for engineering purposes, large-deformation simulations of granular crushing is needed. Thanks to the advance of computational methods, many finite element analysis programs are now available for large-strain problems. abaqus (2010) for example, provides two typical relationships between mesh and underlying material when dealing with large deformation problems: Arbitrary Lagrangian Eulerian (ALE) adaptive meshing and Eulerian. Those methods are recently used, for instance, in dealing with the large pile penetration problem (e.g., Endra and Roman 2003; Sheng et al. 2005). With the ALE remeshing technique, the mesh motion is constrained to the material motion only at the free boundaries, while inside the model the mesh and material motions are separated. With this method, mesh distortion can be minimised by adjusting the shape of the mesh relative to the material inside the material boundaries and a good mesh is therefore maintained throughout the analysis. At the same time, it is easy to capture the material boundaries because they are always the same as the mesh-free surfaces.

The other technique uses the Eulerian formulation in which the nodes stay fixed while the material flows through the mesh. Though it becomes difficult to track the free surfaces of the material with the Eulerian formulation, it has the apparent advantage of eliminating mesh distortion caused by material deformation. Particularly for analysis with extreme deformation, such as fluid flow, the Eulerian technique may be the only method that can provide a solution (abaqus 2010). In light of the rigorous performance of the finite element analysis (FEA), this thesis adopts the ALE and

Eulerian technique in abaqus to carry out the large-deformation simulations (in Chapters V, VI and VII).

Chapter III

Continuum breakage mechanics: Review of theory and models

1 Introduction

The significance of thermodynamics in the formulation and development of constitutive models has been widely acknowledged (e.g., Zytynski et al. 1978, Ziegler 1977; Collins and Houlsby 1997; Houlsby and Puzrin 2000; Einav 2002). Both the first and second laws of thermodynamics must be satisfied in the constitutive modelling, so that the derived models are rigorous, consistent and physically meaningful. Otherwise, models that violate thermodynamics cannot be used with any confidence to describe material behaviour (except perhaps under some rather particular and well-defined conditions) (Houlsby and Puzrin 2000).

The formulation of continuum breakage mechanics by Einav (2007a, b) are developed based on the thermodynamics principles. In addition, this theory also emphasises the significance of linking micro to macro scales (i.e., avoiding as much as possible the arbitrary mathematical structures) in constitutive modelling: it incorporates GSD and its evolution (through breakage, B) to capture macroscopic soil behaviour. In this way, the underlying microscopic process connects with macroscopic behaviour, which many other continuum theories fail to capture.

The various models previously derived from breakage mechanics are all thermodynamically consistent, providing better explanations of many of the phenomenological aspects of crushable soil behaviour. These models have thus far been used in different applications, including geophysics (Nguyen and Einav 2009; Das et al. 2011), foundation engineering (Zhang et al. 2011; Zhang et al. 2012),

unsaturated soil mechanics (Buscarnera and Einav 2012), and a general breakage model accounting for finite deformation and porous compaction and dilation (Rubin and Einav 2011). In addition, an extended breakage theory was defined to explain the mechanics of granular mixtures (Einav and Valdes 2008).

The objective of this chapter is to present the hierarchy in the development of continuum breakage mechanics. This includes the concepts, hypotheses, and thermodynamic procedures on which the theory is based. Finally, a linear breakage model (2007a, b), which will be referred to throughout the whole thesis, is explained carefully. This is followed by a brief review of other enhanced breakage models recently derived from the field of breakage mechanics.

2 Breakage

To better quantify the amount of grain crushing within compacted crushable granular materials, Einav (2007a) proposed that the property of breakage should be based on the relative position of the current cumulative GSD from:

(1) an initial cumulative distribution, and

(2) a physical ultimate distribution curve (which, for most practical purposes, could be assumed to be fractal).

This definition appears in Figure 3.1 with the breakage B (bearing some connection to Hardin's relative breakage B_r presented in Chapter II) expressed as:

$$B = \frac{B_t}{B_p} \tag{3.1}$$

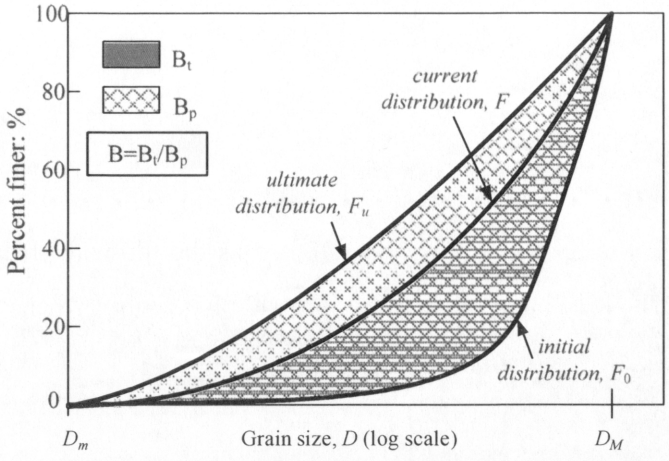

Figure 3.1 Einav's breakage definition (2007a)

It will later be shown that B is an internal state variable in a thermodynamic sense. The connection between B and current cumulative GSD, $F(x)$, is assumed to obey a linear scale based on the initial cumulative GSD, $F_0(x)$, and final cumulative GSD, $F_u(x)$ in terms of grain sizes x:

$$F(x,B)=(1-B)F_0(x)+BF_u(x) \tag{3.2}$$

In statistical analysis, it is more convenient to use GSD, $p(x,B)$ that is given by differentiating $F(x, B)$, and correspondingly:

$$p(x,B)=(1-B)p_0(x)+Bp_u(x) \tag{3.3}$$

where $p_0(x)$ and $p_u(x)$ define the initial and final GSD. Therefore, any current $p(x, B)$ could also be assessed for a given B.

As for the ultimate distribution, Turcotte (1986), by assuming the minimum size, D_m is zero, gave a fractal distribution by mass:

$$F_u(x)=\left(\frac{x}{D_M}\right)^{3-\alpha} \tag{3.4}$$

in which D_M denotes the maximum grain size. A drawback of the assumption of D_m=0 in equation (3.4), for instance in mineral comminution, might lead the calculated specific surface area of the product materials to be infinity as the size approaches zero (Stamboliadis 2007). Alternatively, Einav (2007a), ackowledging the physical size limit of D_m (e.g., taking 1μm), obtained the modified form of the fractal distribution

by mass:

$$F_u(x) = \frac{x^{3-\alpha} - D_m{}^{3-\alpha}}{D_M{}^{3-\alpha} - D_m{}^{3-\alpha}} \tag{3.5}$$

The above modified fractal form in (3.5) is adopted as the ultimate size distribution throughout the thesis. Notice that the above expression has a limit when $\alpha = 3$, where it becomes $F_u(x) = \log(x / D_m) / \log(D_M / D_m)$ (Einav 2007a).

3 Statistical homogenisation

Adopting the proposed breakage property, Einav (2007a) used the approach of statistical homogenisation* to incorporate the GSD, $p(x,B)$ into a continuum mathematical formulation. As seen in equation (3.6) the GSD, $p(x,B)$ has been incorporated as a weighting average function over the microscopic variables $A(x)$to get any statistical average microscopic variable $\langle A \rangle$ (" $\langle\ \rangle$ " denotes statistical average):

$$\langle A \rangle = \int_{D_m}^{D_M} A(x) p(x,B) \mathrm{d}x = \langle A \rangle_0 (1-B) + \langle A \rangle_u B \tag{3.6}$$

where

$$\langle A \rangle_0 = \int_{D_m}^{D_M} A(x) p_0(x) \mathrm{d}x \tag{3.7}$$

$$\langle A \rangle_u = \int_{D_m}^{D_M} A(x) p_u(x) \mathrm{d}x \tag{3.8}$$

D_M and D_m denote the maximum and minimum size of particles. $A(x)$ can be treated as any microscopic variable. For instance, if we consider $A(x)$ as the energy stored in

* Homogenisation approaches have been used in many recent studies to describe the global behaviour of granular medium based on the knowledge of the microscopic characteristics of the material such as the inter-particle contact law, the particle size distribution and initial arrangement (Emeriault and Claquin 2000; Emeriault 2004).

fraction size x, i.e., $A(x)=\psi(x,\varepsilon_e)$ which is also a function of notional macroscopic elastic strain, ε_e (expressed as a tensor). Thus, by making use of equations (3.6) to (3.8) the Helmholtz free energy potential, $\Psi(x,\varepsilon_e)$, could be expressed as:

$$\Psi(x,\varepsilon_e)=\Psi_0(1-B)+\Psi_u B \tag{3.9}$$

where,

$$\Psi_0=\int_{D_m}^{D_M}\psi(x,\varepsilon_e)p_0(x)\mathrm{d}x \tag{3.10}$$

$$\Psi_u=\int_{D_m}^{D_M}\psi(x,\varepsilon_e)p_u(x)\mathrm{d}x \tag{3.11}$$

in which Ψ_0 and Ψ_u are Helmholtz free energy based on initial and ultimate GSDs.

4 Energy split hypothesis

The core idea in this hypothesis is that the difference between the stored energy of different sizes of grain is proportional to their size. This is because the larger grains have a larger surface area, which attract more forces (or energy) on average. Therefore, the stored energy of grains is in proportion to their size, i.e., their diameter. A general non-dimensional power function may be adopted to present energy split ability (Einav 2007a):

$$f_\psi(x)=\left(\frac{x}{x_r}\right)^n \tag{3.12}$$

in which x_r represents the reference grain size with reference stored energy of $\psi_r(\varepsilon_e)$. Thus by making use of equation (3.12), the stored energy for other grains with the size of x is expressed:

$$\psi(x,\varepsilon_e)=f_\psi(x)\psi_r(\varepsilon_e) \tag{3.13}$$

Rewriting equations (3.10) and (3.11) by using equation (3.13) and employing the statistical average gives:

$$\Psi_0 = \psi_r(\varepsilon_e)\int_{D_m}^{D_M} f_\psi(x)p_0(x)\mathrm{d}x = \psi_r(\varepsilon_e)\langle f_\psi(x)\rangle_0 \tag{3.14}$$

$$\Psi_u = \psi_r(\varepsilon_e)\int_{D_m}^{D_M} f_\psi(x)p_u(x)\mathrm{d}x = \psi_r(\varepsilon_e)\langle f_\psi(x)\rangle_u \tag{3.15}$$

Substituting the equation (3.12) to the above two equations:

$$\Psi_0 = \psi_r(\varepsilon_e)\int_{D_m}^{D_M}\left(\frac{x}{x_r}\right)^n p_0(x)\mathrm{d}x = \psi_r(\varepsilon_e)\frac{\int_{D_m}^{D_M} x^n p_0(x)\mathrm{d}x}{x_r{}^n} = \psi_r(\varepsilon_e)\frac{J_{n0}}{x_r{}^n} \tag{3.16}$$

$$\Psi_u = \psi_r(\varepsilon_e)\int_{D_m}^{D_M}\left(\frac{x}{x_r}\right)^n p_u(x)\mathrm{d}x = \psi_r(\varepsilon_e)\frac{\int_{D_m}^{D_M} x^n p_u(x)\mathrm{d}x}{x_r{}^n} = \psi_r(\varepsilon_e)\frac{J_{nu}}{x_r{}^n} \tag{3.17}$$

J_{n0} and J_{nu} are the nth order moment of the initial and ultimate GSDs. For example, the first order current moment J_1 is the mean particle size for plate disks, and second order current moment J_2 (corresponding to sphere balls) describes the way in which the grain sizes are distributed around the mean grain size J_1. Thus, with equations (3.16) and (3.17), the equation (3.9) becomes:

$$\Psi = \frac{\psi_r(\varepsilon_e)}{x_r{}^n}\left(J_{n0}(1-B)+J_{nu}B\right) \tag{3.18}$$

The question for equation (3.18) is, what is the reference size, x_r? To a first order let us set x_r equal to J_{n0}. After rearrangement, the (3.18) becomes:

$$\Psi = \psi_r(\varepsilon_e)\left(1-\left(1-\frac{J_{nu}}{J_{n0}}\right)B\right) = \psi_r(\varepsilon_e)(1-\vartheta B) \tag{3.19}$$

where,

$$\vartheta = 1-\frac{J_{nu}}{J_{n0}} \tag{3.20}$$

ϑ is called the 'criticality proximity parameter', which measures how far the initial GSD is from the ultimate GSD (Einav 2007a). It can be seen before crushing (i.e., B=0), the equation (3.19) means the specific strain energy of the confining granular material (i.e., gross average stored energy) equates to the stored energy within the reference grain size, x_r; as B develops, the current specific strain energy decreases with decreasing $(1-\vartheta B)$.

5 Thermodynamic formulation of breakage mechanics

With the previous background, it is now possible to incorporate the concept of breakage in thermomechanical formulation and deriving rigorous models that adequately represent the grain crushing behaviour of crushable granular materials.

5.1 Energy balance equation

The first and second laws of thermodynamics of rate independent compacted agglomerate in isothermal conditions take the following forms (e.g., Ziegler 1977; Houlsby and Puzrin 2000; Walsh and Tordesillas 2004; Collins and Einav 2005):

$$\delta W = \mathrm{d}\Psi + \delta\Phi \tag{3.21}$$

$$\delta\Phi \geq 0 \tag{3.22}$$

where $\mathrm{d}\Psi$ is the increment of Helmholtz free energy; δW is the increment of mechanical work along the boundaries of a representative volume element and $\delta\Phi$ is the non-negative increment of energy dissipation. The increments are represented by different symbols to specify that W and Φ, unlike Ψ, would not be differentiable with respect to state variables.

A general expression of δW is:

$$\delta W = \boldsymbol{\sigma} : \mathrm{d}\boldsymbol{\varepsilon} = \boldsymbol{\sigma} : \left(\mathrm{d}\boldsymbol{\varepsilon}_{\mathbf{e}} + \mathrm{d}\boldsymbol{\varepsilon}_{\mathbf{p}}\right) \tag{3.23}$$

where $\mathrm{d}\boldsymbol{\varepsilon}$, $\mathrm{d}\boldsymbol{\varepsilon}_{\mathbf{e}}$ and $\mathrm{d}\boldsymbol{\varepsilon}_{\mathbf{p}}$ are increments of total, elastic and plastic strains in tensor form; $\boldsymbol{\sigma}$ is stress tensor. According to equation (3.19), the increment of Helmholtz free energy is:

$$\mathrm{d}\Psi = \psi_r'(\boldsymbol{\varepsilon}_\mathbf{e})(1-\vartheta B) : \mathrm{d}\boldsymbol{\varepsilon}_\mathbf{e} - \vartheta\psi_r(\boldsymbol{\varepsilon}_\mathbf{e})\mathrm{d}B \tag{3.24}$$

The only expression now required to complete the energy balance equation (3.21) is the formulation of $\delta\Phi$ that supposes to be the combination of plastic $\delta\Phi_p$ and the breakage $\delta\Phi_B$ components. In conventional rate independent plasticity, the increment of plastic dissipation is assumed a homogeneous first order function of the plastic strain increment:

$$\delta\Phi_p = \frac{\partial\delta\Phi_p}{\partial\mathrm{d}\boldsymbol{\varepsilon}_\mathbf{p}} : \mathrm{d}\boldsymbol{\varepsilon}_\mathbf{p} \tag{3.25}$$

Analogous to the formulation of $\delta\Phi_p$, the increment of plastic dissipation, $\delta\Phi_B$ for rate independent granular materials is also assumed as equation (3.26), which is simply a first order homogeneous function of the breakage increment (Einav 2007a):

$$\delta\Phi_B = \frac{\partial\delta\Phi_B}{\partial\mathrm{d}B}\mathrm{d}B \tag{3.26}$$

A convenient form to couple $\delta\Phi_p$ and $\delta\Phi_B$ with $\delta\Phi$ may be:

$$\delta\Phi = \sqrt{\delta\Phi_p^2 + \delta\Phi_B^2} \tag{3.27}$$

Substituting the equations (3.23), (3.24) with (3.27) into the energy conservation equation (3.21):

$$\left(\boldsymbol{\sigma} - \psi_r'(\boldsymbol{\varepsilon}_\mathbf{e})(1-\vartheta B)\right) : \mathrm{d}\boldsymbol{\varepsilon}_\mathbf{e} + \left(\boldsymbol{\sigma} - \frac{\partial\delta\Phi}{\partial\mathrm{d}\boldsymbol{\varepsilon}_\mathbf{p}}\right) : \mathrm{d}\boldsymbol{\varepsilon}_\mathbf{p} + \left(\vartheta\psi_r(\boldsymbol{\varepsilon}_\mathbf{e}) - \frac{\partial\delta\Phi}{\partial\mathrm{d}B}\right)\mathrm{d}B = 0 \tag{3.28}$$

Following the Ziegler's orthogonality principle (1977), it is suggested that the terms in the brackets are zero,equations (3.19) and (3.27), thus:

$$\boldsymbol{\sigma} = \psi_r'(\boldsymbol{\varepsilon}_\mathbf{e})(1-\vartheta B) = \frac{\partial\Psi}{\partial\boldsymbol{\varepsilon}_\mathbf{e}} \tag{3.29}$$

$$\boldsymbol{\sigma} = \frac{\partial\delta\Phi}{\partial\mathrm{d}\boldsymbol{\varepsilon}_\mathbf{p}} = \frac{\partial\delta\Phi}{\partial\delta\Phi_p}\frac{\partial\delta\Phi_p}{\partial\mathrm{d}\boldsymbol{\varepsilon}_\mathbf{p}} = \frac{\delta\Phi_p}{\delta\Phi}\frac{\partial\delta\Phi_p}{\partial\mathrm{d}\boldsymbol{\varepsilon}_\mathbf{p}} \tag{3.30}$$

where the second equality in (3.29) is due to (3.19), and the second equality in (3.30)

is due to (3.27). Also following ziegler, a new stress-like variable is designated and is called (A3) breakage energy E_B (explained later):

$$E_B = \vartheta\psi_r(\varepsilon_e) = -\frac{\partial \Psi}{\partial B} \tag{3.31}$$

$$E_B = \frac{\partial \delta \Phi}{\partial dB} = \frac{\partial \delta \Phi}{\partial \delta \Phi_B}\frac{\partial \delta \Phi_B}{\partial dB} = \frac{\delta \Phi_B}{\delta \Phi}\frac{\partial \delta \Phi_B}{\partial dB} \tag{3.32}$$

Equations (3.29)–(3.32) denote that both $\boldsymbol{\sigma}$ and E_B can be obtained not only from Helmholtz free energy but also by energy dissipation caused by plastic strains or breakage.

5.2 Breakage energy and residual breakage energy

To elaborate the meaning of E_B, which is one of the fundamental properties in continuum mechanics, let us rewrite equation (3.31) by using (3.20), together with equations (3.16) and (3.17):

$$E_B = \psi_r(\varepsilon_e)\left(\frac{J_{n0} - J_{nu}}{J_{n0}}\right) = \psi_r(\varepsilon_e)\left(\frac{J_{n0} - J_{nu}}{x_r^n}\right) = \Psi_0 - \Psi_u \tag{3.33}$$

Therefore, the breakage energy E_B describes the total stored free energy available for release from the system during the fracturing from the state of initial GSD to the final state of an ultimate GSD (Einav 2007a). Besides the total consumable energy, E_B, what further interests us is the available energy for breakage at the current fracturing stage. An internal variable residual breakage energy, E_B^*, is proposed:

$$E_B^* = E_B(1 - B) \tag{3.34}$$

From equation (3.9) we have:

$$B = \frac{\Psi_0 - \Psi}{\Psi_0 - \Psi_u} \tag{3.35}$$

$$1 - B = \frac{\Psi - \Psi_u}{\Psi_0 - \Psi_u} \tag{3.36}$$

With equations (3.33) and (3.34), the equation (3.36) can be further expressed as

$$E_B^* = \Psi - \Psi_u, \tag{3.37}$$

representing the current stored energy at the current GSD that is available for release for further fracturing. In fact, the breakage energy E_B can be treated as a particular E_B^* before the commencement of breakage (B=0).

5.3 Breakage growth assumption

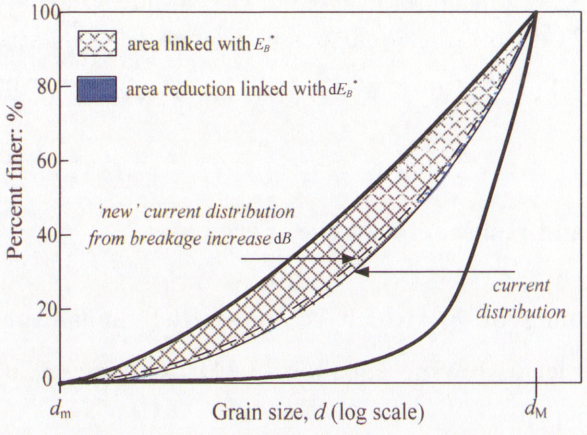

Figure 3.2 Breakage growth assumption (Einav 2007a)

As illustrated in Figure 3.2, "new" current cumulative GSD from breakage dissipation, $\delta\Phi_B$ that associates with dB is assumed equal to the loss of residual breakage energy, dE_B^*. A simple postulate of breakage growth states that $\delta\Phi_B$ is fully attained from dE_B^* (Einav 2007a):

$$\delta\Phi_B = dE_B^* \tag{3.38}$$

From equation (3.34):

$$dE_B^* = dE_B(1-B) - E_B dB \tag{3.39}$$

5.4 Yield functions

5.4.1 Breakage yield function in an elastic-breakage model

From equations (3.26) and (3.32), in which $\delta\Phi = \delta\Phi_B$ in a pure elastic-breakage case:

$$\delta\Phi_B - E_B dB = 0 \tag{3.40}$$

The breakage yield function, associated with the evolution of $\mathrm{d}B$, is related to the breakage dissipation function $\delta\Phi_B$ given in equation (3.40). As the breakage dissipation is homogeneous and first order function of $\mathrm{d}B$, a general relationship is given by a degenerate Legendre transformation (Collins and Houlsby 1997):

$$\delta\lambda_B y_B \equiv E_B \mathrm{d}B - \delta\Phi_B = 0 \tag{3.41}$$

in which y_B denotes the yielding function in breakage space, and $\delta\lambda_B \geq 0$ is a common non-negative multiplier. A possible yielding function of (3.41) might be obtained by integrating the equations (3.39) and (3.40), presented as:

$$y_B = E_B(1-B)^2 - E_c \leq 0 \tag{3.42}$$

where E_c is called "breakage energy constant", is a constant resulted from the integration (Einav 2007b). Both (3.41) and special case of (3.42) describe the yield condition only relating to breakage dissipation but not accounting for the plastic strain dissipation.

5.4.2 Coupled yield function

The coupled dissipation function that includes the both breakage and plastic strain components is given in equation (3.27). It is possible to show them, together with equations (3.25) and (3.26):

$$\delta\Phi = \frac{\partial\delta\Phi}{\partial\delta\Phi_p}\frac{\partial\delta\Phi_p}{\partial\mathrm{d}\boldsymbol{\varepsilon}_\mathbf{p}} : \mathrm{d}\boldsymbol{\varepsilon}_\mathbf{p} + \frac{\partial\delta\Phi}{\partial\delta\Phi_B}\frac{\partial\delta\Phi_B}{\partial\mathrm{d}B}\mathrm{d}B = \frac{\delta\Phi_p^2}{\delta\Phi} + \frac{\delta\Phi_B^2}{\delta\Phi} \tag{3.43}$$

Therefore, the proposed coupled dissipation function in equation (3.27) is still a first order homogeneous function in the rates. Thus, the general form of the coupled yield function in dissipative breakage/dissipative stress space can also be given by a degenerate Legendre transformation:

$$\delta\lambda y^* \equiv \boldsymbol{\sigma} : \mathrm{d}\boldsymbol{\varepsilon}_\mathbf{p} + E_B\mathrm{d}B - \delta\Phi \leq 0 \tag{3.44}$$

From equations (3.25) and (3.26), we have $\mathrm{d}\boldsymbol{\varepsilon}_{\mathbf{p}} = \dfrac{\delta\Phi_p}{\partial\delta\Phi_p/\partial\mathrm{d}\boldsymbol{\varepsilon}_{\mathbf{p}}}$ and $\mathrm{d}B = \dfrac{\delta\Phi_B}{\partial\delta\Phi_B/\partial\mathrm{d}B}$ that are then placed in equation (3.44) resulting in:

$$\delta\lambda y^* \equiv \boldsymbol{\sigma} : \frac{\delta\Phi_p}{\partial\delta\Phi_p/\partial\mathrm{d}\boldsymbol{\varepsilon}_{\mathbf{p}}} + E_B\frac{\delta\Phi_B}{\partial\delta\Phi_B/\partial\mathrm{d}B} - \delta\Phi = 0 \tag{3.45}$$

Rewriting equations (3.30) and (3.32) gives $\delta\Phi_p = \boldsymbol{\sigma} : \dfrac{\delta\Phi}{\partial\delta\Phi_p/\partial\mathrm{d}\boldsymbol{\varepsilon}_{\mathbf{p}}}$ and $\delta\Phi_B = \dfrac{E_B\delta\Phi}{\partial\delta\Phi_B/\partial\mathrm{d}B}$ that are then substituted into equation (3.45), which, together with the condition $\delta\lambda \geq 0$, (3.45) becomes:

$$y^* \equiv \frac{\boldsymbol{\sigma} : \boldsymbol{\sigma}}{\left(\partial\delta\Phi_p/\partial\mathrm{d}\boldsymbol{\varepsilon}_{\mathbf{p}}\right) : \left(\partial\delta\Phi_p/\partial\mathrm{d}\boldsymbol{\varepsilon}_{\mathbf{p}}\right)} + \left(\frac{E_B}{\partial\delta\Phi_B/\partial\mathrm{d}B}\right)^2 - 1 \leq 0 \tag{3.46}$$

Equation (3.46) is a general form of coupled yield function, accounting for breakage dissipation and plastic dissipation (Einav 2007b). Alternatively, if we subdivide the $\delta\Phi_p$ in dissipation function (3.27) in terms of plastic volumetric dissipation, $\delta\Phi_p^v$ and plastic shear dissipation $\delta\Phi_p^s$:

$$\delta\Phi = \sqrt{\delta\Phi_p^{v\,2} + \delta\Phi_p^{s\,2} + \delta\Phi_B^2} \tag{3.47}$$

using a triaxial model, the coupled yield function (3.46) becomes:

$$y^* \equiv \left(\frac{p}{\partial\delta\Phi_p^v/\partial\mathrm{d}\varepsilon_v^p}\right)^2 + \left(\frac{q}{\partial\delta\Phi_p^s/\partial\mathrm{d}\varepsilon_s^p}\right)^2 + \left(\frac{E_B}{\partial\delta\Phi_B/\partial\mathrm{d}B}\right)^2 - 1 = 0 \tag{3.48}$$

The equation (3.48) reflects the yield function y^* in dissipative triaxial stress/breakage space, in which p and q denote the mean stress and triaxial shear stress.

6 Models developed from breakage mechanics theory

6.1 Breakage model based on linear elasticity (i.e., linear elastic breakage model)

The linear elastic breakage model is the simplest breakage model (Einav 2007a, b), in which the stored elastic energy equation (3.19) in a (reference) grain size is simplified by adopting linear elasticity (Einav 2007d):

$$\Psi = (1-\vartheta B)\left(\frac{1}{2}K\varepsilon_v^{e\,2} + \frac{3}{2}G\varepsilon_s^{e\,2}\right) \tag{3.49}$$

where K and G are the bulk and shear moduli, and ε_v^e and ε_s^e are the elastic volumetric and shear strains in triaxial conditions, respectively.

From the framework of thermodynamics (see equations (3.29) and (3.31)), constitutive equations can be defined as follows:

$$p = \frac{\partial \Psi}{\partial \varepsilon_v^e} = (1-\vartheta B)K\varepsilon_v^e \tag{3.50}$$

$$q = \frac{\partial \Psi}{\partial \varepsilon_s^e} = 3(1-\vartheta B)G\varepsilon_s^e \tag{3.51}$$

$$E_B = -\frac{\partial \Psi}{\partial B} = \frac{\vartheta}{2}\left(K\varepsilon_v^{e\,2} + 3G\varepsilon_s^{e\,2}\right) = \frac{\vartheta}{2(1-\vartheta B)^2}\left(\frac{p^2}{K} + \frac{q^2}{3G}\right) \tag{3.52}$$

Once breakage (or yield) develops, $E_B(1-B)^2/E_c = 1$ (as shown in equation (3.42)), and by incorporating this unity into the formulation of dissipations, we have:

$$\delta\Phi_B = \frac{E_B \mathrm{d}B}{\cos\omega} = \frac{\sqrt{E_B E_B}}{\cos\omega}\delta B = \frac{\sqrt{E_B E_c}}{(1-B)\cos\omega}\mathrm{d}B \tag{3.53}$$

$$\delta\Phi_p^v = \frac{p\mathrm{d}\varepsilon_v^p}{\sin\omega} = \frac{p}{\sin\omega}\frac{E_B(1-B)^2}{E_c}\mathrm{d}\varepsilon_v^p = \frac{p}{(1-B)\sin\omega}\sqrt{\frac{E_c}{E_B}}\mathrm{d}\varepsilon_v^p \tag{3.54}$$

$$\delta\Phi_p^s = q\left|\mathrm{d}\varepsilon_s^p\right| = Mp\left|\mathrm{d}\varepsilon_s^p\right| \tag{3.55}$$

Note that in isotropic compression, grains rearmament is only passive to breakage. The "plastic-breakage coupling angle, ω" (Einav 2007b) is thereby introduced to reflect the coupling effect between the breakage dissipation and plastic volumetric dissipation. $M=q_f/p_f$, is the ratio between the shear stress and volumetric stress at failure; $\mathrm{d}\varepsilon_v^p$ and $\mathrm{d}\varepsilon_s^p$ are the incremental volumetric and shear strains. The flow rules are defined based on the equation (3.48) that is derived obeying the second law of thermodynamics, with the mechanical dissipation assured of being non-negative. Consequently, the flow rules are defined as non-associated as follows:

$$\mathrm{d}\varepsilon_v^p = \delta\lambda\frac{\partial y^*}{\partial p} = \delta\lambda\frac{2E_B(1-B)^2\sin^2\omega}{pE_c} \tag{3.56}$$

$$\mathrm{d}\varepsilon_s^p = \delta\lambda\frac{\partial y^*}{\partial q} = \delta\lambda\frac{2q}{(Mp)^2} \tag{3.57}$$

$$\mathrm{d}B = \delta\lambda\frac{\partial y^*}{\partial E_B} = \delta\lambda\frac{2(1-B)^2\cos^2\omega}{E_c} \tag{3.58}$$

where $\delta\lambda$ is a non-negative multiplier; $\mathrm{d}B$ is the incremental breakage, such that we are now able to predict the evolution of the current GSD (i.e. equation (3.3)); and finally, the angle ω governs the coupling between plastic volumetric strain dissipation and grain crushing dissipation. Values $\omega=0^\circ$ and $\omega=90^\circ$ represent two extremes corresponding to dissipative processes due to grain crushing only and plastic volumetric strain only, respectively. The physical meaning of ω might relate to local pore collapse, with ω increasing as the amount of internal pores within the grains increases (see discussion by Das et al. (2011)).

Substituting equations (3.53)–(3.55) into (3.48), y^* can be expressed in the mixed space of all the above three stresses (Einav 2007c, d):

$$y=\frac{E_B}{E_c}(1-B)^2+\left(\frac{q}{Mp}\right)^2-1\le 0 \tag{3.59}$$

Alternatively, using equation (3.52):

$$y = \frac{\vartheta}{2E_c}\left(\frac{p^2}{K} + \frac{q^2}{3G}\right)\left(\frac{1-B}{1-\vartheta B}\right)^2 + \left(\frac{q}{Mp}\right)^2 - 1 \le 0 \tag{3.60}$$

An example of the yield surface in *p-q-B* space is plotted in Figure 3.3.

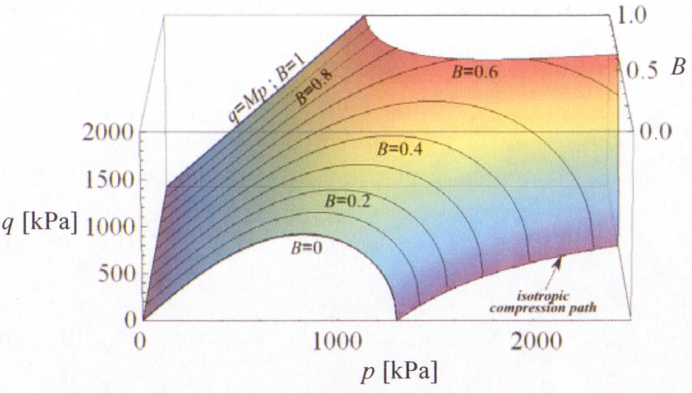

Figure 3.3 Yield surface in *p-q-B* space (Dog's Bay sand parameters, as listed in Table 4.2, Chapter IV)

The above model possesses only five physically identifiable mechanical parameters: shear and bulk modulus G and K; friction coefficient M; critical breakage energy constant E_c; and coupling angle ω between the friction and breakage dissipative processes. All of these parameters can be measured and calibrated using a single standard triaxial test involving a stage of isotropic compression followed by a stage of drained or undrained shear. In this standard test, the energy threshold E_c is calculated from the maximum yield pressure defining the first yield surface, the "comminution pressure", p_c, which marks the commencement of grain crushing during isotropic compression: $p_c = \sqrt{2KE_c/\vartheta}$ (Einav 2007c). In addition, the model responds to variations in the initial GSD through the grading index ϑ. To maximise the usefulness of this model, a convenient approach is to implement it into FE codes as detailed in Chapter IV.

6.2 Breakage model based on pressure-dependent elasticity

The pressure-dependent bulk and shear moduli could enhance the breakage model performance. This can be achieved by introducing a general form of Helmholtz free energy potential:

$$\Psi = (1-\vartheta B)\left(\psi_v\left(\varepsilon_v^e\right) + \psi_s\left(\varepsilon_v^e, \varepsilon_s^e\right)\right) \tag{3.61}$$

where unlike the simple linear elasticity in equation (3.49), $\psi_v\left(\varepsilon_v^e\right)$ takes the form from Einav (2007b):

$$\psi_v\left(\varepsilon_v^e\right)= p_r \frac{\left(\xi\left(\varepsilon_v^e\right)/p_r\right)^{2-m}}{\overline{K}(2-m)} \tag{3.62}$$

In the above equation, p_r is defined as a reference pressure conveniently taken as 1 kPa and $m=0.5$, and $\overline{K}$ is a material constant that depends on intrinsic bulk modulus of the granular material. $\xi\left(\varepsilon_v^e\right)$ represents the pressure as a function of elastic volumetric strain: $\xi\left(\varepsilon_v^e\right)= p_r\left(\overline{K}(1-m)\left(\varepsilon_v^e-\varepsilon_{vr}\right)+1\right)^{\frac{1}{1-m}}$ where ε_{vr} is the initial volumetric strain dependent on the maximum ($e_{\max}$) and initial (e_0) void ratios of the sample: $\varepsilon_{vr}=-\log\left((1+e_0)/(1+e_{\max})\right)$ (Einav and Puzrin, 2004). It is practical to take $\varepsilon_{vr}=0$ given the $e_{\max}$ unknown. From the formula $\xi\left(\varepsilon_v^e\right)$, the pressure-dependent bulk modulus $K\left(\varepsilon_v^e\right)$ can be derived:

$$K\left(\varepsilon_v^e\right)=\frac{\partial\xi\left(\varepsilon_v^e\right)}{\partial\varepsilon_v^e}= p_r\overline{K}\left(\frac{\xi\left(\varepsilon_v^e\right)}{p_r}\right)^m \tag{3.63}$$

To obtain the pressure-dependent shear modulus $G\left(\varepsilon_v^e\right)$, let us assume that the Poisson ratio ν remains unchanged. Since $\nu=\left(3K\left(\varepsilon_v^e\right)-2G\left(\varepsilon_v^e\right)\right)/\left(6K\left(\varepsilon_v^e\right)+2G\left(\varepsilon_v^e\right)\right)$, $G\left(\varepsilon_v^e\right)$ is thereby calculated:

$$G\left(\varepsilon_v^e\right)=\frac{3(1-2\nu)}{2(1+\nu)}K\left(\varepsilon_v^e\right)= p_r\frac{3(1-2\nu)}{2(1+\nu)}\overline{K}\left(\frac{\xi\left(\varepsilon_v^e\right)}{p_r}\right)^m = p_r\overline{G}\left(\frac{\xi\left(\varepsilon_v^e\right)}{p_r}\right)^m \tag{3.64}$$

where $\overline{G}$ is a non-dimensional material constant that depends on the intrinsic shear modulus of the granular material. The reference stored shear strain energy ψ_s can now be formulated, in the form of the linear elasticity, as:

$$\psi_s\left(\varepsilon_v^e,\varepsilon_s^e\right)=\frac{3}{2}G\left(\varepsilon_v^e\right)\varepsilon_s^{e2}=\frac{3}{2}p_r\overline{G}\left(\frac{\xi\left(\varepsilon_v^e\right)}{p_r}\right)^m\varepsilon_s^{e2} \tag{3.65}$$

Substitute the equations (3.62) and (3.65) into the constituive equations in (3.50) to (3.52), in case of m=0.5, we have:

$$p = \frac{\partial \Psi}{\partial \varepsilon_v^e} = (1 - \vartheta B)\left(p_r A^2 + \frac{3}{4} p_r \overline{G} \overline{K} \varepsilon_s^{e2} \right) \tag{3.66}$$

$$q = \frac{\partial \Psi}{\partial \varepsilon_s^e} = 3(1 - \vartheta B) p_r \overline{G} A \varepsilon_s^e \tag{3.67}$$

$$E_B = \vartheta \psi_r = \vartheta \left(\frac{2 p_r A^3}{3\overline{K}} + \frac{3}{2} p_r \overline{G} A \varepsilon_s^{e2} \right) \tag{3.68}$$

in which $A = \left(\xi \left(\varepsilon_v^e \right) / p_r \right)^{1-m}$. A and ε_s^e in the above can be further expressed in terms of p and q by solving the equations (3.66) and (3.67), which then become: $A = \left(3p\overline{G} + \sqrt{9p^2\overline{G}^2 - 3\overline{G}\overline{K}q^2} \right/ 6(1 - \vartheta B) p_r \overline{G} \Big)^{1/2}$ and $\varepsilon_s^e = q / 3(1 - \vartheta B) p_r \overline{G} A$. To satisfy the mathematical requirement, the expression A must obey $\overline{G}/\overline{K} > q^2 / \left(3p^2 \right)$. While the upper bound of the ratio of shear and mean stress is just the Coulomb friction slope M (i.e., $q = Mp$), it therefore limits the choice of $\overline{G}$ and $\overline{K}$ by:

$$\frac{\overline{G}}{\overline{K}} > \frac{M^2}{3} \tag{3.69}$$

This expression is the same condition proposed by Nguyen and Einav (2009), which they derived by eliminating instability issues (Houlsby 1985; Borja et al 1997; Einav and Puzrin 2004).

The flow rules follow the general forms in equations (3.56)–(3.58), but in which the p, q and E_B are replaced, respectively, by equations (3.66), (3.67) and (3.68).

The yielding function now can be rewritten using equation (3.68) to replace the E_B in equation (3.59):

$$y_{mix} = \vartheta \left(\frac{2 p_r A^3}{3\overline{K}} + \frac{q^2}{6(1 - \vartheta B)^2 p_r \overline{G} A} \right) \frac{(1 - B)^2}{E_c} + \left(\frac{q}{Mp} \right)^2 - 1 \le 0 \tag{3.70}$$

The initial critical crushing pressure p_c in isotropic compression now becomes (i.e., given q=0 in equation (3-68)):

$$p_c = p_r\left(\frac{3\overline{K}E_c}{2p_r\vartheta}\right)^{2/3} \tag{3.71}$$

Generally, the breakage model based on pressure-dependent elasticity proved to better predict soil response (Nguyen and Einav 2009). However, the application of such a model has some limitations that will be discussed later in Section 6.6.

6.3 Breakage model for unsaturated granular materials

To study the dependence of yielding on the degree of saturation in brittle granular materials, the linear elastic breakage model has been integrated within the context of unsaturated soil mechanics (Buscarnera and Einav 2012). Buscarnera and Einav defined the Helmholtz free energy potential as a summation of mechanical (i.e. equation (3.49)) and hydraulic Helmholtz free energy, ψ_r^H. The reason to consider ψ_r^H is due to that the potential energy increases when bulk water, driven by surface tension, moves to the particle surfaces (Tarantino 2010). According to Buscarnera and Einav (2012), such a process depends on the degree of saturation, S_r and evolving grain size (or index B in the context of breakage mechanics). The latter factor might play a dominant role, particularly for unsaturated brittle granular aggregates caused considerable grain crushing. Based on statistical homogenisation, the general form of Helmholtz free energy in unsaturated granular materials is given as:

$$\Psi = \left(1-\vartheta_M B\right)\left(\frac{1}{2}K\varepsilon_v^{e2} + \frac{3}{2}G\varepsilon_s^{e2}\right) + \left(1+\vartheta_H B\right)\psi_r^H\left(S_r\right) \tag{3.72}$$

in which ϑ_M is equivalent to ϑ (see equation (3.20)) while ϑ_H is called hydraulic grading index (Buscarnera and Einav 2012).

By incorporating the equation (3.72) into energy balance equation (3.21), together with an uncoupled energy dissipation form (i.e., the summation of both plastic and breakage dissipation), the constitutive equations can be derived. Consequently, p and

q have the same expressions as in equations (3.50) and (3.51) while the E_B now becomes:

$$E_B = -\frac{\partial \Psi}{\partial B} = \frac{\vartheta_M}{2(1-\vartheta_M B)^2}\left(\frac{p^2}{K}+\frac{q^2}{3G}\right) - \vartheta_H \psi_r^H(S_r) \tag{3.73}$$

The flow rules are the same as equations (3.56) and (3.57), except that in equation (3.58) the E_B is replaced by equation (3.73).

By substituting the above E_B into equation (3.59), a new yielding function for unsaturated brittle granular materials is obtained:

$$y = \frac{\vartheta_M}{2E_c}\left(\frac{1-B}{1-\vartheta_M B}\right)^2\left(\frac{p^2}{K}+\frac{q^2}{3G}\right)+\left(\frac{q}{Mp}\right)^2 - \left(1+\frac{\vartheta_H \psi_r^H(S_r)(1-B)^2}{E_c}\right) \le 0 \tag{3.74}$$

The mean effective stress at the onset of grain breakage in an unsaturated granular soil is now given by (i.e., q=0 and B=0 in equation (3.74)):

$$p_c^{unsat} = \sqrt{\frac{2KE_C}{\vartheta_M}}\sqrt{1+\vartheta_H \frac{\psi_r^H(S_r)}{E_C}} \tag{3.75}$$

A comparison has been made between this model's predictions and the experimental data regarding the suction-net isotropic stress plane (Buscarnera and Einav 2012). Satisfactory agreement was found.

6.4 Breakage model based on large strain deformation

A more recent general constitutive model of crushable granular materials has been developed within the context of large deformations (Rubin and Einav 2011). This idea originated from the widely known fact that the critical effects of brittle granular materials depend on their loading history and evolving grain size (or GSD). A particular feature of this model is that it is able to explicitly explain the yielding dependence on porosity. Moreover, many other important mechanisms of the brittle granular materials are also described, such as: (1) stiffness and critical comminution dependent on grain crushing and porosity; (2) competition between granular dilation

(due to inelastic distortion) and compaction (due to crushing); and (3) jamming transition between solid and gaseous states.

6.5 Mixture breakage model

The previous models (Sections 6.1–6.4), derived from the theory of breakage mechanics, are for homogeneous granular materials. As for the mechanics of granular mixtures, Einav and Valdes (2008) extended the breakage mechanics theory by taking into account the strength of the independent homogeneous species. This allowed the researchers to predict the critical comminution pressure, breakage evolution, and yield pressure increase/hardening with increasing breakage in granular mixtures. The predictions for dissimilar constituent species were consistent with corresponding experimental findings.

6.6 Current development of a breakage model with cementation

Group members from University of Sydney are now working on a new model to study the behaviour of cemented granular materials. A feature of this model is to adopt a novel measurable property of damage for the cement phase, in addition to the breakage property used in those existing breakage models. Thus, the ability of the breakage model (and breakage theory) would have been rigorously extended to include the ductile responses of cemented granular materials. The formulation of the model is also thermodynamically consistent, with explicit links between the internal variables (breakage and damage) and the evolving microstructure of the material. In addition, only the plastic strain rate is considered with no need to define the total plastic strain. This provides a sounded insight into the physical nature of the mechanical behaviour of cemented granular materials, by comparing many existing models that only rely on plastic strain.

6.7 Discussion

The focus, in this thesis, is on a dry crushable granular material upon which either the linear elastic breakage model or breakage model based on pressure-dependent elasticity will be used. Although the latter model enhances the prediction of the model's response for granular materials, it has several disadvantages. First, due to

mathematical limitations, the choices of $\overline{K}$ and $\overline{G}$ are limited (i.e. (3.69)). However, such a limitation is not physically meaningful as both properties might not always necessarily be within such a mathematical scale. Second, the derivation of $G\left(\varepsilon_v^e\right)$is based on the assumption of constant *v*. However, this is merely a simplification, which might not be necessary in reality. Probably the most significant drawback happened when implementing the breakage model (based on pressure-dependent elasticity) into a finite element code. Due to the model's high non-linearity even within elastic regions, the stiffness of the model at low pressure (e.g., the artificial reference pressure of 1kPa) is too small. This easily causes large mesh distortions in finite element simulation, and subsequently terminating the calculation or producing unreliable results. On the other hand, such a small amount of stiffness, due to low pressures, does not really reflect the true response of granular materials.

Having said that, all research work in this thesis is based on the linear elastic breakage model. Our motivation is to start with the simplest possible model to conceptually discover and identify the main mechanisms, before we turn to a more complicated model. Nevertheless, since the studied problems already involve the complexity at the level of geometry and boundary conditions, we consider the results obtained in this thesis valuable and meaningful. It will be shown in the latter chapters that this simple model proves to be very practical and attractive. The main reason might be that the simple model is already sufficiently informative for capturing the essential underlying features (i.e., evolving GSD) of the behaviour of granular materials without adding *ad hoc* fitting parameters to the model. As for the rest of its features, including pressure-dependent elasticity, they will be good supplements to enhance the model response if the drawbacks, mentioned in the previous paragraph, can be overcome.

Also notice that the used linear elastic breakage model does not reflect the dependence of the soil behavior on density, and does not directly reflect the recent finding by Altuhafi and Coop (2011) that the relation between breakage and pressure also depends on the porosity. However, more recently, such effects were explained by Rubin and Einav (2011), within the thermodynamics framework of breakage mechanics. Their work illustrated that by taking porosity dependent bulk modulus, in a form similar to that proposed by Hardin and Black (1966) and Viggiani and Atkinson (1995), the critical comminution pressure could be approximated by a linear

dependence on the solid fraction. In addition, one might study the correlation between elastic moduli and porosity, such that the porosity-dependence elastic moduli would be further taken into account within thermodynamics. Those ideas motivate our future research to develop more rigorous simplified breakage model into practical application.

7 Summary

This chapter presented a thermodynamic approach to the constitutive modelling of granules using breakage mechanics. The theory rigorously incorporates the evolving GSD (through B) to construct constitutive models for crushable granular materials. The various models, based on the breakage mechanics theory, were explained; either briefly or in detail. The rigour and novelty of the breakage mechanics theory can be attributed to five key points, as highlighted below (Einav 2007a):

1) The ultimate cumulative GSD, $F_u(x)$, determines the critical state (this explains the non-uniqueness of the critical-state pressure-porosity relation in sand, see Rubin and Einav (2011)). Although not necessary, it is practical to employ a fractal power law $F_u(x)$ (Sammis et al. 1986; McDowell et al. 1996; Ben-Nun and Einav 2010).

2) Breakage, B, is introduced to predict the current cumulative GSD by mass ($F(x,B)$) through a linear scaling between the initial ($F_0(x)$) and ultimate cumulative GSDs ($F_u(x)$), as shown in equation (3.2).

3) Through statistical homogenisation, the macroscopic specific elastic strain energy stored is the average of such energies stored in the various size fractions, determined by the current GSD, $p(x,B)$, as illustrated in Section 3 in this chapter.

4) The specific elastic strain energy stored in larger grains is greater than in smaller grains. To a first order this energy is in proportion to the grains' surface area, as elaborated in Section 4 in this chapter.

5) Breakage dissipation from grain crushing is equal to the loss in the residual breakage energy (the residual breakage energy reflects the energy left in the system to crush particles towards the ultimate GSD $F_u(x)$), as explained in detail in Section 5.3 in this chapter.

It is important to note that breakage mechanics, though developed initially for the purpose of geotechnical modelling of sands, was never intended to be limited to this single discipline. In the mining industry, for example, the comminution modelling of minerals through a roller mill is also applicable to breakage mechanics (see Chapter VII). Furthermore, as stated by Einav (2007d), breakage mechanics offers a very promising mean of study access to deal with various granular modelling, i.e., pasta-sand or wheat-sand, by simply changing physical parameters and boundary conditions as required.

Chapter IV

Finite element numerical implementation of the linear elastic breakage model

1 Introduction

Finite element (FE) numerical implementation is essential in order to maximise the use of constitutive models in engineering applications. In our study, the linear elastic breakage model of breakage mechanics is incorporated into the commercial FE code, abaqus. abaqus provides two user subroutines, the so-called 'umat' and 'vumat', to allow users to implement their own user defined constitutive models. The finite element analysis (FEA) for umat employs implicit schemes—i.e., the finite element momentum balance or equilibrium equations are solved implicitly—while for vumat, the FEA uses explicit schemes. Regardless of whether the FEA scheme is implicit or explicit, constitutive equations are always needed to update the stress at the end of the time increment. Moreover, in implicit FE codes the solution (mostly uses the Newton-Raphson method for the momentum balance or equilibrium equations), requires that the tangent stiffness matrix (the so-called Jacobian) be calculated in addition to the constitutive equations. In explicit FE, however, the tangent stiffness matrix is not necessary.

The purpose in this chapter, therefore, is to present a procedure to implement the linear elastic breakage constitutive equations for umat and vumat. Especially for umat, the additional tangent stiffness matrix is needed. To verify the model's implementation it is tested using single and multiple elements under isotropic and triaxial shear tests in both drained and undrained conditions. Finally, the numerical results are compared with experimental shear tests to demonstrate the ability of the linear elastic breakage model to predict the mechanical responses of crushable granular aggregates.

2 Brief review of stress return algorithm

Different stress return algorithms have been proposed to integrate the constitutive relations to compute the increments in stresses and state variables. One of the relatively easy algorithms is the so-called 'explicit scheme'. This integration scheme enables the updated quantities at time $t+\Delta t$ to be calculated based on known quantities at time t. Its notable advantage is its simplicity in FE implementation and it has been commonly used in goemechanics (Abbo and Sloan 1996; Sheng et al. 2000; Sheng and Sloan 2001; Luccioni et al. 2001; Zhao et al. 2005). However, the yield condition is not ensured at time $t+\Delta t$ in such a forward integration process. As a result, the calculated quantities, for instance the plastic multiplier at time $t+\Delta t$, is not satisfied in the yield condition. This causes the solution, over many time increments, to drift away from the yielding surface (Dunne and Petrinic 2005). Moreover the time step size, Δt, cannot be too large. Otherwise, incorrect results will be computed. Therefore, the application of explicit schemes is usually limited to some simple constitutive models (e.g., the linear elastic model). For complex non-linear constitutive models, the explicit scheme is usually neither efficient nor capable. Nevertheless, some researchers have extended the performance of the explicit scheme. A good example is the explicit method with automatic substepping and error control proposed by Sloan (1987). Sloan aimed for conventional elastoplastic models in which the mechanical responses inside the yield surface are linear elastic. This work was recently further developed and extended to cover the non-linear elastic behaviour inside the yield surface (Sloan et al. 2001).

As opposed to the explicit scheme, another integration algorithm is called the 'full implicit scheme'. In detail, an (elastic) trial stress increment is first computed to obtain the updated trial stress, $\sigma^{tr}_{t+\Delta t}$. The trial stress will be outside the yield surface if the yield condition is not satisfied. On this occasion, the trial stress is then updated with a plastic correction to bring it back onto the yield surface at time $t+\Delta t$. This is known as the stress return process that must be solved iteratively. A most widely used method to solve the stress return process is the Newton method. Since the yield condition is satisfied at the end of the time increment, the full implicit method can avoid 'drift' from the yield surface, which occurs in the explicit scheme. In addition,

the full implicit scheme allows for the use of significantly larger time increments, which generally leads to far quicker solutions (Dunne and Petrinic 2005). The full implicit method has been widely used in geomechanics (Simo and Taylor 1985; Gens and Potts 1988; Borja 1991; Jeremić and Sture 1997; Borja et al. 2001).

The constitutive equations can also be integrated using a backward Euler return algorithm (Crisfield 1991; Alawaji et al. 1992; Simo and Hughes 1997; Simo 1998; Tamagnini et al. 2002). This might be called a 'semi-implicit' method because it still follows the idea of stress return but uses the first-order of Taylor's expansion of the yield function. This is much simpler than the full implicit method regarding the stress return process because no iteration is strictly necessary to predict the final stresses. Therefore the semi-implicit method makes the FE implementation much easier compared with full implicit method. Moreover, the semi-implicit method enables quantities to be updated almost as accurately as those obtained from the full implicit method. Due to its simplicity, stability and high level of accuracy, the semi-implicit integration method is used to implement the breakage model.

It is also interesting to note that a novel rate-dependent algorithm, i.e., Perzyna's (1963 and 1966) model could also be used to predict the rate-independent response (e.g., Simo 1989; Needleman 1988). Although such a model is highly dependent on rate parameters, it is the simplest implementation ever used in the stress return algorithm. It is therefore unnecessary to use either explicit or implicit methods to obtain the non-negative multiplier, provided that the rate parameters used in Perzyna's model are correct. The rate-independent response can then be accurately described by such a rate-dependent method. All in all, it provides a useful strategy to simplify the stress return algorithm given the correctly calibrated parameters; otherwise a rate-dependent response, but not a rate-independent response, may result.

3 Finite element implementation

The numerical implementation of the linear elastic breakage constitutive model described in Chapter III is presented for FE implementation. The tensorial form of the triaxial model is used, and here the sign convention follows that of solid mechanics, where compression is negative for implementation in abaqus. The triaxial stresses and strains are written in terms of the stress and strain invariants as follows:

$$p = -\frac{1}{3}\sigma_{kk} \tag{4.1}$$

$$q = \sqrt{\frac{3}{2}s_{ij}s_{ij}} \tag{4.2}$$

$$\varepsilon_v = -\varepsilon_{kk} \tag{4.3}$$

$$\varepsilon_s = \sqrt{\frac{2}{3}e_{ij}e_{ij}} \tag{4.4}$$

where (δ_{ij} is the Kronecker delta):

$$s_{ij} = \sigma_{ij} - \frac{\sigma_{kk}}{3}\delta_{ij} \tag{4.5}$$

$$e_{ij} = \varepsilon_{ij} - \frac{\varepsilon_{kk}}{3}\delta_{ij} \tag{4.6}$$

The elastic component of the constitutive equations (3.48–3.49 in Chapter III) of the model can be rewritten in tensorial form:

$$\sigma_{ij} = (1 - \vartheta B)D_{ijkl}\varepsilon^e_{kl} \tag{4.7}$$

with the yield function given as:

$$y = \frac{\vartheta}{2E_c}\left(\frac{p^2}{K} + \frac{q^2}{3G}\right)\left(\frac{1-B}{1-\vartheta B}\right)^2 + \left(\frac{q}{Mp}\right)^2 - 1 \le 0 \tag{4.8}$$

and flow rules:

$$\mathrm{d}\varepsilon^p_{ij} = \delta\lambda\left[-\frac{2(1-B)^2 E_B \sin^2\omega}{pE_c}\frac{\delta_{ij}}{3} + \frac{3s_{ij}}{M^2p^2}\right] = \delta\lambda Q_{ij} \tag{4.9}$$

$$\mathrm{d}B = \delta\lambda\frac{2(1-B)^2\cos^2\omega}{E_c} = \delta\lambda R \tag{4.10}$$

The aim is to calculate the stress increment, $\mathrm{d}\sigma_{ij}$, given the current state of the material point at X (Figure 4.1) and the strain increment, $\mathrm{d}\varepsilon_{ij}$, obtained from the non-linear finite element analysis. We consider the case that yielding occurs, indicated by $y^{\text{trial}} > 0$ at trial point Y. This trial stress point is obtained by assuming linear elastic behaviour with secant stiffness $(1-\vartheta B)D_{ijkl}$ for the strain increment $\mathrm{d}\varepsilon_{ij}$, resulting in the trial stress increment $\mathrm{d}\sigma_{ij}^{\text{trial}} = (1-\vartheta B)D_{ijkl}\mathrm{d}\varepsilon_{kl}$. By performing a Taylor expansion of the yield function (4.8) at the trial point Y (Figure 4.1) we obtain:

$$y = y^{\text{trial}} + \frac{\partial y}{\partial B}\mathrm{d}B + \left(\frac{\partial y}{\partial p}\frac{\partial p}{\partial \sigma_{ij}} + \frac{\partial y}{\partial q}\frac{\partial q}{\partial \sigma_{ij}}\right)\mathrm{d}\sigma_{ij} = y^{\text{trial}} + \frac{\partial y}{\partial B}\mathrm{d}B + M_{ij}\mathrm{d}\sigma_{ij} \tag{4.11}$$

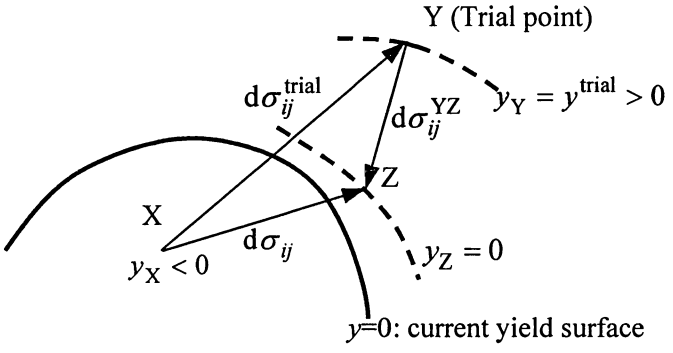

Figure 4.1 Schematics of the stress return algorithm.

Substituting the flow rules (4.9–4.10), and the stress increment in the form:

$$\mathrm{d}\sigma_{ij} = -(1-\vartheta B)D_{ijkl}\mathrm{d}\varepsilon_{kl}^{p} - \frac{\vartheta\sigma_{ij}}{1-\vartheta B}\mathrm{d}B \tag{4.12}$$

into (4.11) results in (note that the total strain increment has been used to obtain the trial point Y, and hence there is no total strain increment beyond this trial point):

$$y = y^{\text{trial}} + \left[\frac{\partial y}{\partial B}R - M_{ij}\left((1-\vartheta B)D_{ijkl}Q_{kl} + \frac{\vartheta\sigma_{ij}}{1-\vartheta B}R\right)\right]\delta\lambda \tag{4.13}$$

where Q_{kl} and R are defined in equations (4.9–4.10). It is implied here that all variables and quantities in equation (4.13) are evaluated at trial point Y. Enforcing the yield condition at point Z, $y = y_{\text{Z}} = 0$, we can obtain the multiplier, $\delta\lambda$, in the form:

$$\delta\lambda = \frac{-y^{\text{trial}}}{\dfrac{\partial y}{\partial B}R - M_{ij}\left((1-\vartheta B)D_{ijkl}Q_{kl} + \dfrac{\vartheta\sigma_{ij}}{1-\vartheta B}R\right)} = \frac{-y^{\text{trial}}}{N} \tag{4.14}$$

The stress increment, $\mathrm{d}\sigma_{ij}^{\text{YZ}}$, then follows as:

$$\mathrm{d}\sigma_{ij}^{\text{YZ}} = -\left[(1-\vartheta B)D_{ijkl}Q_{kl} + \frac{\vartheta\sigma_{ij}}{1-\vartheta B}R\right]\delta\lambda \tag{4.15}$$

The total stress increment, $\mathrm{d}\sigma_{ij}$, is obtained as the sum of $\mathrm{d}\sigma_{ij}^{\text{trial}}$ and $\mathrm{d}\sigma_{ij}^{\text{YZ}}$ (Figure 4.1):

$$\mathrm{d}\sigma_{ij} = \mathrm{d}\sigma_{ij}^{\text{trial}} + \mathrm{d}\sigma_{ij}^{\text{YZ}} \tag{4.16}$$

Due to the linearisation of the yield function in (4.11), the returned stress point Z usually does not lie on the new yield surface, e.g., $y\left(B|_Z, p|_Z, q|_Z\right) \neq 0$. Repetition of the above process, e.g., linearising the yield function at point Z and then following the same algorithm, is a simple way to bring the stress point closer to the yield surface. Improvements to the accuracy of the above algorithm can also be made by dividing the total strain increment, $\mathrm{d}\varepsilon_{ij}$, into sub-increments, and applying the above algorithm to each sub-increment. The above algorithm has been implemented in the commercial finite element package abaqus (2010) in the forms of umat and vumat subroutines. As an example, the vumat has been presented in Appendix B at the end of this thesis. Readers may straightforwardly convert vumat into umat with slight modification by following the format of umat.

4 Tangent stiffness matrix

Implicit finite element analysis (relevant to umat) using the Newton-Raphson iterative techniques requires the formulation of the tangent stiffness matrix (Jacobian). This matrix is of importance in increasing the rate at which convergence is achieved. The derivation of Jacobian is quite straightforward by starting from the stress-strain relationship (4.7) written in:

$$\begin{aligned} \mathrm{d}\sigma_{ij} &= (1-\vartheta B)D_{ijkl}\left(\mathrm{d}\varepsilon_{kl}-\mathrm{d}\varepsilon_{kl}^{p}\right)-\vartheta D_{ijkl}\varepsilon_{kl}^{e}\mathrm{d}B \\ &= (1-\vartheta B)D_{ijkl}\mathrm{d}\varepsilon_{kl}-(1-\vartheta B)D_{ijkl}\mathrm{d}\varepsilon_{kl}^{p}-\vartheta D_{ijkl}\varepsilon_{kl}^{e}\mathrm{d}B \end{aligned} \tag{4.17}$$

Substituting (4.9) and (4.10) into the above:

$$\mathrm{d}\sigma_{ij} = (1-\vartheta B)D_{ijkl}\mathrm{d}\varepsilon_{kl}-(1-\vartheta B)D_{ijkl}\delta\lambda Q_{ij}-\vartheta D_{ijkl}\varepsilon_{kl}^{e}\delta\lambda R \tag{4.18}$$

Using the following consistency condition:

$$\mathrm{d}y = \frac{\partial y}{\partial B}\mathrm{d}B+\left(\frac{\partial y}{\partial p}\frac{\partial p}{\partial \sigma_{ij}}+\frac{\partial y}{\partial q}\frac{\partial q}{\partial \sigma_{ij}}\right)\mathrm{d}\sigma_{ij} = \frac{\partial y}{\partial B}\mathrm{d}B+M_{ij}\mathrm{d}\sigma_{ij} \tag{4.19}$$

Substituting the stress increment (4.17) and flow rules (4.9–4.10) results in:

$$\mathrm{d}y = (1-\vartheta B)M_{ij}D_{ijkl}\mathrm{d}\varepsilon_{kl}-\left(\frac{\partial y}{\partial B}R-M_{ij}\left((1-\vartheta B)D_{ijkl}Q_{kl}+\frac{\vartheta\sigma_{ij}}{1-\vartheta B}R\right)\right)\delta\lambda \tag{4.20}$$

The plasticity/breakage multiplier is then:

$$\delta\lambda = \frac{(1-\vartheta B)M_{ij}D_{ijkl}\mathrm{d}\varepsilon_{kl}}{\frac{\partial y}{\partial B}R-M_{ij}\left((1-\vartheta B)D_{ijkl}Q_{kl}+\frac{\vartheta\sigma_{ij}}{1-\vartheta B}R\right)} = \frac{T_{kl}\mathrm{d}\varepsilon_{kl}}{N} \tag{4.21}$$

Placing equation (4.21) into (4.18) we have:

$$\mathrm{d}\sigma_{ij} = \left((1-\vartheta B)D_{ijmn}-(1-\vartheta B)D_{ijkl}Q_{kl}\frac{T_{mn}}{N}-R\vartheta D_{ijkl}\varepsilon_{kl}^{e}\frac{T_{mn}}{N}\right)\mathrm{d}\varepsilon_{mn} \tag{4.22}$$

T_{mn} is defined in equation (4.21). Thus the tangent stiffness matrix (for umat only) is:

$$X_{ijmn} = (1-\vartheta B)D_{ijmn}-(1-\vartheta B)D_{ijkl}Q_{kl}\frac{T_{mn}}{N}-R\vartheta D_{ijkl}\varepsilon_{kl}^{e}\frac{T_{mn}}{N} \tag{4.23}$$

The used notations and derivatives are as follow:

$$\frac{\partial y}{\partial B} = \frac{\vartheta(1-B)}{E_c(1-\vartheta B)^2}\left(\frac{p^2}{K}+\frac{q^2}{3G}\right) \tag{4.24}$$

$$\frac{\partial y}{\partial p} = \frac{p\vartheta}{KE_c}\left(\frac{1-B}{1-\vartheta B}\right)^2-\frac{2q^2}{M^2p^3} \tag{4.25}$$

$$\frac{\partial y}{\partial q}=\frac{q\vartheta}{3GE_c}\left(\frac{1-B}{1-\vartheta B}\right)^2+\frac{2q}{M^2p^2} \tag{4.26}$$

$$\frac{\partial p}{\partial \sigma_{ij}}=\frac{\delta_{ij}}{3} \tag{4.27}$$

$$\frac{\partial q}{\partial \sigma_{ij}}=\frac{\partial q}{\partial s_{kl}}\frac{\partial s_{kl}}{\partial \sigma_{ij}}=\frac{3}{2}\frac{s_{ij}}{q} \tag{4.28}$$

$$M_{ij}=\left(\frac{\partial y}{\partial p}\frac{\partial p}{\partial \sigma_{ij}}+\frac{\partial y}{\partial q}\frac{\partial q}{\partial \sigma_{ij}}\right) \tag{4.29}$$

$$T_{kl}=(1-\vartheta B)M_{ij}D_{ijkl}\mathrm{d}\varepsilon_{kl} \tag{4.30}$$

$$N=\frac{\partial y}{\partial B}R-M_{ij}\left((1-\vartheta B)D_{ijkl}Q_{kl}+\frac{\vartheta\sigma_{ij}}{1-\vartheta B}R\right) \tag{4.31}$$

5 Verification of implementations

To verify the FE implementation, it is necessary to test the model's response using single or multiple quadratic, fully integrated 8-node axisymmetric elements, under conditions of strain and load control. To do this, the following four numerical experiments were conducted and the results obtained were compared with solutions from the triaxial model. As the material is considered homogenous, the results of the model from single element and multiple elements were found to be identical. Therefore, only the single-element model's results are presented here. The geometry of the single-element model for all verification cases is sketched in Figure 4.2, in which only a quarter of the whole is modelled; while the boundary conditions vary from case to case, which are illustrated in each case. The parameters, if not specified, are from Nguyen and Einav's parameters (2009) as listed Table 4.1.

Table 4.1 Model parameters for numerical experiments

Sample name	K(MPa)	G(MPa)	E_c (MPa)	M	ω	ϑ
Adamswiller sandstone	4608	4710	3.53	1.5	45°	0.9

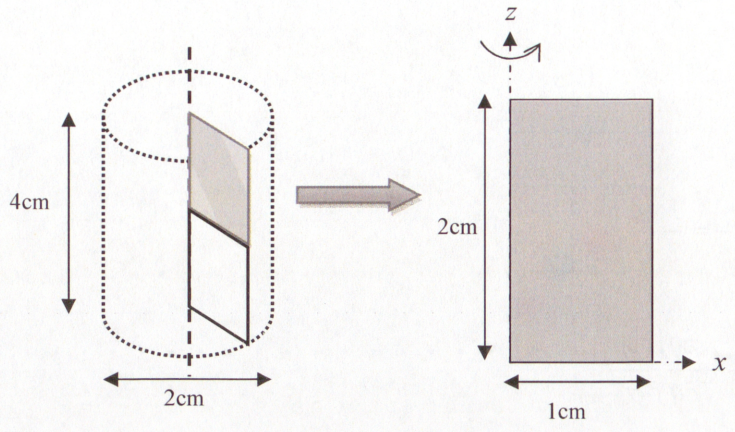

Figure 4.2 Axisymmetric finite element mesh (one element). Considering the geometry of the model, modelling of a quarter of the whole (the grey part) is sufficient.

5.1 Isotropic loading condition

As the simplest case, the isotropic loading condition is first applied to validate the implementation. The model's boundary condition is shown in Figure 4.3. Increase confining pressure p until the expected volumetric strain of ε_v=0.5 achieves. The model's mechanical responses are compared in Figure 4.4.

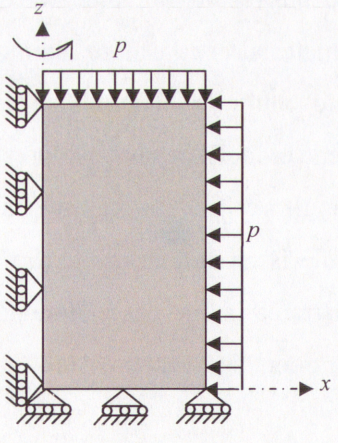

Figure 4.3 Boundary conditions of isotropic loaded specimen

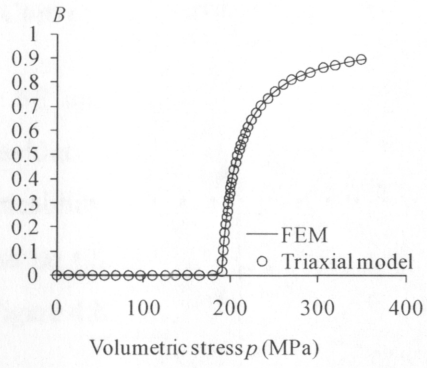

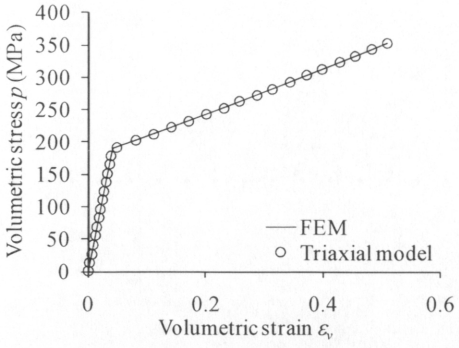

(a) (b)

Figure 4.4 Validation of implementation in terms of (a) p-B and (b) p-ε_v relationship, under isotropic compression condition

5.2 Isotropic loading-unloading-reloading condition

While based on the same geometry used in Figure 4.3, first compress the sample until ε_{v1}=0.3, then unload the model until ε_{v2}=0.15 (here 'unloading' is realised by adding an increased isotropic tensile pressure), and finally recompress the model until ε_{v3}=0.6.

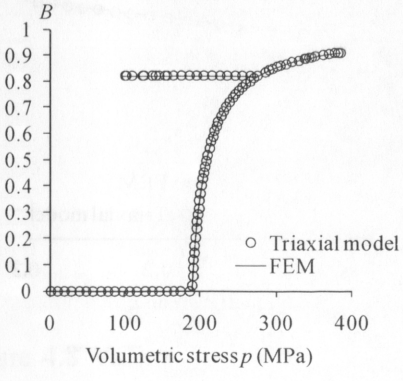

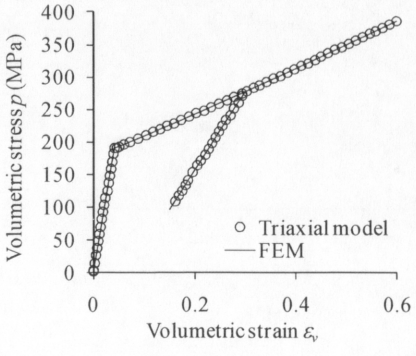

(a) (b)

Figure 4.5 Validation of implementation in terms of (a) p-B and (b) p-ε_v relationship, under isotropic loading, unloading, and reloading conditions.

5.3 Conventional drained loading with constant confining pressure

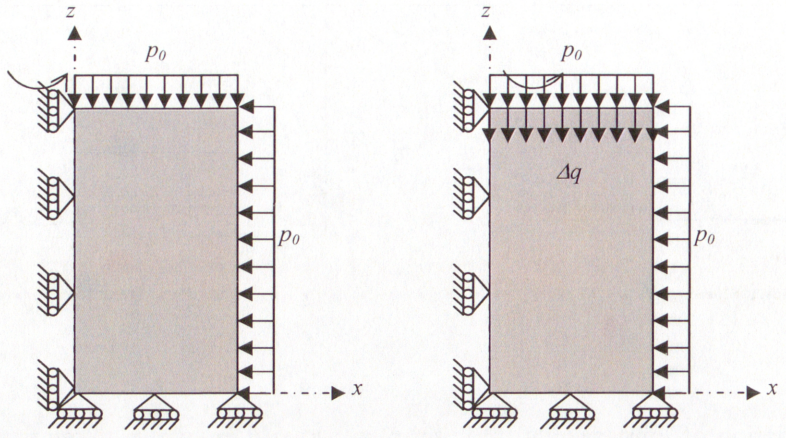

(a) Isotropic stage (b) Shear stage

Figure 4.6 Boundary conditions of conventional shear test

The boundary conditions for this case are illustrated in Figure 4.6, in which the model first under an initial isotropic stress of p_0=100MPa. The model is then subjected to an increased shear stress Δq till the shear strain ε_s=0.3. The model's responses to the triaxial model and finite element model (FEM) are compared in Figure 4.7.

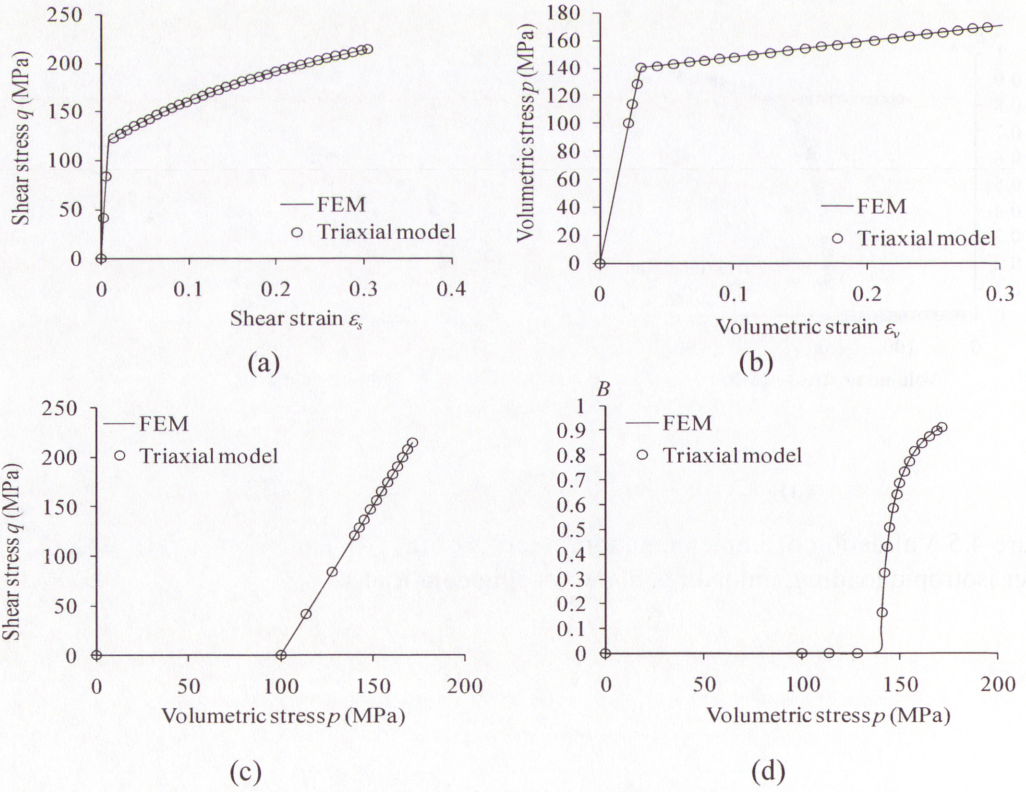

Figure 4.7 Validation of implementation in terms of (a) q-ε_s, (b) p-ε_v, (c) p-q and (d) p-B relationship, under conventional drained loading condition.

5.4 Conventional undrained loading with constant confining pressure

The FE undrained model is also based on Figure 4.6. To simulate the undrained behaviour of the soil model, all boundaries are impermeable. Therefore the permeability, k, can be defined arbitrarily. Let us take k=0.002m/s. Increase the shear stress Δq till the ε_s=1.0. The results from the FEM and triaxial models are compared in Figure 4.8.

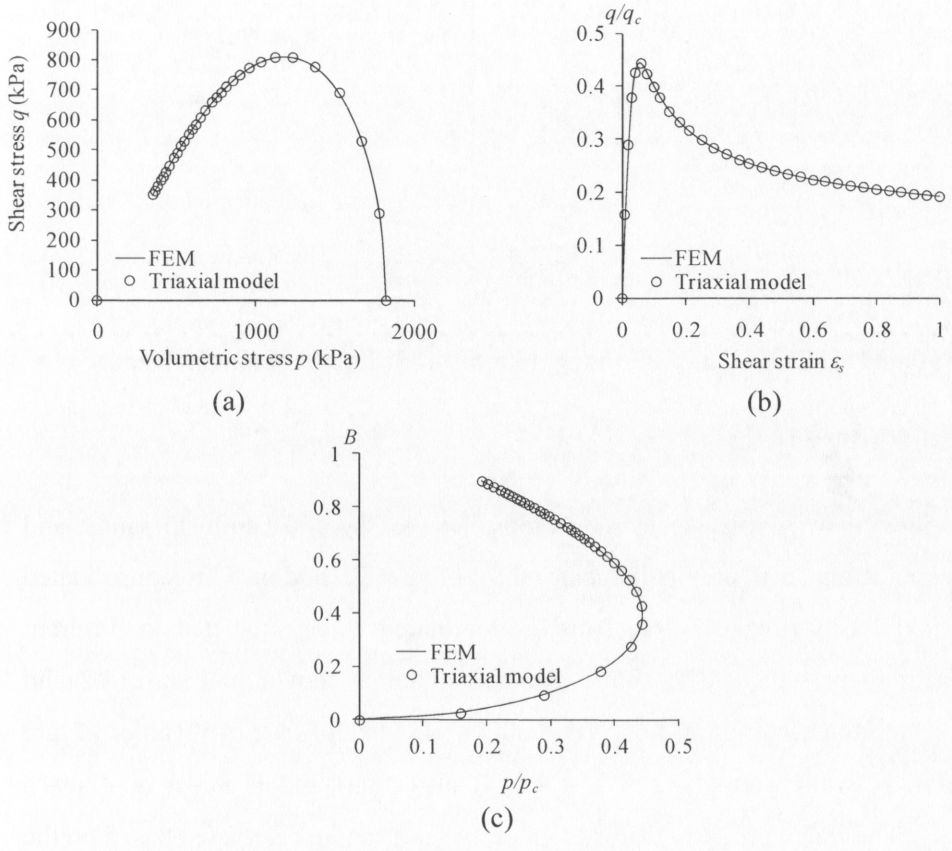

Figure 4.8 Validation of implementation in undrained loading condition in terms of (a) p-q, (b) normalized shear stress and shear strain relationship, q/p_c-ε_s and (c) normalized volumetric stress and breakage relationship, p/p_c-B. Recall the $p_c = \sqrt{2KE_c/\vartheta}$ (Section 6.1, Chapter III). The following parameters used: K=30000kPa, G=10000kPa, E_c=50kPa, M=1, ϑ=0.9 and ω=0° (indicating no plastic volumetric strain).

5.5 Accuracy verification

To validate the accuracy of the implementation, different $\Delta\varepsilon_s$ (i.e. from 10^{-1} to 10^{-5}) are selected for the conventional undrained test. As an example, only the results of q/p_c-ε_s and p/p_c-B are plotted in Figure 4.9. It can be seen that good convergence

appears for $\Delta\varepsilon_s$ less or equal to 10^{-2}. For $\Delta\varepsilon_s$ equal or less than 10^{-3}, the results coincide with each other. Given $\Delta\varepsilon_s=10^{-3}$, the corresponding yielding value, y (equation (4.11)) is around 10^{-4} that satisfies the requirement of numerical accuracy. Therefore, all simulations throughout the thesis consider the both conditions of $\Delta\varepsilon_s=10^{-3}$ and $y=10^{-4}$ as accuracy criterion.

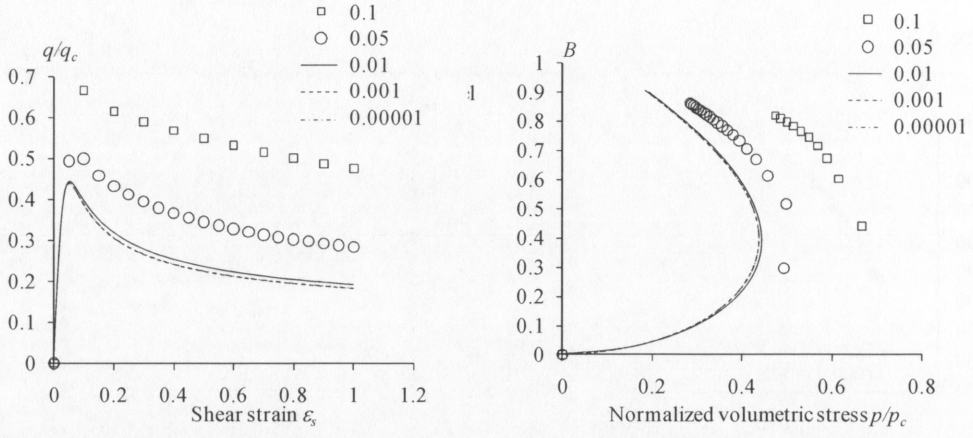

Figure 4.9 Validation of accuracy in terms of different increment size

6 Model prediction

The behaviour of two typical calcareous soils, Dog's Bay and Chiibishi sands, and Bentheim sandstone are predicted using the above FE model. The consolidated drained triaxial behaviour of these soils are simulated when subjected to different initial confining pressures. The single-element model is shown in Figure 4.2 and boundary conditions in Figure 4.6. The model's parameters listed in Table 4.2 are mainly from Kuwajima et al. (2009), Coop et al. (2004) and Baud et al. (2004), respectively. The index property ϑ for Dog's Bay sand can be calculated based on the initial and ultimate cumulative GSDs, while that for Chiibishi sand is determined from the experimentally given initial cumulative GSD, and an assumed fractal ultimate cumulative GSD in equation (3.5) with the fractal dimension α taking the value α = 2.7 (Turcotte 1986). The high value, ϑ, for Bentheim sandstone implies very poor initial grading in the test.

Table 4.2 Model parameters for calcareous sand

Crushable sand	K(MPa)	G(MPa)	p_c (MPa)	M	ω	ϑ
Chiibishi sand	17.8	14.5	1.3	1.77	30°	0.2
Dog's bay sand	25	14	0.6	1.65	38°	0.65
Bentheim sandstone	11522	7513	390	1.7	70°	0.9

Figures 4.10–4.12 show the agreement between numerical predictions and experimental observations. From those examples, we can see that the linear elastic breakage model works very well for crushable granular aggregates, independent of their hardnesses.

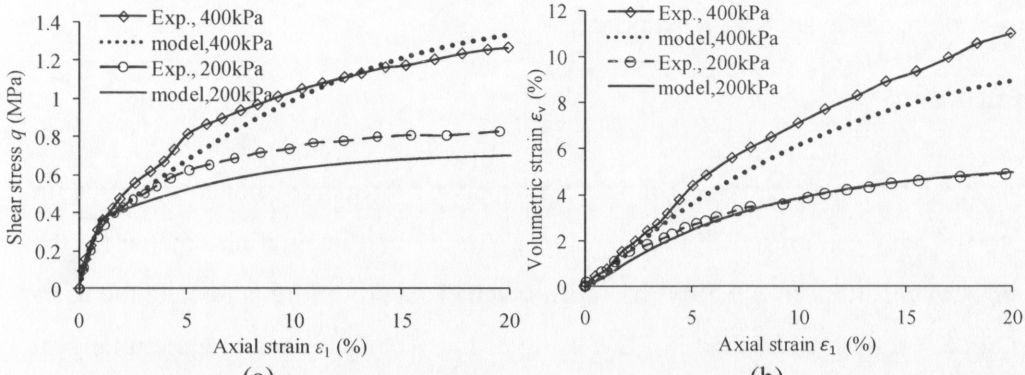

Figure 4.10 Model predictions of the mechanical response of Dog's Bay sand for drained triaxial shear tests at different initial confining pressures: (a) shear stress-axial strain and (b) volumetric strain-axial strain (experimental data from Kuwajima et al. 2009)

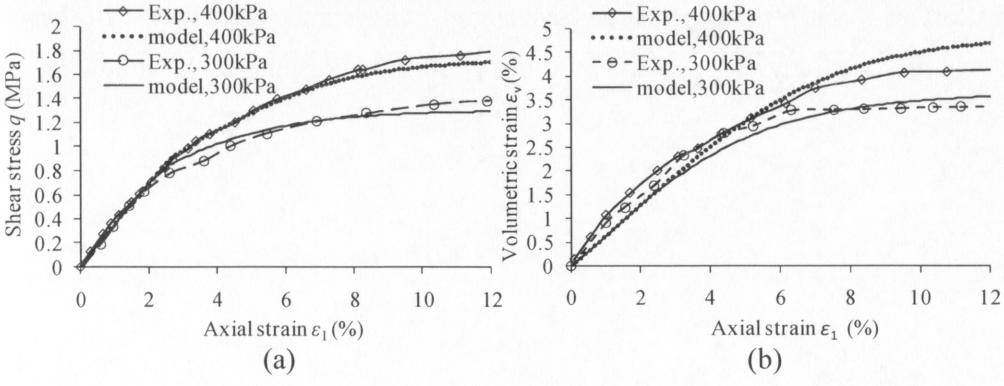

Figure 4.11 Model predictions of the mechanical response of Chiibishi sand under drained triaxial shear tests at different initial confining pressures: (a) shear stress-axial strain and (b) volumetric strain-axial strain (experimental data from Kuwajima et al. 2009)

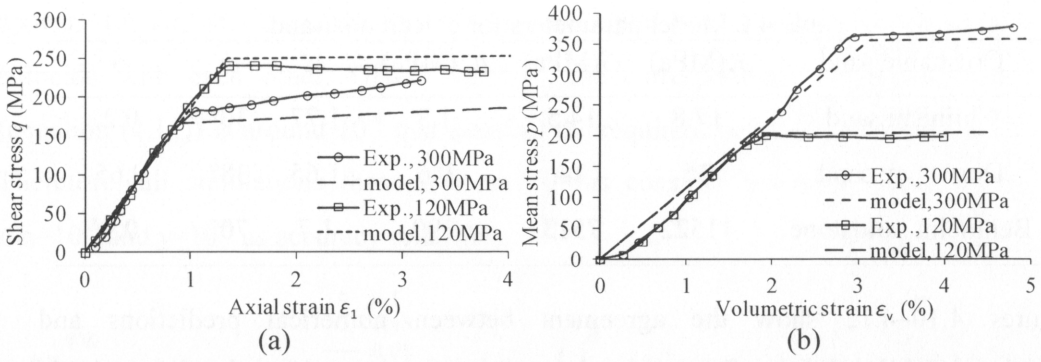

Figure 4.12 Model predictions of the mechanical response of Bentheim sandstone under drained triaxial shear tests at different initial confining pressures: (a) shear stress-axial strain and (b) mean stress-volumetric strain (experimental data from Baud et al. 2004). More comparisons can be seen in Das et al. (2011), which focuses on compaction bands in such hard material.

7 Summary

The numerical implementation of the linear elastic breakage model proposed in Chapter III has been presented in this chapter. An implicit integration scheme for the incremental constitutive equations has been given. This procedure is to code the user-subroutines of umat and vumat in FEM using abaqus. The additional required tangent stiffness matrix, exclusively for the umat, has also been derived. The FE implementations have been validated against the triaxial model tests under different loading paths. Next, the model's ability to predict soil behaviour is illustrated by comparing three samples of crushable material of varying hardness, ranging from very soft (calcareous sand) to very hard (sandstone). This implementation will be extensively used to study more complex problems of grain crushing in the following chapters.

Chapter V

End-bearing capacity of pile into crushable soils

1 Introduction

Conventional bearing capacity equations predict increasing resistance with increasing friction angle (e.g. Terzaghi 1943). Accordingly, given the relatively high friction angle of calcareous sand, it can be expected that its resistance to pile penetration would be high. However, in such crushable soils the bearing capacity is much lower than estimated by conventional equations (Poulos and Chua 1985; Golightly and Hyde 1988; Yu 2000). For example, experiments have shown that for comparable tip resistances, pile displacements in highly crushable materials are much larger than in non-crushable soils (Kuwajima et al. 2009). This is because grain crushing helps the soil to accommodate the new volumetric intrusion by the pile. The result is an overall reduction in the total volume, defined by the soil compressibility. In crushable sands, the compressibility is governed by the way the GSD evolves, as observed experimentally (Datta et al. 1980), and rationalised theoretically (Einav 2007a). The GSD influences the strength and stress-strain behaviour of the soil (Hardin 1985; Lade et al. 1996) and subsequently affects the pile's end-bearing capacity. For example, using geotechnical centrifuge tests of a model pile driven into crushable soils, McDowell and Bolton (2000) noticed that well-graded soils' resistance to penetration is higher than that of uniformly poorly graded soils.

The importance of soil crushability to the design and construction of pile foundations was highlighted from a practical standpoint (Datta et al. 1980; Poulos and Chua 1985; Alba and Audibert 1999). Various laboratory and in situ field tests: e.g. a pile load test, a cone penetration test (CPT), and a pressuremeter test (PMT), have been carried out to obtain relevant experimental data and determine the pile end-bearing capacities (Joer et al. 1999; Foray et al. 1999). Simple models of cavity expansion were also

used to assess end-bearing capacities. Vesic (1973) has used this approach to derive an end-bearing capacity equation for piles based on confining pressure and soil compressibility. The applicability of his derived formula has been noted for both shallow footings (Poulos 1989) and piles (Yasufuku and Hyde 1995) residing in crushable soils, at least when compared to results yielded from employing Terzaghi's original equation (Terzaghi 1943). The outcome, however, does not explain why the bearing capacity varies with crushability and variations in the GSDs. Another formula, which relates the end-bearing capacity to the cavity expansion pressure, was developed by Yasufuku and Hyde (1995). Their proposed equation requires the introduction of a so-called secant friction angle in order to capture the observed pressure-dependence of the end-bearing capacity. The secant friction, however, is not a fundamental soil property and therefore cannot explain why the bearing capacity varies with crushability and GSDs. More recently, Russell and Khalili (2002) employed the cavity expansion approach to study the effect of grain crushing on CPT and PMT model tests, which required an assumed relationship between the grain crushing and the compressibility via the void ratio. However, this relationship was empirical and thus could not respond to variations in the tested material and its initial GSD.

The purpose of this chapter is to establish a more complete, rigorous and reliable bearing capacity equation of piles penetrating into sand taking into account the grain crushability as well as other critical factors (e.g. GSD, the friction coefficient, and elastic stiffness). To achieve this, the problem is analysed using the micromechanics-based continuum theory of breakage mechanics (Einav 2007a-d). As stated in Chapter III, this theory rigorously accounts for the effects of the evolving cumulative GSD due to grain crushing on the material behaviour. Micromechanical connections between an internal variable, breakage B, and the evolving GSD allows tracking continuously the GSD during the deformation. A linear elastic breakage model has been implemented into a FE code as outlined in the introduction to Chapter IV. This model will be used here to study pile penetration into crushable soils in the context of Finite Element Analysis. Comparing with experiments, it is shown that the FE model was able to predict pile end-bearing capacities, evolving GSDs, and soil deformations. On this basis, a parametric study was then carried out to establish the new formula for the piles' end-bearing capacity. The formula is robust and versatile and can capture the

effects of pressure, initial GSD, comminution limit defining yielding, friction coefficient, and the elastic stiffness of the material, on the prediction.

The structure of this chapter is as follows.

In the following Section 2, the results of cumulative GSDs obtained from theoretical prediction are compared with those from a model pile test. The good agreement highlights the model's ability to accurately capture the particle breakage around the driving pile.

Section 3 in this chapter presents the theoretical results of soil deformation and end-bearing capacities of a driving pile. These results are compared well to corresponding model pile tests, establishing a sound basis for the formulation of a new end-bearing capacity equation.

Section 4 in this chapter, through the parametric analysis, develops a new equation for predicting end-bearing capacity. The principal factors in such prediction are highlighted. Finally, the new equation's success in accurately predicting the pile end-bearing capacities in crushable soils is shown by comparing it with its experimental counterparts and many other existing formulae.

2 Analysis of cone-ended model pile test

Yang et al. (2010) carried out a pile test with cone tip in a quartz Fontainebleau sand, under an initial vertical stress of 150kPa. They measured the pile resistance and crushing profile surrounding the driven pile, which will be used to validate the numerical results in this study. The numerical simulaiton is conducted by employing the Arbitrary Lagrangeian Eulerian (ALE) method where appropriate remeshing and variable remapping technique are used for large deformation analysis (abaqus 2010).

The finite element model is depicted in Figure 5.1a. Following the procedure of the experiment, three steps are used in the currrent FE simulation. The first step is to gradually apply the gravity to the modelled sand until its elastic response becomes stable; second step is to apply the top pressure of 150kPa gradually to the surface of the model until its elastic reaction gets stable; the last step is to drive the pile into the modelled sand where the ALE technique is used to overcome the elements' large

distortion issue. Two input parameters are needed for the operation of the ALE calculation scheme in abaqus: remeshing frequency (i.e., how often a process of remeshing is being recurred) and sweeping frequency (i.e., time step duration of each remeshing). The remeshing and sweeping frequencies set for the current analysis are 10 and 1. Information regarding the ALE FE method can be found in the abaqus manual.

The modelled sand parameters are as follows: K=28.3MPa, G=13.1MPa and M=1.5 (based on effective friction angle of ϕ=36.5°). These parameters have been determined from a series of triaxial compression tests on Fontainebleau sand under the stress level of 100kPa (De Gennaro and Frank 2002). Other parameters are from Yang et al. (2010): critial comminution pressure p_c = 23MPa (from 1D compression test), and the soil-pile interface friction coefficient μ=tan(ϕ_p) was calculated using the measured interface friction angle ϕ_p=25°, (effective) unit weight of sand γ =16.3kN/m^3. In addition, based on the initial GSD in Yang et al. (2010) the grading index is taken as $\vartheta = 0.7$ (where the ultimate cumulative GSD was assumed to follow a fractal grading with a fractal dimension α=2.7). The agreement between the theory and the experiment is excellent when the plastic-breakage coupling angle ω is 55°.

The crushing profiles corresponding to different penetration depths are depicted in Figure 5.1b,c,d showing that the crushing influenced zone is approximately within half a pile radius from the shaft, in agreement with the experimenal observation (Yang et al. 2010). A closer look is given in Figure 5.2 where the numerically predicted breakage isolines are plotted in Figure 5.2b and the experimental ones in Figure 5.2a. The predicted cumulative GSD can be determined from the breakage using the initial and ultimate cumulative GSDs (3.2) and this is compared with the experimental measurements in Figures 5.3a-c. Figure 5.3d presents the theoretical prediction for the breakage variable B, which is plotted against the measured values calculated by the breakage definition (Einav 2007a). While the prediction of breakage in zone 1 appears excellent according to Figure 5.3d, inspection of the full cumulative GSD function in Figures 5.3a-c discloses some discrepencies since the cumulative GSD is a function of all the grain sizes and not only of a single internal variable B. Nevertheless, the usefullness of the fractional breakage hypothesis in Equation (3.2) should be highlighted, as the FEM model predicts favourably well the evolving GSD in all three

zones (Figures 5.3a-d). The numerically predicted end-bearing capacity of the model pile with penetration depth also compares well with its experimental counterpart (Figure 5.4).

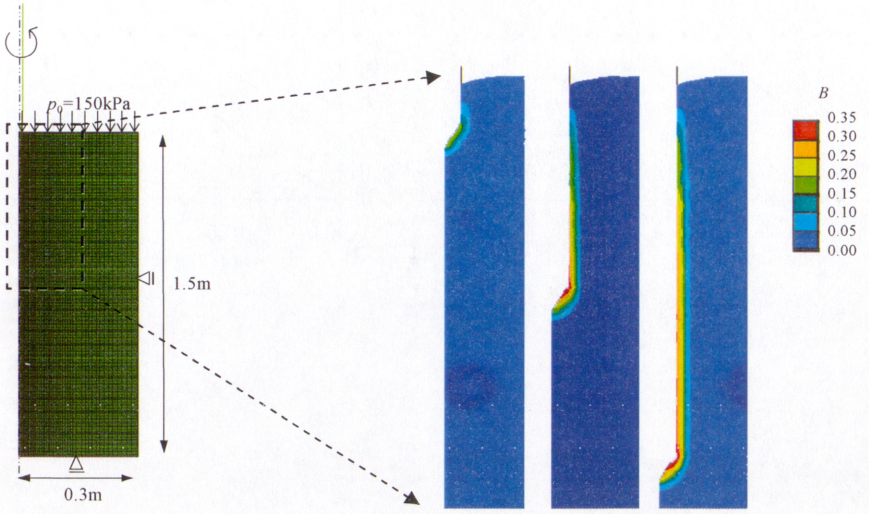

Figure 5.1 Simulation of model pile test in Fontainebleau sand: (a) finite element mesh and boundary conditions, (b-d) breakage distributions corresponding to penetration depths of S=5r, S=15r, and S=25r, respectively (S: penetration depth; r: pile radius)

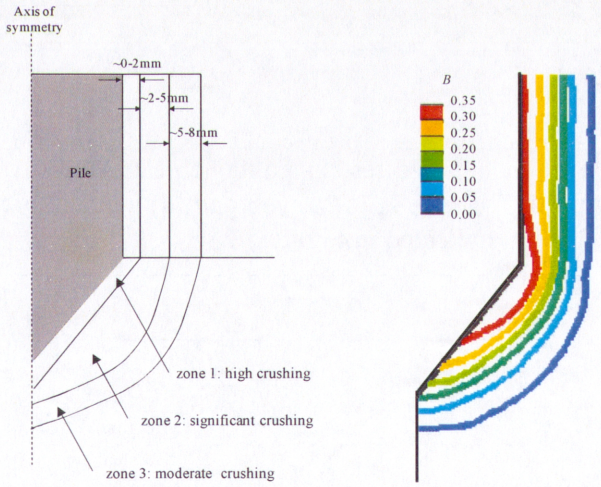

(a) experimental (reproduced from Yang et al. 2010) (b) numerical

Figure 5.2 Simulation of model pile test in Fontainebleau sand: profile of crushing zones

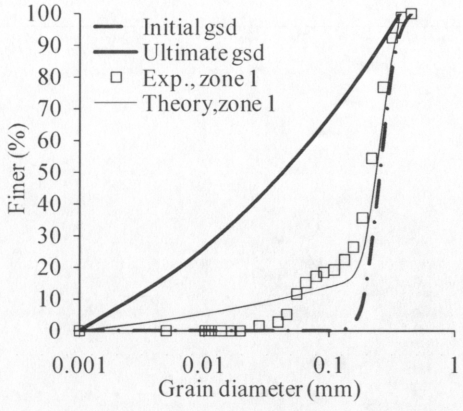

(a)

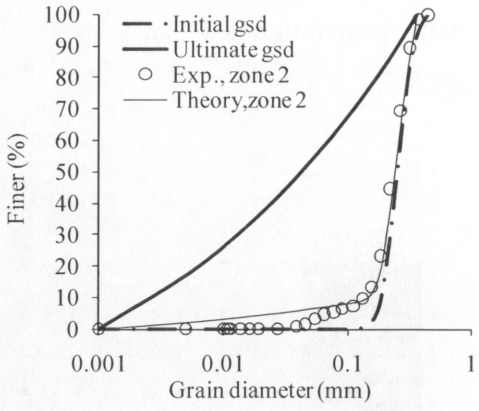

(b)

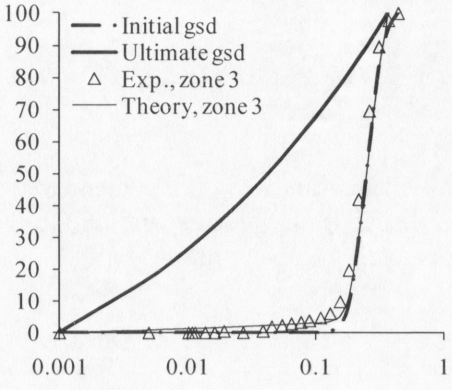

(c)

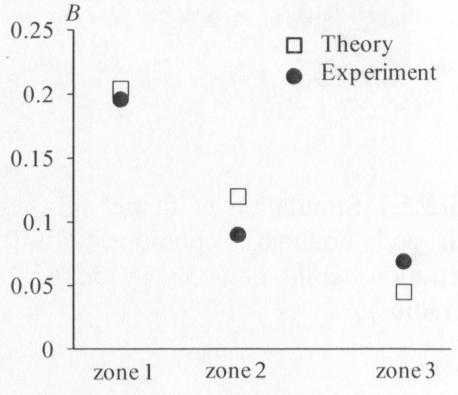

(d)

Figure 5.3 Simulation of model pile test in Fontainebleau sand: average grain size distributions for (a) zone 1, (b) zone 2, (c) zone 3 and (d) average breakage index for three zones (zones 1, 2 and 3 indicated in Figure 5.2a)

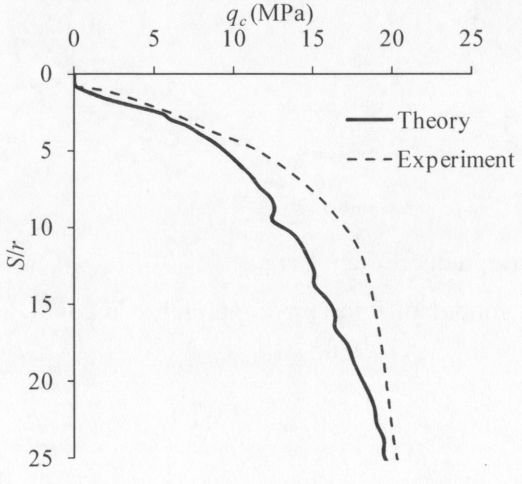

Figure 5.4 Simulation of model pile test in Fontainebleau sand: end-bearing capacity, q_c, versus normalised penetration depth, S/r

3 Analysis of pile penetration

In this section, the breakage constitutive model is used in an Eulerian finite element framework in abaqus (2010) to study the flat-ended pile penetrating into crushable sand, the Chiibishi sand (Kuwajima et al. 2009). In such an occasion, the elements around the pile tip would undergo extremely large deformation, beyond the accurate capacity of the ALE method. Instead, the Eulerian technique is able to overcome such extremely large distortion issues associated with ALE or Updated Lagrangian method for the pile with high cone angles such as 90° in flat tip piles (Sheng et al. 2005).

The following describes the mesh sensitivity analysis performed in Zhang et al. (2010). The model and boundaries are illustrated in Fig. 5.5, in which only a part of the rigid pile with a length L=4m is simulated. As indicated in the figure, lateral walls prevent horizontal movements; the pile's tip prevents vertical movement; the top and bottom walls maintain constant vertical stress σ_{v0} and enable the inflow and outflow of mass fluxes at a constant rate reflecting the pile's penetration velocity. Notice that the initial stresses are pre-established current analyses by applying designated external pressures. The results of the mesh sensitivity in terms of normalised tip resistance q_p by pile's tip area, A and p_c are presented in Figure 5.6, showing the convergence of the results upon mesh refinement.

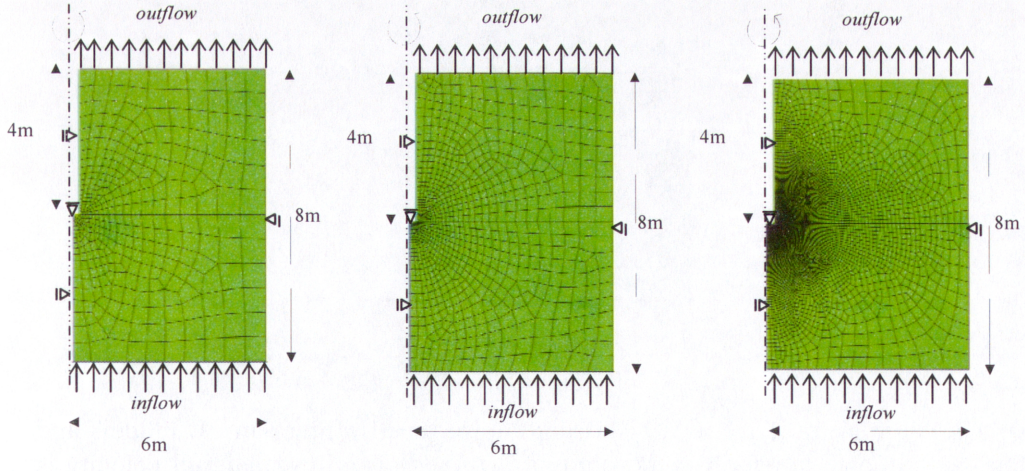

(a) L-1 (290 elements) (b) L-2 (892 elements) (c) L-3 (7700 elements)

Figure 5.5 Models for mesh sensitivity analysis (Zhang et al. 2010), in which 1) the rigid pile is fixed; 2) inflow material velocity is 0.02m/s; 3) initial vertical stress, σ_{v0}=100kPa and lateral stress, σ_{H0}=40kPa. Parameters are used: K=7586kPa, G=7112kPa, M=1, ϑ=0.7, and E_c=184kPa; unit weight of sand γ=20kN/m^3, pile diameter D=0.2m, and interface friction coefficient μ=0.3.

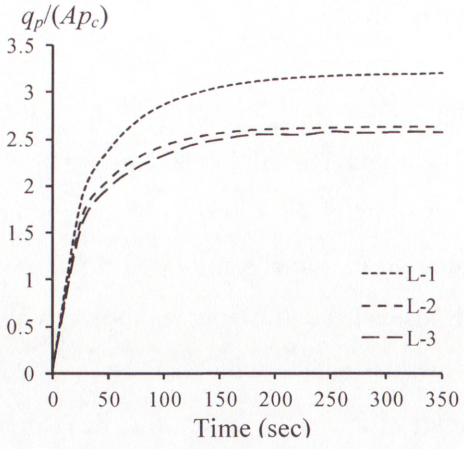

Figure 5.6 Mesh sensitivity results regarding to normalised tip resistance (Zhang et al. 2010).

Based on the previous sensitivity analysis we set the mesh as in Figure 5.7 for Chiibishi soil parameters (i.e. using 3600 4-node, reduced-integration, axisymmetric, solid elements). The parameters of the Chiibishi sand have already been provided in Table 4.2 (Chpater IV); correspondingly, the shear stress at the interface is calculated using the Coulomb friction model with friction coefficient $\mu=\tan(\phi/2)=0.4$ (Durgunoglu and Mitchell 1975). Other parameters relevant to the rigid pile and boundary conditions are defined same as those in Figure 5.5.

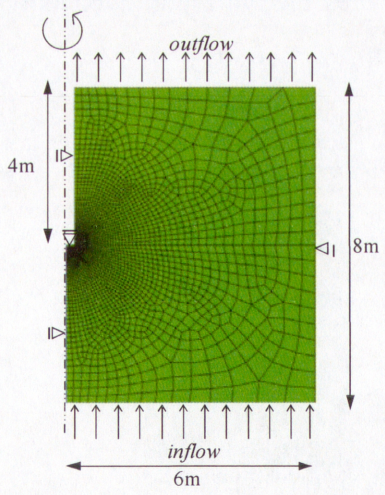

Figure 5.7 Pile penetration in Chiibishi sand: axisymmetric Eulerian FE models and boundary conditions, in which 1) the rigid pile is fixed; 2) inflow material velocity is 0.01m/s; 3) initial vertical and horizontal stresses are defined by nominating σ_{v0} and σ_{h0}

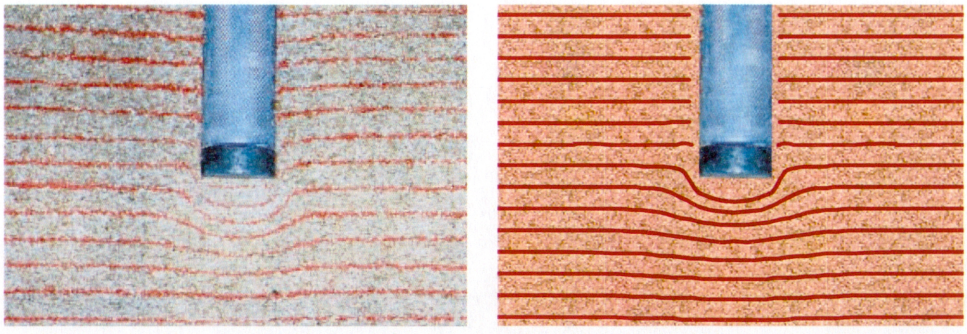

(a) S/D=0.5, experiment (b) S/D=0.5, theory

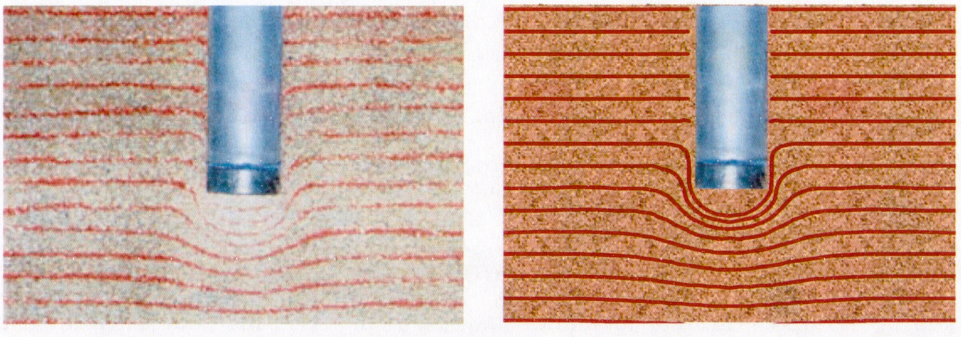

(c) S/D=1, experiment (d) S/D=1, theory

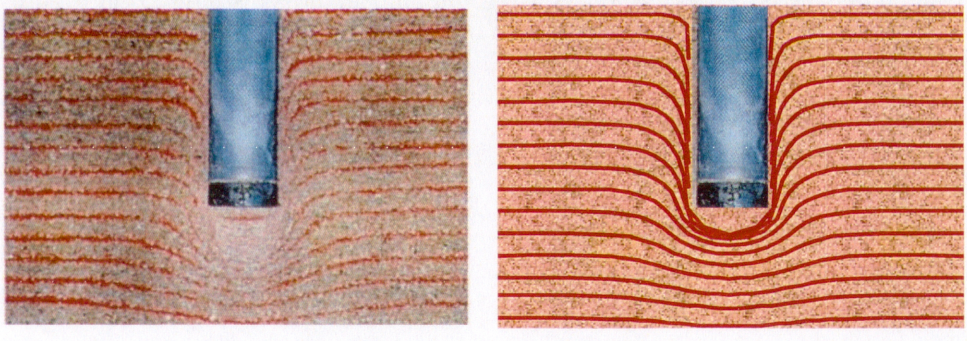

(e) S/D=3, experiment (f) S/D=3, theory

Figure 5.8 Pile penetration in Chiibishi sand: experimental observation (Kuwajima et al. 2009) and numerical prediction of soil deformation (S is penetration depth and D pile diameter; red lines in left Figures indicate coloured sand during experiments, with the corresponding prediction on the right).

Next, the experimental observations of the deformation patterns in the Chiibishi sand are given by Figures 5.8a,c,e, which will be predicted numerically using the FE model. This is achieved by employing a technique similar to the strain path method, which was originally proposed by Baligh (1985) in terms of inviscid fluid streamlines and then by Einav and Randolph (2005) using the upper bound theory of plasticity. Here,

this technique is adapted to employ the velocity profiles obtained by the FE numerical model, from the nodal velocities at steady state corresponding to the fixed Eulerian FEM mesh. Accordingly, when breakage and stress distributions tend to be stable, the velocity field at any point in the problem domain was calculated by employing shape functions interpolating the nodal velocities. Consequently, the positions and trajectories of the material points were tracked continuously from the moment they entered into the computational domain until they left it. This procedure then provides us with the numerical pictures of the soil deformation during steady state penetration. As can be seen in Figure 5.8, excellent agreement between the numerical (Figures 5.8b,d,f) and experimental (Figures 5.8a,c,e) deformation patterns is found.

In addition, the numerical model could be furthered assessed in the more traditional way, by comparing the numerical and experimental tip resistances as the piles penetrate through the soil (Figure 5.9). The agreement between these curves is very good. The small noise shown by the numerical solution is linked directly to the remeshing cycles in the abaqus calculation, as part of the ALE method. A parametric analysis shows such noise is very sensitive to one of the model's parameter, the critical state coefficient, M. We find that for higher M, the noise is larger (via Figures 5.6 and 5.9). One possible way to remove such numerical disturbances in the future could be done by adopting different large deformation FE methods, such as the material point method (MPM) (Sulsky et al. 1994).

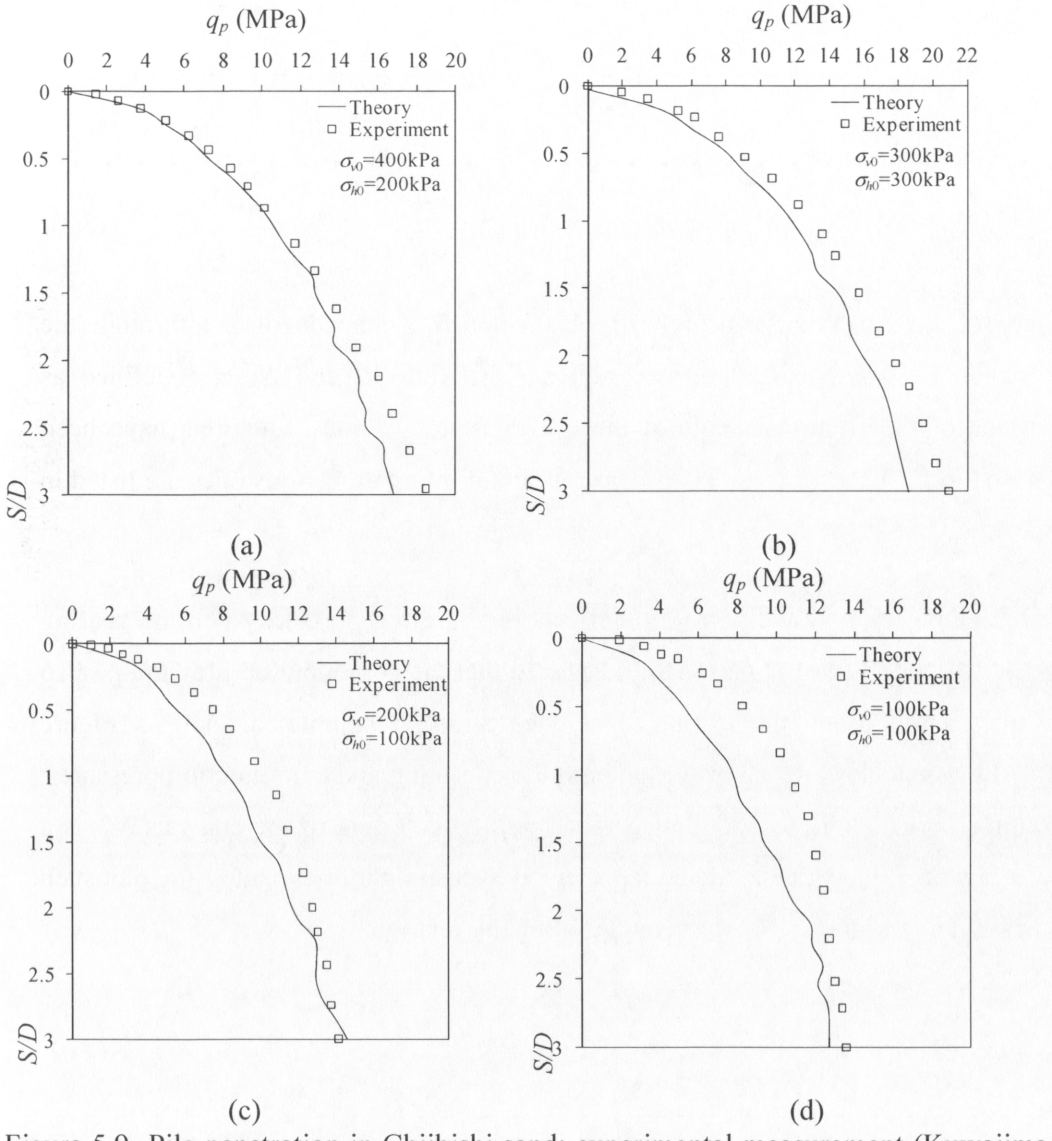

Figure 5.9 Pile penetration in Chiibishi sand: experimental measurement (Kuwajima et al. 2009) and numerical prediction of end-bearing capacity for different initial stress conditions (*S*: penetration depth; *D*: pile diameter).

4 A new formula for end-bearing capacity factor

One way to express the end-bearing capacity of piles is often written as:

$$q_p = N_q \sigma_{v0} \tag{5.1}$$

where σ_{v0} represents the initial vertical stress at a depth corresponding to the pile's tip and N_q is the dimensionless end-bearing capacity factor. More recently it became more common to express the end-bearing capacity of piles using the initial effective

confining pressure, p_0, rather than σ_{v0} (Al-Awquati and Vesic 1972; Al-Awquati 1975; Vesic 1973):

$$q_p = N_q^* p_0 \tag{5.2}$$

$$N_q^* = \frac{3}{1+2K_0} N_q \tag{5.3}$$

where the modified end-bearing capacity factor N_q^* depends on N_q through the coefficient of lateral earth pressure at rest, K_0. Both N_q and N_q^* are defined as functions of the frictional angle at the critical state. Various equations have been proposed in the past for these factors, and a few of the more famous ones are listed in Appendix A.

For crushable soils, in addition to the effects of confining pressure p_0 on the bearing capacity (Figure 5.9), it is reasonably expected that the comminution pressure p_c also play an essential role in the bearing capacity equation. The numerical analysis (Figure 5.10) shows the dependence of N_q^* on both the confining and comminution pressures, through a sort of 'over consolidation ratio' p_0/p_c. According to the analysis N_q^* is a power law of p_0/p_c, which could be represented by a straight line in a log-log plot such as that given in Figure 5.10b, to give the following relation:

$$N_q^* = \alpha \left(\frac{p_c}{p_0} \right)^{2\beta} = \alpha \left(\frac{2E_c K}{\vartheta p_0^{\,2}} \right)^{\beta} \tag{5.4}$$

where α and β are parameters which will be found later to depend on the material stiffness (G and K) and the friction parameter (M). The above equation provides the first formula to explain the sensitivity of measured bearing capacities on GSD through the grading index ϑ, *viz.* $q_p \propto \vartheta^{-\beta}$. Since ϑ weighs how far the initial GSD is from its ultimate counterpart, this new equation predicts an increasing bearing capacity with increasing polydispersity. For example, crushable sands that are initially poorly graded would resist less to the penetrating piles, which is supported by the experimental observations by McDowell and Bolton (2000).

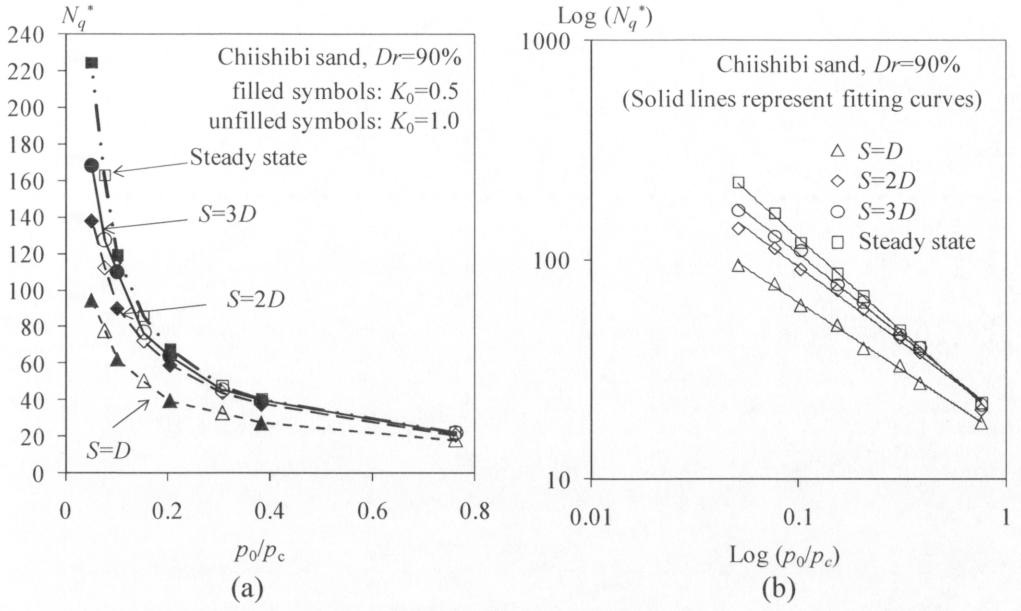

Figure 5.10 Modified bearing capacity factor N_q^* versus p_0/p_c (S: penetration depth; D: pile diameter; model parameters are listed in Table 4.2, Chapter IV)

Since the power law relation in (5.4) is controlled by two parameters α and β, it is necessary to quantify their dependence on the fundamental model constants: shear modulus, G; bulk modulus, K; friction coefficient at critical states, M and the coupling angle, ω. Numerical results on the variation of α and β with respect to penetration depth (Table 5.1) shows that β apparently increases with the penetration depth till steady state while the change in α is not monotonic. A comparison has been made by converting the experimental data from Kuwajima et al. (2009) into the definition of N_q^*. It is found that their experimental α ranges from 17.96 to 33.66, and β from 0.28 to 0.35 up to 3D penetration.

Table 5.1 Effects of penetration depth on α and β

Penetration	α	β	R^2
S=D	15.06	0.31	0.9975
S=2D	18.25	0.35	0.9922
S=3D	18.10	0.38	0.9960
Steady	17.41	0.42	0.9995

The results in Table 5.1 indicate that β reaches a constant value of 0.42 at steady state. This constant value can be confirmed by a parametric study employing different values of G/K, M and ω. The numerical results are depicted in Figure 5.11 and the corresponding values of α and β listed in Table 5.2.

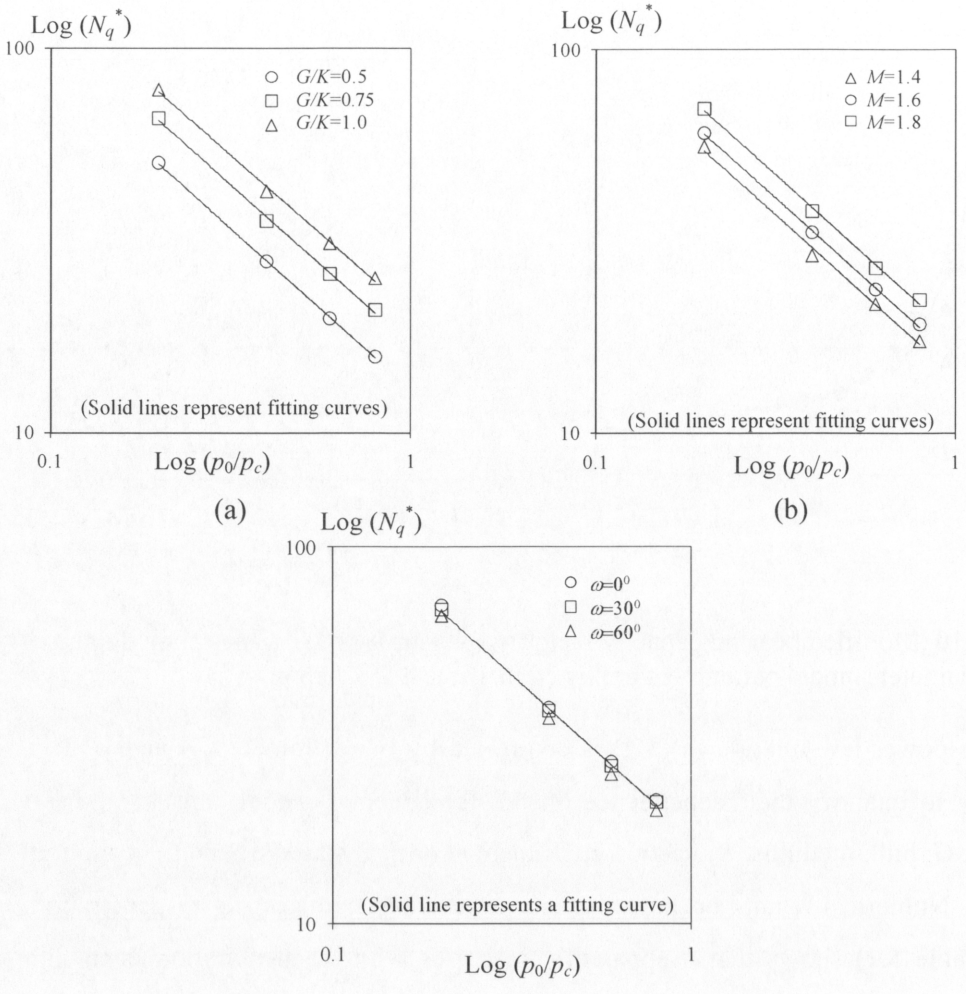

Figure 5.11 Modified bearing capacity factor N_q^* versus p_0/p_c at steady state penetration with K_0=1: (a) effects of G/K; (b) effects of M; (c) effects of ω (other model parameters, if not varied, are listed in Table 4.1 in Chapter IV)

Table 5.2 Effects of G/K, M, and ω on α and β at steady state penetration

Parameter	Value	α	β	R^2
G/K	0.5	12.98	0.42	0.999
	0.75	16.98	0.42	0.998
	1.0	20.55	0.42	0.998
M	1.4	14.12	0.42	0.996
	1.6	15.68	0.42	0.999
	1.8	17.99	0.42	0.998
ω	0^0	17.18	0.42	0.999
	30^0			
	60^0			

Table 5.3 Effects of G/K and M on α (for β=0.42)

	M=1.4	M=1.6	M=1.8
G/K=0.5	10.10	10.97	12.65
G/K=0.75	13.47	14.57	16.24
G/K=1.0	16.03	17.45	20.04

It can be seen that β=0.42 is independent on the other parameters. In contrast, α grows with increasing G/K and M. Also, both α and β are independent on the coupling angle, ω, and therefore the end-bearing capacity is also independent on ω. Therefore, α can be expressed as a function of M and G/K only, the relationship of which is obtained from another series of simulations using different values for G/K and M. The obtained results, listed in Table 5.3, give us the following relationship (with deviation errors always less than 4.5%):

$$\alpha = M^3 + 14(G/K) \tag{5.5}$$

Expressing G/K in terms of the Poisson's ratio ν, the complete expression for N_q^* can given as:

$$N_q^* = \left(M^3 + 7\left(\frac{3-6\nu}{1+\nu}\right)\right)\left(\frac{p_c}{p_0}\right)^{0.84} \tag{5.6}$$

Using the standard approximation $M = 6\sin\phi/(3-\sin\phi)$, the bearing capacity equation can also be expressed as:

$$N_q^* = \left(\left(\frac{6\sin\phi}{3-\sin\phi}\right)^3 + 7\left(\frac{3-6\nu}{1+\nu}\right)\right)\left(\frac{p_c}{p_0}\right)^{0.84} \tag{5.7}$$

where it is recalled that according to the breakage model the comminution pressure p_c, which marks isotropic yielding, depends on the GSD via ϑ, i.e. $p_c = \sqrt{2KE_c/\vartheta}$ (Einav 2007c). Therefore, the last equation for the end-bearing capacity of piles penetrating into sand is here dependent on the confining pressure p_0, GSD (via ϑ), critical breakage energy E_c, elastic Young's modulus (E) and Poisson's ratio (ν), and the friction coefficient M. The performance of this new formula is compared for the two typical crushable soils with four previous ones by Prandtl (1921), Terzaghi (1943) and Vesic (1973, 1975), as depicted in Figure 5.12. Both the Prandtl and the Terzaghi

solutions are pressure independent, unlike the experimental results showing high-pressure sensitivity. It appears that out of the previous formulae, the two equations by Vesic are the most successful in reproducing the pressure sensitivity, but either over or under estimate the true result. On the other hand, the new formula appears highly successful both qualitatively and quantitatively. Notice, that unlike the previous formulae, the new one depends on the critical comminution pressure p_c (a value which was therefore employed identically to non-dimensional the pressure in all the solutions). This critical comminution pressure depends on the GSD, which for the first truly underpins the compressibility of crushable soils.

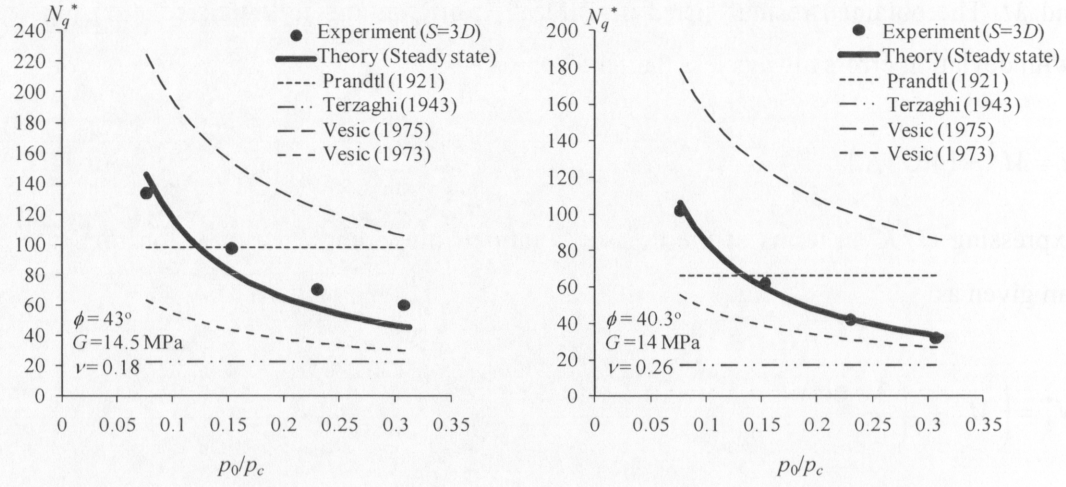

Figure 5.12 Modified end-bearing capacity factor N_q^* versus p_0/p_c for (a) Chiibishi sand; and (b) Dog's bay sand (experimental data from Kuwajima et al. 2009).

The influence of the initial GSDs on N_q^* is further explored as seen in Figure 5.13 based on the parameters of Dog's bay sand (see Table 4.2, Chapter IV). Note that the initial GSDs indicated in the insert plot in Figure 5.13 are calculated by assuming the initial size distribution also power law, with a coefficient β replacing α in equation 3.5. It is evident that the more polydispersed the initial GSD is, the end-bearing capacity increases. This conclusion seems intuitively reasonable and should motivate future experimental research to validate, or adjust the theoretical expectation in Figure 5.13.

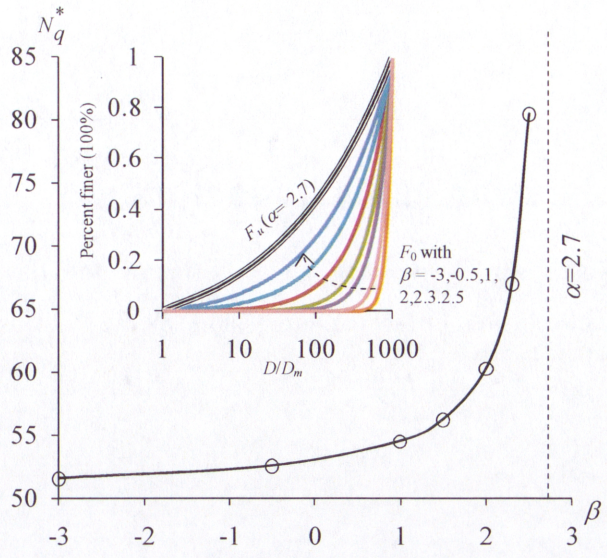

Figure 5.13 Influence of initial GSDs on N_q^* for Dog's bay sand described by the shape parameter β (Inset shows the corresponding GSD, always with an ultimate GSD defined by α=2.7, and a minimum grainsize always being D_m)

5 Summary

The end-bearing capacity of piles penetrating into crushable soils is analysed within the context of the breakage mechanics theory. The importance of resorting to fundamental failure mechanisms of crushable soils in determining the end-bearing capacity is highlighted. The breakage mechanics theory does not only improve the understanding of the constitutive response of crushable soils but also provides us with an insight into such problems as the bearing capacity and consequently results in predictions that are free from empirical parameters. This is particularly essential for practical purposes, given the reliability issues in interpreting and incorporating data from both lab and field tests in the prediction of the bearing capacity. The proposed end-bearing capacity equation captures the effects of the material crushability, in terms of the initial GSD, the confining pressure, the critical breakage energy, and the constants of elasticity. The result appears to provide a more reliable prediction of capacities compared to any of the previous equations. The new bearing capacity equation can benefit the future design of pile foundations in sand materials, and can be used as a reference for engineering purposes.

Appendix V-1

Previous end-bearing capacity factors

Prandtl (1921) proposed an end-bearing capacity factor for flat strip surfaces punching through idealised weightless incompressible media with assumed general shear failure:

$$N_q = \tan^2\left(\frac{\pi}{4}+\frac{\phi}{2}\right)e^{\pi\tan\phi} \tag{A1}$$

The assumption of a general shear failure, however, is known to be problematic for compressible soils. In such cases, the shear failure tends to be more local.

Terzaghi (1943) suggested modifying the equation above by incorporating the reduced friction angle $\phi_r = \tan^{-1}\left(\frac{2}{3}\tan\phi\right)$ to account for the local shear in compressible soils:

$$N_q = \tan^2\left(\frac{\pi}{4}+\frac{\phi_r}{2}\right)e^{\pi\tan\phi_r} \tag{A2}$$

Both (A1) and (A2) could be corrected in the usual way to allow applying these factors to the circular flat surface shape of typical piles. However, irrespective to the shape of the base, the assumption embedded do not reflect the strengthening of the soil with penetration depth. Moreover, (A2) is known to give too conservative answers for piles (Vesic 1973).

Vesic (1973) first attempted to modify Prandtl's equation (A1), by considering the soil compressibility. For that reason Vesic introduced the reduction compressibility factor ξ_{qc} (here specificied for the case of flat circular surface):

$$N_{qc} = N_q\xi_{qc} \tag{A3}$$

$$\xi_{qc} = \exp\left[(3.07\sin\phi)\frac{\log(2I_r)}{1+\sin\phi} - 3.8\tan\phi\right] \tag{A4}$$

where for sand the rigidity index $I_r = G/(\sigma_{v0}\tan\phi)$ was introduced to capture the influence of the initial (effective) vertical stress σ_{v0}.

Vesic (1975) proposed another equation, an alternative to his own (A3, 4), specified in terms of N_q^*:

$$N_q^* = N_{qc}\xi_{qc} \tag{A5}$$

$$N_{qc} = \tan^2\left(\frac{\pi}{4}+\frac{\phi}{2}\right)e^{\left(\frac{\pi}{2}-\phi\right)\tan\phi} \tag{A6}$$

$$\xi_{qc} = \frac{3}{3-\sin\phi}(I_{rr})^{\frac{4\sin\phi}{3(1+\sin\phi)}} \tag{A7}$$

The main conceptual change may be seen through the modified rigidity index $I_{rr} = I_r/(1+\bar{\varepsilon}_v I_r)$, which adds irreversible compressibility effects via $\bar{\varepsilon}_v$, the average volumetric strain in the plastic zone. Unfortunatly, volumetric strain is a reference dependent measure that requires a lot of guess work. More critically, it was recommended to take $\bar{\varepsilon}_v = 0$ for soils that are initially at their densest state (e.g., corresponding to the experiments evaluated in the current paper). Unfortunatly, the notion of densest state in crushable soils is ambiguous. This is because that in such soils the maximum and minimum densities depend on the GSD, which by itself varies during the deformation.

The above four formulae are plotted in Figure 5.12 against ours (5.7) for both the Chiibishi and Dog's bay sands. Note that the experimental condition provides K_0=1, and therefore the N_q is the same as N_q^*. Since Vesic's formulae (A3-A7) include σ_{v0} through the use of I_r, the corresponding curves are indeed pressure-dependent. In the proposed equation, both the compressibility of the soil and the initial GSD are shown through the comminution pressure, p_c. The initial GSD in the current experiments was fixed. Future experiments are recommended to explore the effect of the initial GSD on the end-bearing capacity, in a way that could be evaluated using the current formula (5.7).

Chapter VI

Hydro-mechanical response of expanding cavities in crushable granular soils

1 Introduction

The study of perforations in crushable granular materials presents a challenge: how to predict the cavity expansion induced damage zone and its characteristics, both of which are essential in the study of sand-, gas- and oil-production, deep foundations, tunnels and underground excavations. This is complicated and requires the correct prediction of permeability reduction due to grain crushing and correspondingly excess pore pressures around the expanding cavity. For example, the excess pore pressure, instantly after the expansion, would introduce an erosion process involving the removal of fine particles and formation of localized annular clogging with the migratory of bigger particles (Valdes and Santamarina 2007). If sufficient clogging occurs, the production of the sand might cease but catastrophic unplugging via hydraulic fracture might follow. A similar situation may occur in gas- and oil-extraction from the drilling into crushable granular materials. Another adverse impact is the soil liquefaction when sufficient excess pore pressure appears, which is the main cause of many failures of foundations and slopes (Sassa et al. 1996; Wang and Sassa 2000). Therefore, the study of crushing damage zones, and the prediction of the development of the excess pore pressures, is of great importance to many production industries.

Grain crushing and the resulting evolving GSD lead to the increase of specific surface and/or the porosity reduction of the granular ensemble. Particularly in undrained conditions, where there is no porosity reduction, the specific surface of the sample still increases as the GSD evolves. Consequently, the local permeability reduces, generating high excess pore pressure that dissipates slowly (Okada et al. 2004). Many

experiments (though not directly relevant to cavity expansion) have already shown the significant impact of grain crushing on permeability reduction and excess pore pressure generation (e.g., Zhu and Wong 1997; Okada et al. 2004). It is therefore essential to be able to predict the permeability and excess pore pressure given the evolving GSD as the characteristics of the grain crushing process.

Hazen's (1892) formula links the permeability, k to D_{10}^2 (D_{10} is a grain size for which 10% of the grains are finer by mass). This statement was later slightly modified to link to D_{10}^n (n=1.65-1.85) based on statistical power regression analyses of 19 sets of published data (Shepherd 1989). In addition, many other formulae have been suggested. For instance, Sperry and Peirce (1995) developed a linear model to estimate permeability based on a grain size of D_{50} (grain size for which 50% of the grains by mass are finer). Alyamani and Şen (1993) used both D_{10} and D_{50} (grain sizes for which 50% of the grains by mass are finer) in their equation. Finally, a highly effective and popular form is to adopt the Kozeny-Carman equation (Matyka et al. 2008).

Although the connection between the grain sizes and permeability has been widely proposed, the correlation between the grain sizes and the hydro-mechanical behaviour of the granular assembles has yet to be satisfactorily addressed. An example was proposed by Papamichos et al. (1993) who analysed the inter-granular stresses for estimating the local permeability reduction, which is dependent on a single size of D_{50}. Another attempt is to account for grain crushing in the interpretation of the cone penetration test (CPT) or pressuremeter test by Russell and Khalili (2002). Their numerical findings highlighted how the limit stress at the cavity wall is significantly affected by grain crushing. A more recent work has been presented by Einav et al. (2011). They established a general grain-crushing analysis using breakage mechanics with a cavity expansion solution. Their work shows the advantage in being able to track the evolving GSD for the solution of stresses and permeability reduction. In particular, instead of relying on a single size, Einav et al. used a mean harmonic grain size, D_H calculated from the entire evolving GSD to predict the permeability reduction. The use of D_H, rather than a single size, has been proved to be more reliable in accurately predicting the permeability reduction (Carrier 2003; Matyka et al. 2008).

The continuum approach by Einav et al. (2011) established the theoretical basis for the connection between the evolving GSD and permeability reduction in the context of undrained cavity expansion. This work will be reviewed and further extended in this chapter for the study of hydro-mechanical behaviour in cavity expansion problems. A special focus is on the generation and dissipation of the excess pore pressures. The following section starts with a brief review of a constitutive model based on breakage mechanics. The Kozeny-Carman's equation will then be briefly presented, followed by the Finite Element model of the cylindrical cavity expansion. The analysis of the excess pore pressure and other effective stresses of brittle granular materials will be presented and practical formulae to predict the excess pore pressure finally derived.

The philosophy we choose to adopt to address this issue is to use the simplest possible model to conceptually identify the main effects, without bringing too much complexity at once. Therefore, we currently use the simplest breakage model based on linear elasticity. The point being that the complexity of the boundary conditions will already provide untrivial results, even with this simple linear elastic breakage model. In the future, a more complicated model based on nonlinear elasticity will be implemented into the FE code to improve the model realism. In addition, the current analysis is unable to analyse erosion issues and assumes the particles during drainage do not erode.

2 Permeability reduction using breakage mechanics

Grain crushing would reduce permeability, k, due to increase of particle surface area, S. The surface area can be represented in terms of the harmonic mean grain size D_H: $S=6/D_H$, for spherical grains. Using the modified Kozeny-Carman equation (Matyka et al. 2008), the permeability k is expressed as in Equation (6.1). Note that Kozeny-Carman equation has several limitations. For example, the equation is based on the assumption of laminar flow and low pore fluid velocity, and thus for turbulent flow conditions it can become inadequate (Francisco et al. 2009). In addition, the influence of soil structures on the permeability, including that from the void fabric and particle shape (Sahashi et al. 2005), is also beyond the scope of this equation. Nevertheless, the Kozeny-Carman equation has been well supported by experiments, where it was

argued to be particularly suitable for random packing of spheres (Klemm et al. 2001) and fractal porous media (Stanley and Andrade Jr 2001; Adler 1988). Accordingly, there are good reasons to adopt this equation for analysing our current problem.

$$k(r)=\frac{1}{c_1}\frac{n^3}{(1-n)^2}D_H(r)^2 \tag{6.1}$$

where r is the radial distance to the cylindrical centre; c_1 is the Kozeny-Carman constant (Matyka et al. 2008); n is current porosity, which is calculated using $n = e/(1+e)$; and the void ratio, e, is updated using $de \approx -d\varepsilon_v^p(1+e)$. The harmonic mean grain size, D_H, as a function of GSD (the GSD is the derivative with respect to fractional size x of its cumulative function $F(x, B)$) is defined by:

$$D_H(r)^{-1}=\int_{D_m}^{D_M} g(x,B)\frac{dx}{x}=(1-B(r))D_{H0}{}^{-1}+B(r)D_{Hu}{}^{-1} \tag{6.2}$$

in which D_M and D_m are the maximum and minimum grain sizes respectively; D_{H0} and D_{Hu} are the initial and ultimate harmonic mean grain sizes, which correspond to $g_0(x)$ and $g_u(x)$ and can be practically assumed to be power functions in the absence of experimental data (Buscarnera and Einav 2012):

$$g_0(x)=(3-\beta)\frac{x^{2-\beta}}{D_M{}^{3-\beta}-D_m{}^{3-\beta}} \tag{6.3}$$

$$g_u(x)=(3-\alpha)\frac{x^{2-\alpha}}{D_M{}^{3-\alpha}-D_m{}^{3-\alpha}} \tag{6.4}$$

Thus,

$$D_{H0}=\left(\int_{D_m}^{D_M} g_0(x)\frac{dx}{x}\right)^{-1}=\left(\frac{2-\beta}{3-\beta}\right)\left(\frac{D_M{}^{3-\beta}-D_m{}^{3-\beta}}{D_M{}^{2-\beta}-D_m{}^{2-\beta}}\right) \tag{6.5}$$

$$D_{Hu}=\left(\int_{D_m}^{D_M} g_u(x)\frac{dx}{x}\right)^{-1}=\frac{(2-\alpha)}{(3-\alpha)}\left(\frac{D_M{}^{3-\alpha}-D_m{}^{3-\alpha}}{D_M{}^{2-\alpha}-D_m{}^{2-\alpha}}\right) \tag{6.6}$$

where α and β are fractal coefficients. The model's ability to capture the trends in porosity and permeability changes was already presented in Nguyen and Einav (2009), which highlighted the role of material non-linear elasticity (known to be pressure dependent) on well capturing the irreversible response of the permeability reduction, in a way intrinsically related to grain crushing. Nevertheless, the isotropic linear elasticity law currently employed is widely-used in soil mechanics practice, and its implementation should therefore be more approachable for practitioners. The use of the more predictive non-linear elastic law is left for future work.

3 Finite Element model for cylindrical cavity expansion

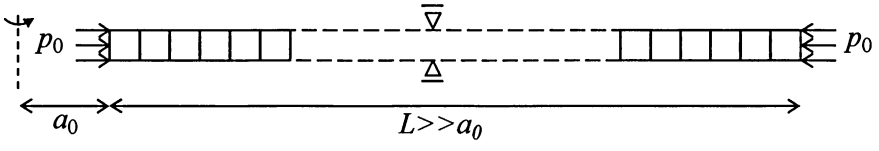

Figure 6.1 Initial FE model

The disturbance of confined brittle granular material is often modelled as a cylindrical cavity expansion problem in plain strain conditions. Here, 4-node axisymmetric quadrilateral, bilinear displacement, bilinear pore pressure elements were used. This is illustrated in Figure 6.1, in which: 1) the brittle medium is considered to be saturated and the pore fluid flow behaviour is governed by Darcy's law; 2) the domain is under various initial isotropic pressures of p_0 with initial void ratio of n_0=1.5 and a typical Australian sand's permeability of k_0=0.002m/s (Alyamani and Şen 1993); 3) only the right boundary is defined as being pervious through the analysis, i.e. the inner cavity interface, top and bottom boundaries were impermeable; and 4) undrained (stage I) procedures under each confining pressure are simulated with the expansion from a_0 (here 0.3m) to any necessary distance, a (here a=2.5a_0 is found to be adequate). To ensure the porosity remains unchanged during the expansion, the time incremental size and time period in step 2 are, respectively, 10^{-9}s and 10^{-6}s (during the calculation it was checked that the volumetric strain is near zero). The maximum pore pressure is found at the cavity wall, and it approaches an asymptotic u_{max} as the expansion proceeds. When u_{max} appears, the cavity size is maintained and the water pressure is allowed to dissipate/drain (stage II) in the radial direction only. The model parameters are listed in Table 6.1. Note that these elastic moduli are broadly similar in magnitude to those previously measured for calcareous soils (see Zhang et al 2012). Such a

choice is only for the basis of the parametric study (sections 5.2 and 6.2). It will be shown later that the G/K ratio (i.e., a ratio defining the Poisson's ratio) and ϕ are fundamental parameters for the analysis.

Table 6.1 The model's relevant parameters

Bulk modulus K(kPa)	Shear modulus G(kPa)	Friction coefficient angle ϕ	Critical breakage energy E_c(kPa)	Grading index ϑ
30000	10000	25°	50	0.4

An anyltical solution from Einav et al. (2011) enables us to calculate the breakage distribution and mechanical response of effective stresses and strains during undrained expansion. For example, the analytical solution in the case of a 50% expansion of the initial cavity radius, i.e., a=1.5a_0 has proved to be identical to our Finite Element results with the parameters listed in Table 6.1. Analytical solution is used as a benchmark to initially verify our Finite Element model (Figure 6.2a–d).

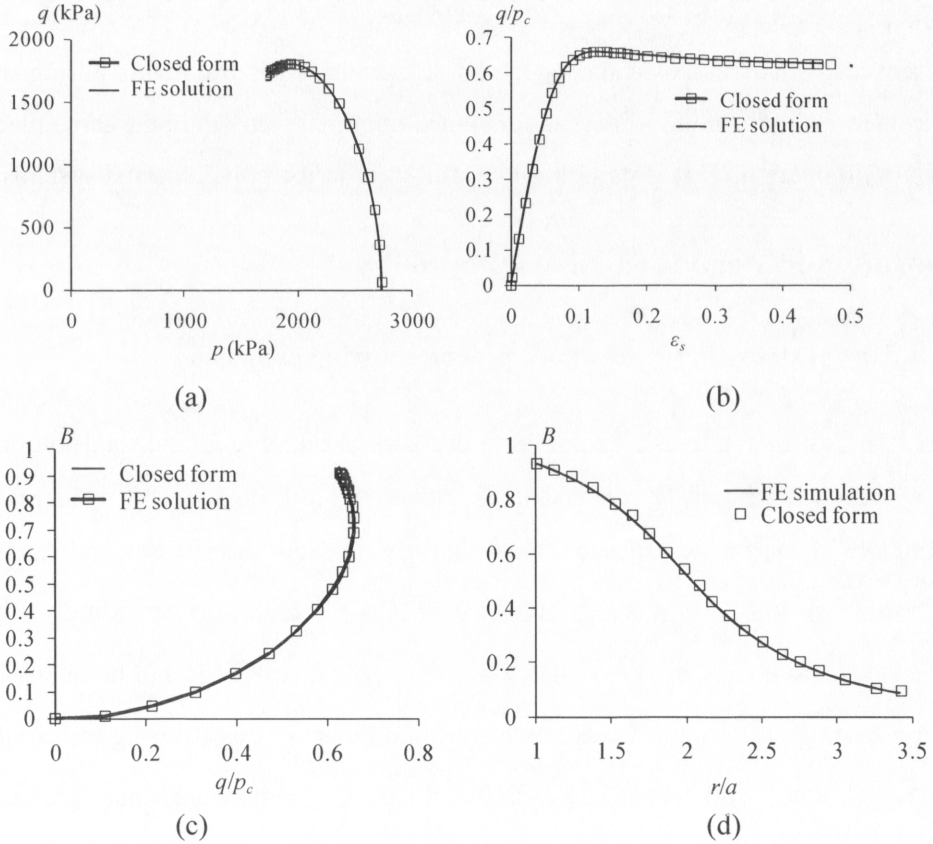

Figure 6.2 Mechanical responses of the brittle granular material in undrained expansion. The initial all-around pressure was set equal to the critical pressure, p_0=p_c, showing the critical status for breakage under isotropic compression condition.

The explicit link between the internal variable B and the evolving GSD (equation 3.2) allows the continuous tracking of the evolving GSD during the deformation process. Such a theoretical prediction of evolving GSD has already been compared favourably to experimental observations in various crushable sands (e.g., Einav 2007b; Zhang et al. 2012). This is a novel feature of any constitutive models derived from breakage mechanics theory, which distinguishes itself from other constitutive models for soils in the literature. In undrained loading case the grain crushing is the main contributor to the permeability reduction (see Nguyen and Einav 2009), which is associated to the generation/dissipation of excess pore pressure. On this basis, further study on the hydro-mechanical response of the model will be carried out in two stages: first in undrained cavity expansion in following Section 5 and then consolidation in Section 6. The main purpose is to explore the effects of material properties on the potential link between the grain crushing and the generation/dissipation of excess pore pressure under various conditions.

Our present analysis does not consider the erosive mobility of fragments during the drainage stage. At this point, our analysis assumes fragments remain in the same place during fluid dissipation. This is particularly useful to describe polydispersed systems.

4 Exploration in stage I: Cavity expansion

4.1 Variations of stress and excess pore pressure during expansion

The first issue of interest is the excess pore pressure variations, u, and total internal (radial) stress, σ_r, at the cavity interface. As shown in Figure 6.3, u and σ_r increase asymptotically as expansion proceeds. Note that in this paper the stresses and excess pore pressure are normalised by p_c (recall $p_c = \sqrt{2KE_c / \vartheta}$). Correspondingly, the variation of effective stresses (i.e. radial stress, σ'_r vertical stress, σ'_z and hoop stress, σ'_θ) and pore pressure u with the distance from the inner interface during the cavity expansion are plotted in Figure 6.4. A detailed illustration of the excess pore pressure is presented in Figure 6.5 in terms of various expansion ratios.

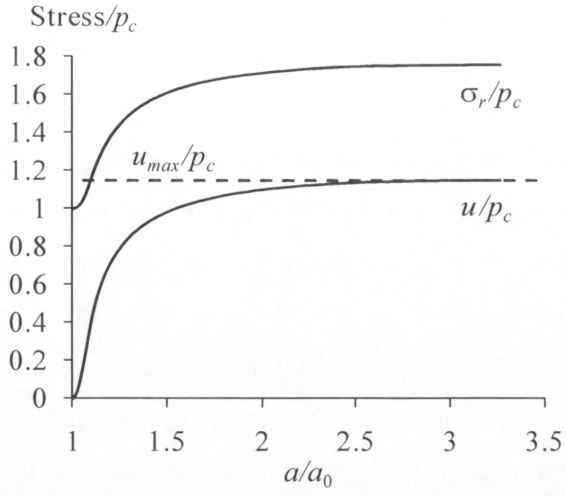

Figure 6.3 Variation of pore pressure and total radial stress at the cavity interface during undrained expansion

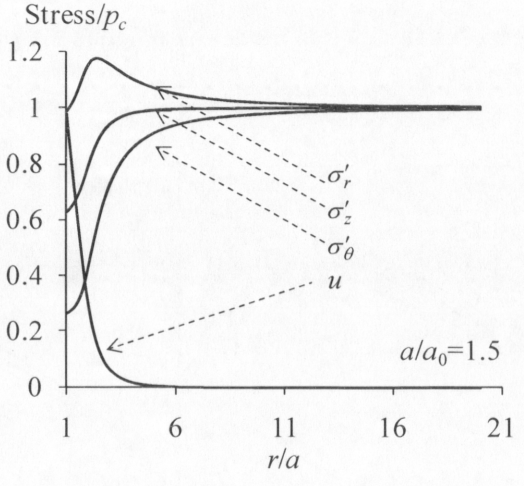

Figure 6.4 Stresses distribution in radial position at a=1.5a_0 under undrained condition

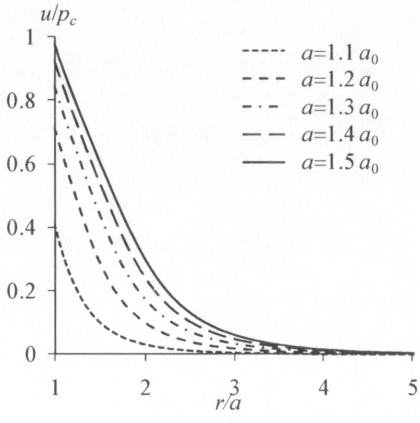

Figure 6.5 Generation of pore pressure against radial position during undrained expansion

4.2 Generation of maximum pore pressure at the cavity interface

We are interested in the excess pore pressure at the cavity interface because this is always the greatest compared to other locations (see Figure 6.5). We know that the increase in pore pressure reduces the effective pressure on the soil skeleton and hence the soil strength. A critical situation corresponds to the maximum value, u_{max}, of such water pressure, as the cavity expands indefinitely (as shown in Figure 6.3). In this section, the correlation between the u_{max} and granular crushability will be examined. A series of numerical experiments were performed by varying, one parameter at a time while the rest is kept fixed (with values indicated in Table 6.1).

From the numerical experiments, the pore pressure at the cavity interface was found to increase with the expansion till the maximum value, u_{max} is reached (see Figure 6.3). Variation of u_{max} with respect to change in model parameters are plotted in Figure 6.6.

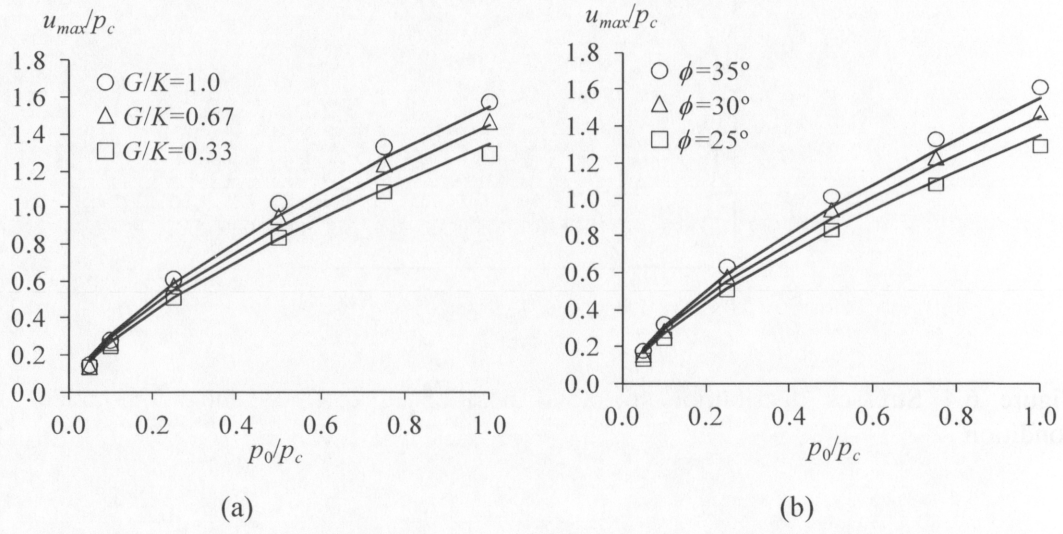

Figure 6.6 Generation of maximum pore pressure at cavity interface during undrained expansion under different isotropic confining pressures. (a) effects of G/K; (b) effects of ϕ (other model parameters, if not varied, are listed in Table 6.1; The solid lines are fitting curves for each simulation)

With the data in Figure 6.6, a power law function can be used to obtain good agreement with numerical experiments:

$$\frac{u_{max}}{p_c} = \alpha\left(\frac{p_0}{p_c}\right)^{\beta} = \left(0.5M + 0.3\frac{G}{K} + 0.75\right)\left(\frac{p_0}{p_c}\right)^{0.7} \tag{6.7}$$

The relevant coefficients α and β in above (6.7) are listed in Table 6.2.

Table 6.2 Parameters for equation (6.7)

Parameter	Value	α	β	R^2
	0.33	1.35	0.7	0.987
G/K	0.67	1.45	0.7	0.991
	1.0	1.55	0.7	0.988
	25°	1.35	0.7	0.987
ϕ	30°	1.45	0.7	0.997
	35°	1.55	0.7	0.996

Alternatively, using the standard approximation $M = 6\sin\phi/(3-\sin\phi)$, and from elasticity, $\nu = (3K\text{-}2G)/(6K+2G)$. (6.7) can be written as:

$$\frac{u_{max}}{p_c} = \alpha\left(\frac{p_0}{p_c}\right)^{\beta} = \left(\frac{3\sin\phi}{3-\sin\phi} + 0.45\left(\frac{1-2\nu}{1+\nu}\right) + 0.75\right)\left(\frac{p_0}{p_c}\right)^{0.7} \tag{6.8}$$

In this breakage model, the comminution pressure p_c, which marks the onset of isotropic yielding, depends on the GSD via ϑ, i.e. $p_c = \sqrt{2KE_c/\vartheta}$ (Einav 2007c). Substitute this relation into (6.7) or (6.8), the connection between u_{max} and GSD is therefore established through the grading index ϑ, i.e. $u_{max} \propto \vartheta^{-0.15}$. This indicates that for finer gradation of the initial granular assembly (corresponding to smaller ϑ), the value of u_{max} becomes higher. This seems reasonable and reflects the influence of tortuosity: for polydispersed granular systems, which have more variation in grain sizes, the path of the fluid is more tortuous. Therefore, fluid flow becomes more difficult and lack of dissipation causes higher pore pressures (e.g., Matyka et al. 2008).

5 Exploration in stage II: Consolidation

5.1 Variations of stress and excess pore pressure during dissipation

The variation of the excess pore pressure in consolidation is of engineering interest, as the results between pore pressure and time measured from piezocone testing (CPTU) can be used to estimate the in situ horizontal coefficient of consolidation and coefficient of permeability (e.g., Robertson et al. 1992; Burns and Mayne 1998;

Cortellazzo and Simonini 2001). Some theoretical models (or analytical solutions) have been used to interpret the pore pressure dissipation results, usually based on the cavity expansion theory (e.g., Torstensson 1977) and the strain-path method (e.g., Teh and Houlsby 1988). However, the above solutions strongly depend on an idealised initial pore-pressure distribution around the cone, which might not well reflect the real situation (Sully et al. 1998). In addition, most relevant studies in the literature focus on clay but very little on sand. Furthermore, there seem to have been no attempts so far to account for grain crushing in interpreting the results of pore pressure dissipation in sand.

The effect of grain crushing on pore pressure dissipation in crushable soils is studied in this section. For an illustration purpose, the initial and ultimate cumulative GSDs, F_0 and F_u, of the modelled granular sample are given in Figure. 6.7 (recall the coefficients α and β in Eqs. (6.5) and (6.6)).

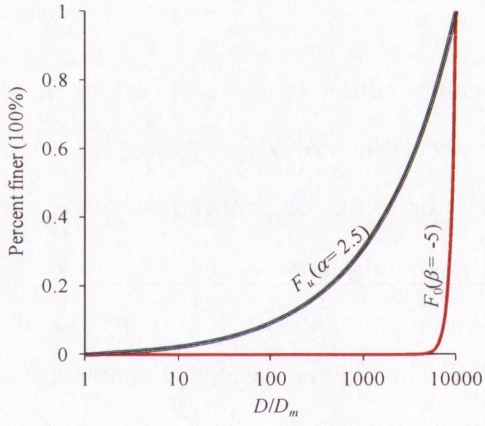

Figure 6.7 Initial and ultimate GSDs in the consolidation analysis

Two numerical studies are performed after $1.5a_0$ expansion: case 1 employs k_0 while case 2 adopts the current permeability, k, which is obtained from the modified Kozeny-Carman's equation (6.1). The variation of k at the cavity interface with the increasing cavity radius, a_c is plotted in Figure 6.8a, in which a_c starts from the initial cavity radius a_0=0.3m. At the end of expansion, when cavity radius achieves to a, the permeability distribution along the radial distance is presented in Figure 6.8b. As can be seen from both Figure 6.8a and b, the maximum permeability reduction is found to be four orders of magnitude (at cavity interface: r/a=1). Such a great reduction in

permeability seems highly probable for crushable granular soils (see Osaka-group coarse sandy soil in Section 2.2 where the finely broken sands present very low permeability, similar to those of clay). This theoretical finding reveals the inhomogeneous permeability distribution surrounding the expanding perforation in crushable granular soils. Such an inhomogeneous permeability distribution is conceptually reasonable, and should have implications on practice. In particular, the result highlights a possible drawback in the way permeabilities are currently interpreted using in-situ tests such as CPTU, which assumes homogeneous radial distribution of permeability surrounding the devise. Our current analysis should therefore motivate a new way of interpreting CPTU tests .

In view of such a great difference between k_0 and k, it is reasonable to expect a marked difference in the hydro-mechanical behaviours of both cases during the consolidation process.

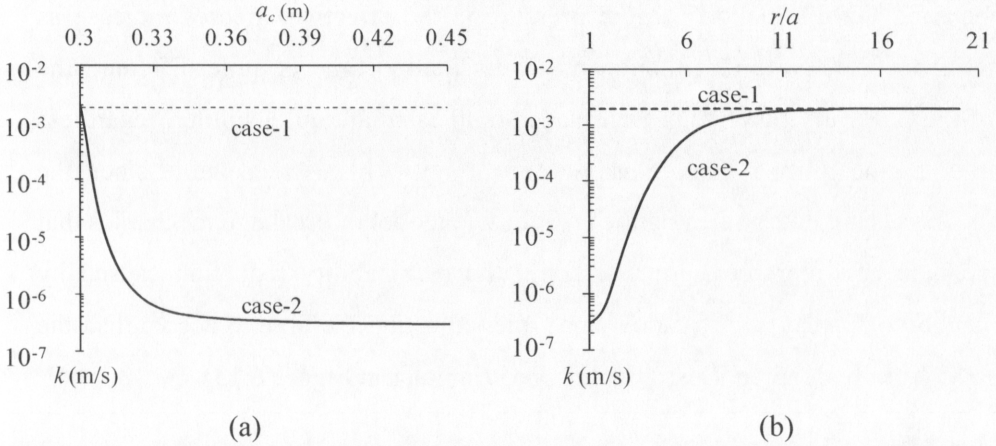

Figure 6.8 (a) Permeability variation at the cavity interface during expansion; (b) permeability distributions after undrained expansion.

The major concern here is the excess pore pressure dissipation in the two cases, which are shown in Figs. 9a and b. For case 1 (Figure 6.9a) where the permeability reduction is ignored, the dissipation time of 95% consolidation for example, is less than two seconds. This indicates an almost instant dissipation of water pressure given k_0=0.002 m/s (typical sand e.g., see Alyamani and Şen 1993). However, in case 2, based on the current k, 95% consolidation is much longer (around 200s in Figure 6.9b). This suggests that CPTU in brittle materials will take much longer time to measuring the pore pressure dissipation. It will show in next Section 5.2 that such a dissipation time can be quantified through the Poisson's ratio and friction angle.

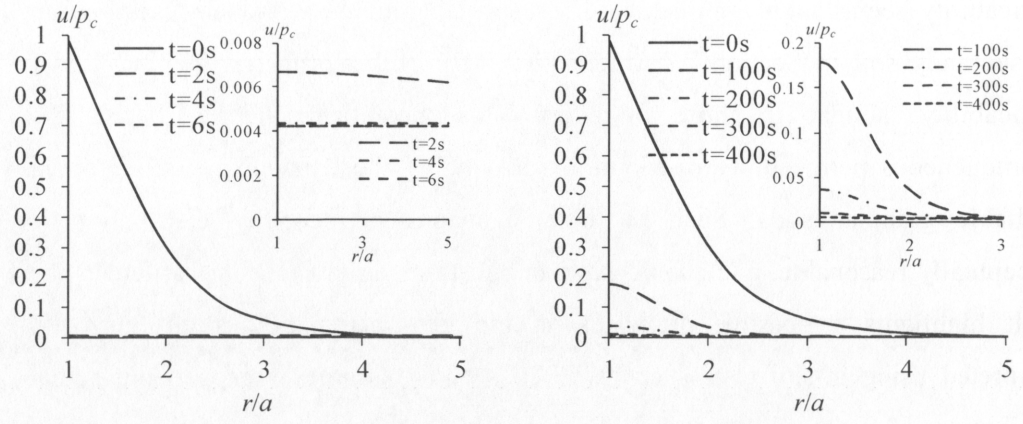

Figure 6.9 Pore pressure dissipation against radial position in (a) case 1 and (b) case 2

Detailed comparison of the excess pore pressure dissipation at the cavity interface is shown in Figure 6.10. It can be seen that the water pressure at this position decays almost instantly for case 1 while it takes a very long time in case 2. This is explained by the great reduction of permeability as shown in Figure 6.8b at r/a=1. Accompanying the dissipation of pore pressure is the effective stresses increase as seen in Figure 6.11. Note that though the consolidation time is quite different, the trends of the time-varying effective stresses in both cases are quite similar, regardless of whether permeability reduction is ignored or not. This is reasonable since the effective stresses are determined by the constitutive model of breakage mechanics that is independent of water pressure. Therefore, the permeability reduction caused by grain crushing only plays a 'time-delaying' role, adjusting the time to accomplish the stress paths (a more detailed illustration can be seen later in Figure 6.13).

As u decreases the effective stress σ_r' increases (see Figure 6.11). However, the total radial stress is found to decrease as shown in Figures 6.12a and b, due to decreasing u and increasing σ_r'. This exhibits the determinable role of excess pore pressure in controlling the development of total radial stress in brittle granular media. Interestingly, this is consistent with numerical and experimental observations of clay consolidation (Carter et al. 1979).

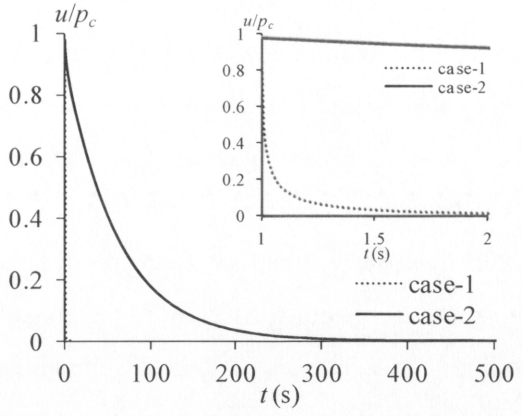

Figure 6.10 Decay of pore pressure at cavity interface for both cases

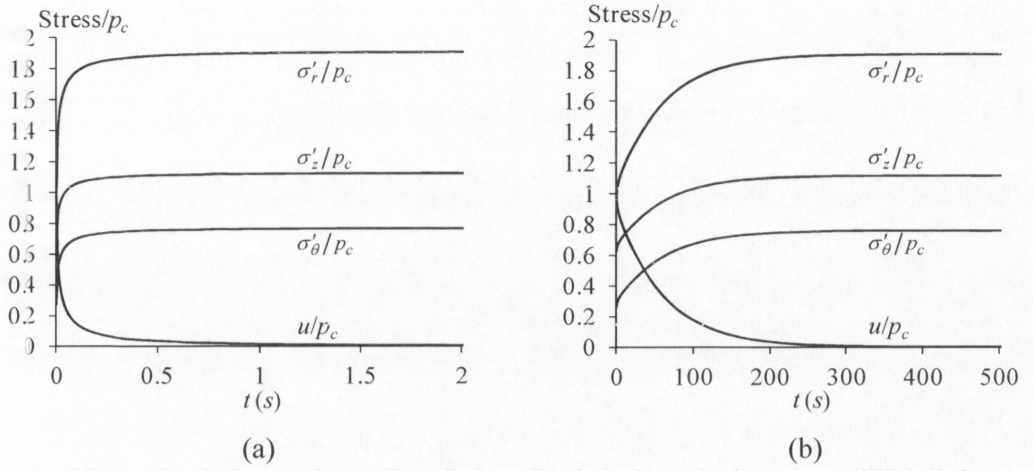

Figure 6.11 Variations of stress at the cavity interface during consolidation for (a) case 1 and (b) case 2

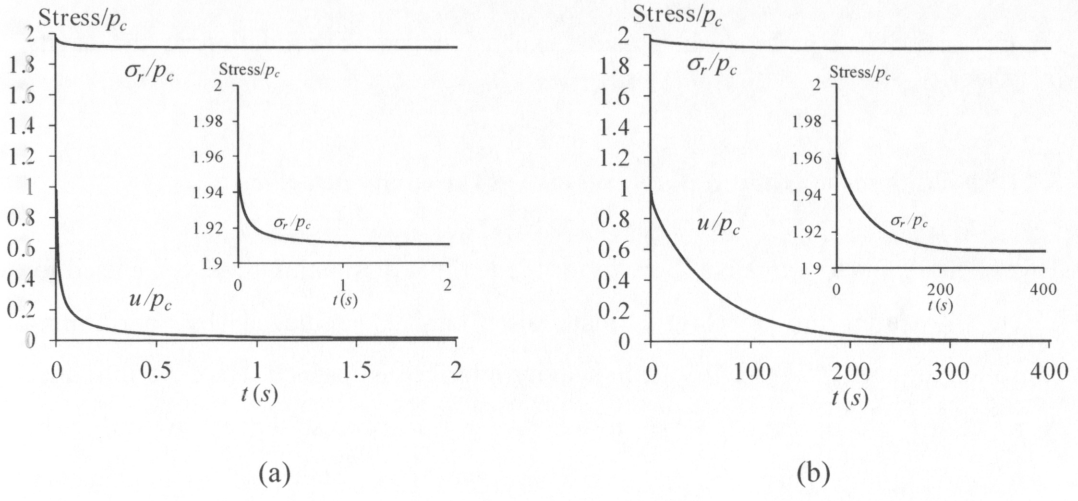

Figure 6.12 Variation of pore pressure and total radial stress during consolidation at the cavity interface for (a) case 1 and (b) case 2

Figure 6.13 depicts the stress path at the cavity interface for both cases, providing some insights into variations of effective and total stresses. At the end of the expansion, the stress state is at near failure (i.e., the isotropic hardening component of the breakage yield envelope is almost fully resourced). Therefore, the second stage of consolidation occurs fully within the expanded elastic domain. Together with the linearity of Darcy's law, both the effective and total stresses follow linear paths. As seen in this figure, although k and k_0 are quite different in the consolidation stage, the stress paths are identical in both cases. This again indicates the unique stress path that is exclusively determined by the given constitutive model. Nevertheless, the time it takes to travel along this unique path is significantly different and determined by current permeability due to grain crushing. In addition, the excess pore pressure, as the difference between the plotted total and effective stresses, increases during expansion and decreases to null during consolidation.

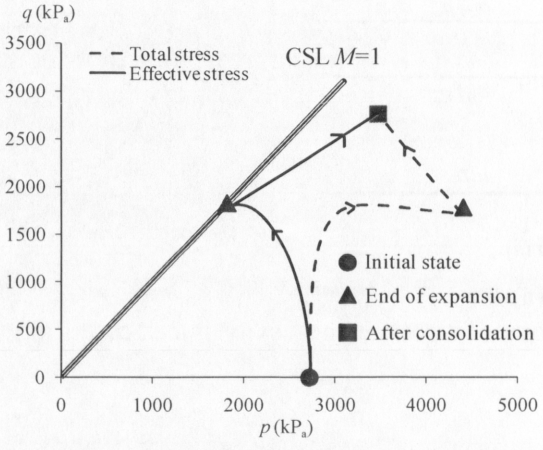

Figure 6.13 Stress paths during cavity expansion and consolidation at the cavity interface

5.2 Dissipation of maximum pore pressure at the cavity interface

This section aims to provide a formula for the optimal dissipation time, to be used for CPTU measurements in brittle materials. This is achieved by performing consolidation analysis after u_{max} at the cavity interface is reached. Here we introduce t_{95} to define the dissipation time for 95% consolidation at the cavity wall. The corresponding t_{95} versus p_0/p_c are plotted in Figure 6.14 in terms of the fundamental parameters of the current breakage constitutive model.

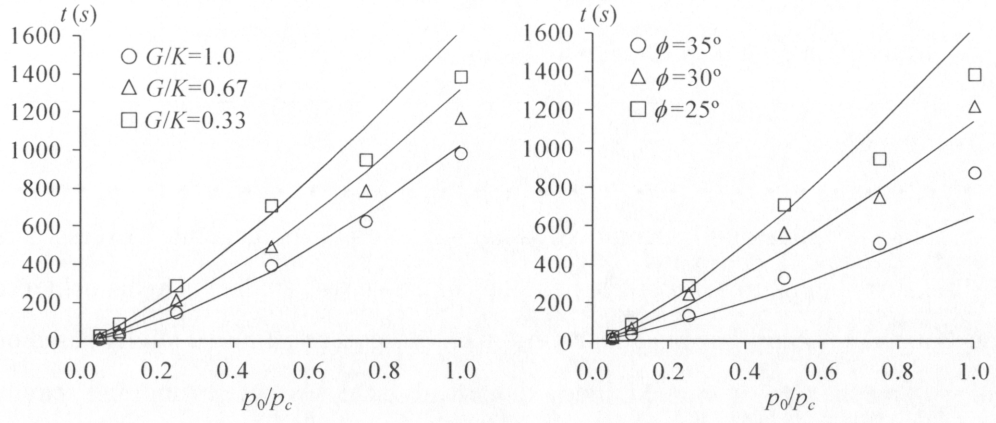

Figure 6.14 Dissipation of maximum pore pressure at cavity interface during consolidation under different isotropic confining pressures with (a) effects of G/K; (b) effects of ϕ (other model parameters, if not varied, are listed in Table 6.1). The solid lines are fitting curves for each simulation.

Interestingly, these relationships in Figure 6.14 could also be practically accounted for by another power law function of (6.9) and alternatively by (6.10) by using a standard approximation of the relationship between M and ϕ, Poisson's ratio and elastic moduli:

$$t_{95} = \alpha\left(\frac{p_0}{p_c}\right)^{\beta} = \left(4350 - 900\left(\frac{G}{K}\right) - 2430M\right)\left(\frac{p_0}{p_c}\right)^{0.3\left(\frac{G}{K}\right)+1.2} \tag{6.9}$$

$$t_{95} = \alpha\left(\frac{p_0}{p_c}\right)^{\beta} = \left(4350 - 1350\left(\frac{1-2v}{1+v}\right) - 14580\frac{\sin\phi}{3-\sin\phi}\right)\left(\frac{p_0}{p_c}\right)^{4.5\left(\frac{1-2v}{1+v}\right)+1.2} \tag{6.10}$$

The coefficient α and β for (6.9) or (6.10) are given in Table 6.3.

Table 6.3 Parameters for (6.9) or (6.10)

Parameter	Value	α	β	R^2
G/K	0.33	1623	1.3	0.991
	0.67	1317	1.4	0.996
	1.0	1020	1.5	0.986
ϕ	25°	1623	1.3	0.991
	30°	1137	1.3	0.986
	35°	651	1.3	0.978

From (6.9) or (6.10), it can be deduced that $t_{95} \propto \vartheta^{-[0.15(G/K)+0.6]}$. This relationship shows that the finer the graded granular soils (smaller ϑ), the more time the pore

pressures need to dissipate to achieve 95% consolidation. This is again relevant to the bigger tortuosity in granular system with wider gradations.

6 Summary

The problem of expanding perforation damage zones and the generated excess pore pressure surrounding those in brittle granular materials was studied. This is achieved through a general grain-crushing analysis that embraces a constitutive model based on breakage mechanics integrated into numerical analyses of cylindrical cavity expansion problems. Thanks to the explicit connection between the breakage internal variable and the evolving GSD of the constitutive model, this general approach enables us to assess both the stress fields and the characteristics of the damage zone. This allows the correct prediction of the permeability reduction, and thus the excess pore pressure, especially in undrained condition when grain crushing is the sole contributor to this reduction. On this basis, our parametric study suggests practical formulae to predict the generation and dissipation of pore pressure in cavity expansion problems. These formulae give estimation of the maximum pore pressure and the time to dissipate this pressure, as functions of the material properties. The suggested formulae (Eqs. 17 and 19) may be helpful to in situ soil testing, deep foundations, tunnels, underground excavations in soil and rock, and sand-, gas- and oil-producing perforations.

Despite the fact that the studied problem is a cylindrical cavity expansion, applications of the general grain-crushing analysis to practical applications, for example to analyse a cone penetration test (CPT), is rather straightforward. Variations of geometry, initial/boundary conditions, and model parameters for a perforation can be readily taken into account in a Finite Element model, as shown in this study.

Chapter VII

Extracting relationships of energy-size reduction in comminution using continuum mechanics principles

1 Introduction

Energy efficiency is the key to the viability of industrial comminution processes. Although a great deal of effort has been focused on the relationship between energy consumption and grain size reduction, little has been gained towards the application of these studies for improving the efficiency of industrial comminution processes. As a consequence, in practice the energy delivered to the comminution still accounts for a very small amount of the total energy consumed in a typical grinding operation (e.g. approximately 4% (Tavares and King 1998)). Conventional mathematical formulas such as the three grinding laws (Rittinger 1867; Kick 1885; Bond 1952) were proposed to describe the energy-size reduction relationship of a single particle. However, none of those classic approaches actually work as expected (Hukki 1962). A typical problem is the selection of an adequate (reference) grain size. With plenty of mineral particles, there is no one exclusive size. Use of different grain sizes (i.e. D_{10}, D_{50} or D_{80}, as the sieve sizes on which 10%, 50% and 80% of the overall sieved mass remains, respectively) will lead to different the energy-size relationships. That results in each model working in a different and limited range.

Rigorous models derived from population balance principles (Ramkrishna 2000) (PBM) could deal with particles of various sizes. Through the introduction of new concepts such as selection functions and breakage functions, prediction of the energy-size reduction relationship was improved (e.g. Kapur 1971; Kapur and Fuerstenau 1987; Kapur 1990; Fuerstenau et al. 1991). However, the parameters required in

those functions are empirically fitted to product GSDs without a clear connection to the energetics of the comminution process. This process itself is complex, with the fracture and fragmentation of grains, followed by the flow of grains and their fragments. The input energy is therefore not only consumed by the grain fracturing process, but also dissipated from friction, acoustic emission, heat transfer, and redistribution of strain energy (Nguyen and Einav 2009). Describing properly this process is beyond the ability of PBMs since they are underpinned by mass balance but not energy.

An interesting way to deal with granular comminution is to use the DEM (discrete element method). Whereas DEMs allow a detailed study of the micro-dynamics of particles, they are generally computationally intensive, which results in a limit either in the duration of a simulation or in the number of particles (Cleary 2001; Cheng et al. 2004; Ben-Nun and Einav 2010). The results are highly sensitive to minor perturbations in the initial conditions and easily affected by numerical noises. Moreover, it is difficult to determine and calibrate the constitutive force-displacement relationship describing the contacts between grains.

Alternatively, continuum mechanics is also widely used to model granular materials as a continuum, assuming smeared representative volumes. This requires less computational power than DEM study, while relying on the accuracy and reliability of the continuum model characterizing the complex behaviour of the material at the grain scale. Given the importance of tracking the evolving GSD during comminution, the breakage theory described in Chapter III is a good starting point for a continuum based study of comminution processes. Our present work aims to offer a good way for gaining insight into grain crushing and energy consumption in comminution via the newly developed theory of continuum breakage mechanics (Einav 2007a, b). This theory and a linear elastic breakage model have been described in detail in Chapter III. In the next section, the Finite Element analysis of a roller mill will be performed using the breakage model described in Chapter III. The distribution of grain crushing represented by the contour of breakage variable will be presented. In the following Section 3, the predicted breakage distribution will be used to calculate the product cumulative GSD and moment (rotation) work. The resulting product cumulative GSD

and moment work are calculated in Section 4 in this chapter, and then verified against experimental counterparts. On this basis, the energy-size reduction relationships are further explored in a parametric study taking into account various rollers' gaps and grinding (rotation) speeds.

2 FEA of comminution of granular materials in a roller mill

Fuerstenau et al. (1991) carried out a roller mill experiment for quartz sand. They measured the product cumulative GSDs of the sand and input energy in comminution with different roller gaps. Both measurements will be used to validate the numerical results in this Section.

In the following, numerical results are based on the Eulerian formulation in FEA where nodes stay fixed while the model material flows through the mesh (abaqus 2010). This analysis configuration is selectively different that the ALE method employed for section 2, Chapter V, which benefits from the inherent self-similarity of the geometry. The Finite Element model (FEM) is depicted in Figure 7.1a. Here, the model size is big enough to well accommodate the possible grinding-influenced zone between the two rollers. Note that the geometry of the roller mill is symmetrical, therefore only half of the domain was modelled in FEA.

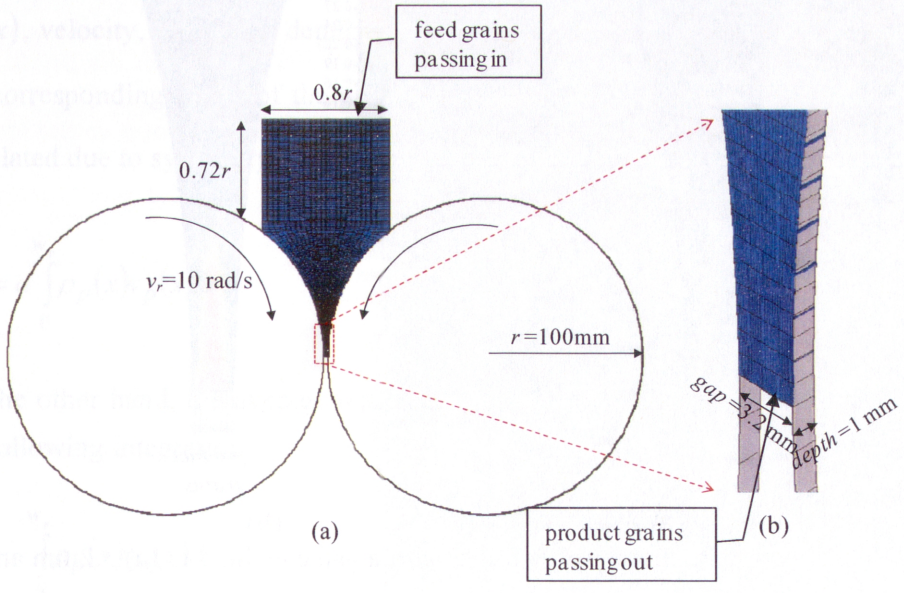

Figure 7.1 Numerical modelling of a roller mill; and (b) zoomed domain near rollers gap. The dimensions are referred to the experiment of Fuerstenau et al. (1991). Note that only the right half of the model is created in Finite Element analysis.

Due to the lack of experimental data for the constitutive behaviour of that particular quartz sand in Fuerstenau et al. (1991), we have decided to employ a set of parameters from Fontainebleau sands, for the merits of its being a typical quartz sand. This sand has a density of around 2000 kg/m^3. Using data from a series of triaxial compression tests on this quartz sand (De Gennaro and Frank 2002), we have estimated the following mechanical parameters: K=28.3MPa, G=13.1MPa and M=1.5 (based on effective friction angle of ϕ=36°). From the 1D compression test by Yang et al. (2010) the critial comminution pressure is p_c = 23MPa. The sand-steel (i.e. the roller material) interface friction coefficient μ=tan(ϕ_p) is calculated using the measured interface friction angle ϕ_p =25°. This friction, together with the gravity (10N/kg), causes the feed quartz sand to move through the rollers. In addition, based on the initial GSD in Yang et al. (2010) the grading index is taken as ϑ=0.92 (where the ultimate cumulative GSD was assumed to follow a fractal grading with a fractal dimension α=3.0 in equation (3.5)). All simulations run until a steady state (i.e. the breakage distribution becomes stable) is achieved. The results of breakage distribution between the two rollers during steady state comminution are presented in Figure 7.2a-b, for the cases when the roller's gap equals to 3.2mm and 2.8mm, respectively.

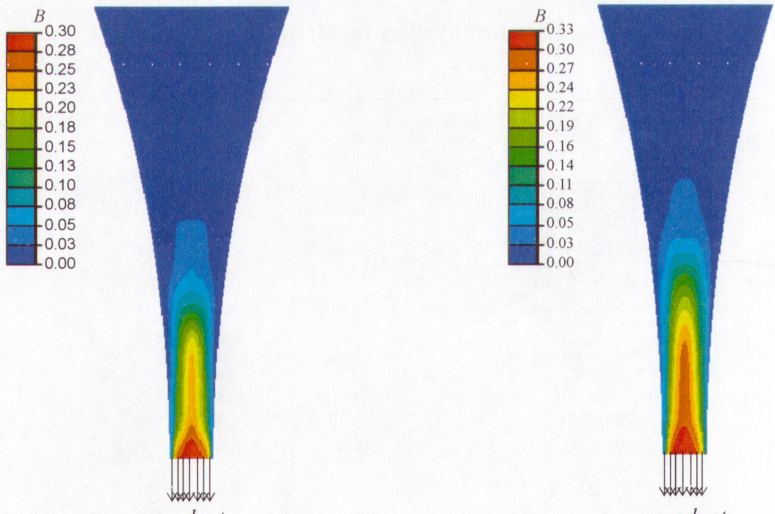

(a) (b)

Figure 7.2 Breakage distribution in roller mills, with a gap equalling to (a) 3.2mm and (b) 2.8mm

3 Interpretation of numerical results

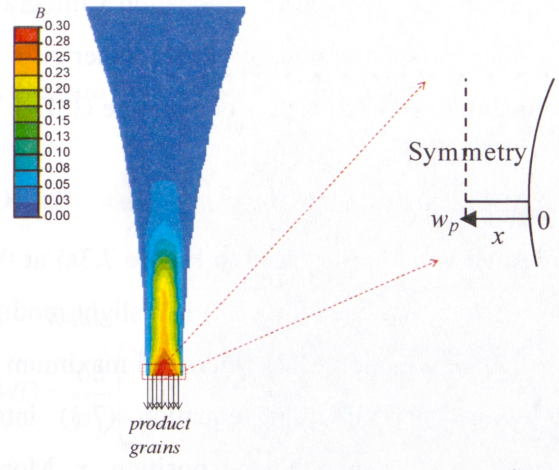

(a) (b)

Figure 7.3 (a) breakage distribution between the two rollers (an example when gap=3.2mm); and (b) zoomed domain near rollers' gap

This section explains a way to associate the FE numerical results of breakage to calculate the product cumulative GSD and moment (rotation) work. Take the right half domain as an illustration (as seen in Figure 7.3b), the product mass flux of grains (per second), Q_p (subscript 'p' denotes '*product*' variables in all followings), can be found through mass balance, by integrating the mass fluxes as a function of density, $\rho_p(x)$, velocity, $v_p(x)$ and depth, a (i.e., 1mm already indicated in Figure 7.1b) over the corresponding width of the product gap, w_p (only the right half of the roller is simulated due to symmetry):

$$Q_p = a\int_0^{w_p}\rho_p(x)v_p(x)dx \tag{7.1}$$

On the other hand, the average density, $\overline{\rho}_p$ of the grains over w_p is calculated using the following integration:

$$\overline{\rho}_p = \frac{\int_0^{w_p}\rho_p(x)v_p(x)dx}{\int_0^{w_p}v_p(x)dx} \tag{7.2}$$

Considering the fact that the maximum product grain size, D_{Mp}, cannot be larger than $2w_p$ and taking into account the maximum feed size, D_{M0}, a simple assumption is made, that is $D_{Mp} = D_{Mp}(x) = \min[2x, D_{M0}]$. Therefore, at location x the grains of size over D_{Mp} become 100% finer in their product cumulative GSD, otherwise, other feed grains obey the following relationship to generate a new cumulative GSD:

$$F_p\left(D, D_{Mp}, B_p, x\right) = F_0\left(D, D_{Mp}, x\right)\left(1 - B_p\right) + F_u\left(D, D_{Mp}, x\right)B_p \tag{7.3}$$

where $B_p = B_p(x)$ defines the breakage variation (as seen in Figure 7.3a) at the product gap, depending on the location, x. Note that equation (7.3) is a slight modification of equation (3.2) (Chapter III), i.e. unlike equation (3.2) where the maximum grain size is assumed unchanged after grains comminution, equation (7.3) introduces a changeable maximum grain size of D_{Mp}, depending on position, x. Moreover, the weighted average of $F_p\left(D, D_{Mp}, B_p, x\right)$ along x is expressed as:

$$\overline{F_p}(D) = \frac{\int_0^{w_p} F_p\left(D, D_{Mp}, B_p, x\right)\rho_p(x)v_p(x)\,dx}{\int_0^{w_p} \rho_p(x)v_p(x)\,dx} \tag{7.4}$$

which represents the experimentally measurable cumulative GSD of the product material. By differentiating the $\overline{F_p}(D)$ with respect to D, we can obtain the product GSD, $\overline{p_p}(D)$. This distribution is used to calculate the mass flux of grains in the size bin from D-dD/2 to D+dD/2 (say, the D-bin):

$$q_p(D) = Q_p\overline{p_p}(D)dD = a\left(\int_0^{w_p}\rho_p(x)v_p(x)dx\right)\overline{p_p}(D)dD \tag{7.5}$$

As the volume of a single grain of size D can be approximated by a typical sphere

$$V(D) = \frac{\pi(D)^3}{6}, \tag{7.6}$$

the produced (ejected) numbers of grains in the D-bin can be calculated given the mass flux $q_p(D)$:

$$V_p(D)=\frac{q_p(D)}{\overline{\rho}_p V(D)}=\frac{a\left(\int_0^{w_p}\rho_p(x)v_p(x)dx\right)\overline{p_p}(D)dD}{\overline{\rho}_p V(D)} \tag{7.7}$$

Next, we can calculate their total product surface area of all grains within the D-bin:

$$s_p(D)=N_p(D)\cdot\pi D^2=\frac{6q_p(D)}{\overline{\rho}_p\pi D^3}\pi D^2=\frac{6a}{\overline{\rho}_p}\left(\int_0^{w_p}\rho_p(x)v_p(x)dx\right)\frac{\overline{p_p}(D)}{D}dD \tag{7.8}$$

Finally, the total product surface of all grains is given by:

$$S_p=\int_{D_m}^{D_M}s_p(D)dD=\frac{6a}{\overline{\rho}_p}\left(\int_0^{w_p}\rho_p(x)v_p(x)dx\right)\left(\int_{D_m}^{D_M}\frac{\overline{p_p}(D)}{D}dD\right) \tag{7.9}$$

Similarly, the total feed surface for all grains is:

$$S_f=\frac{6a}{\overline{\rho}_f}\left(\int_0^{w_f}\rho_f(x)v_f(x)dx\right)\left(\int_{D_m}^{D_{M0}}\frac{\overline{p_f}(D)}{D}dD\right) \tag{7.10}$$

where subscript p in equation (7.9) was replaced with f to denote the corresponding feed variables. Therefore, the new surface generated (per second) is:

$$\Delta S=S_p-S_f \tag{7.11}$$

On the other hand, the moment work in our simulation can be calculated from the instantaneous moment $M(t)$ and grinding velocity v_r:

$$W=\int M(t)d\theta=v_r\int M(t)dt \tag{7.12}$$

Thus the moment work rate, E_m is the slope of W with respect to time. The calculated ΔS and E_m are adopted to elaborate the energy-size reduction relationship in Section 4 in this chapter.

4 Results of product cumulative GSD and assumed moment (rotation) work

Based on the estimation method in Section 3 in this chapter, the product cumulative

GSDs for two cases of different roller gaps are plotted against the experimental counterparts as seen in Figure 7.4b and Figure 7.5b. Interestingly, such good comparisons are found with the plastic-breakage coupling angle $\omega=\phi=36^{o}$. The disagreement is probably mainly caused by loosing some of the rigor of the breakage mechanics formulism towards obtaining practical results. As explained previously, we changed the maximm diameters of particles artificially by x. This means the grading index ϑ (equation 3.20) should ideally be considered as an internal variable, such that the thermodynamics formulation requires to acknowledge more terms and dependencies, and thus becomes more complicated than the present linear elastic breakage model that has not considered such variations of ϑ. Having said that the current work makes only the first step towards the study of mineral comminution problem using the breakage mechanics theory. In the future, one would need to consider the changes of the maximum diameters within the themodynamics framework.

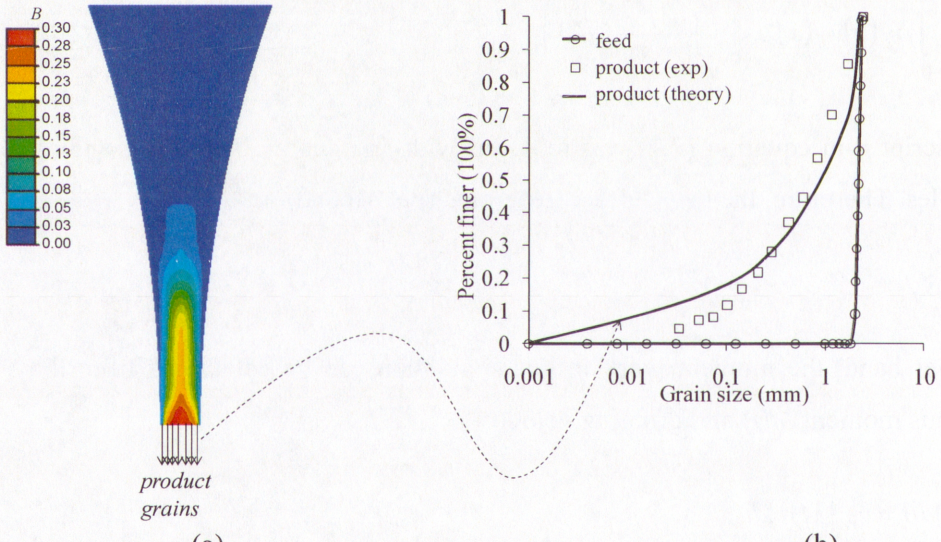

(a) (b)

Figure 7.4 Comminution of quartz sand ground through a roller mill (gap=3.2mm): (a) theoretical prediction of breakage, and (b) experimental and theoretical cumulative GSDs of product grains

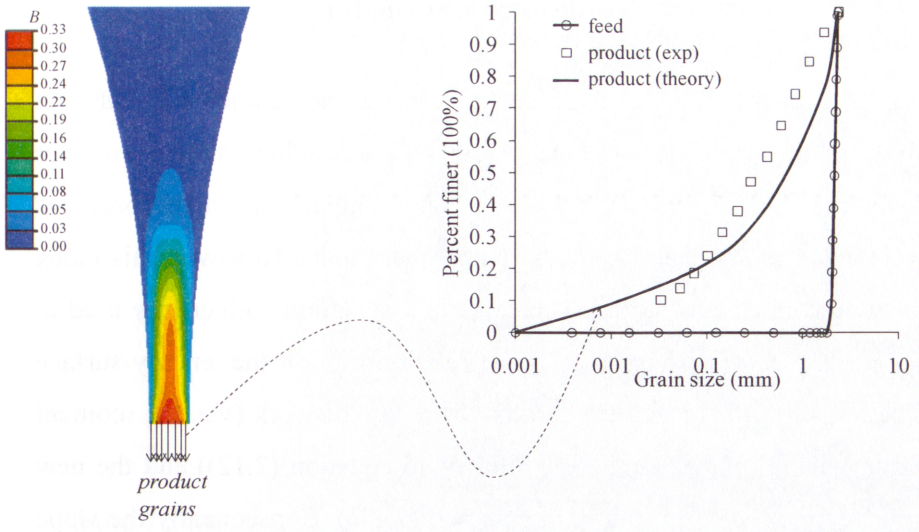

(a) (b)

Figure 7.5 Comminution of quartz sand ground through a roller mill (gap=2.8mm): (a) theoretical prediction of breakage, and (b) experimental and theoretical cumulative GSDs of product grains

In addition, from the Section 3 the flux of product mass, Q_p, and the input (moment) work, W are respectively calculated. Thus, the energy per unit mass (i.e., with the unit of kWh/ton) can be obtained, and is then used to compare with experimental measures in Fuerstenau et al. (1991). The numerial moment works are 1.05kWh/ton (for gap=3.2mm) and 1.39kWh/ton (for gap=2.8mm) while the experimental measures of total energy input (including moment work) are 1.17kWh/ton and 3.11kWh/ton, respectively. The numerical predictions of moment work are always smaller than the experimental input energy. This is probably because the continuum model cannot include the full detail of the operation, especially neglecting energy consumption from the facility itself, e.g. the dissipation due to belts, gears, etc.

It is also important to note that the predictions of the product GSDs and moment work may be improved by using the accurate parameters of the quartz sand that was used in Fuerstenau et al. (1991). Additionally, our present breakge model has not taken into account the possible dependence of the elastic shear and bulk moduli on pressure. Significant improvements might also be expected through the employment of a pressure dependent breakage model. Future work is, of course, needed to resolve this aspect.

5 Exploration of energy-size reduction relationship

In Engineering, a grindability index is used to describe the relationship between energy (or work) and the size of mill products. Such an index indicates the energy per unit mass or volume, i.e. J/kg or kWh/ton, etc. The comparisons in the previous section used this index to validate our model with experiments. However, this index does not indicate how much new surface is created in association with energy used in comminution. A simple way to present such relationship of the energy-surface creation (or size reduction) is to plot the results of the rate of work (viz. the moment work only in our simulation), E_m (unit: J/s, referred to equation (7.12)) and the new surface flux (per second), ΔS (unit: m^2/s in equation (7.11)). Consequently the slope of the relationship between E_m and ΔS is defined as γ, indicating the energy per unit surface area (J/m^2). The index γ can be therefore used as an alternative index of grindability. This provides a straightforward understanding of the relationship between the moment work input and the increased surface areas during the grains passing through a roller mill. Some recent research also supports the use of energy per unit surface area (i.e. γ) to represent the grindability of a mill (e.g. Stamboliadis 2007).

The Finite Element model is also based on Figure 7.1 but now with an industrial roller size of 1.4m in diameter (Benzer et al. 2011). In addition, various rollers' gaps and grinding speeds, v_r are tested to obtain different E_m and corresponding ΔS. The same quartz sand as in Section 3 in this chapter is used in a series of simulations, except the index property $\vartheta = 0.81$ that is based on the initial cumulative GSD in Figure 7.7 (again, with a fractal dimension α=3.0 in equation (3.5)).

The results of E_m versus ΔS are plotted in Figure 7.6, in which two fundamental findings can be summarised.

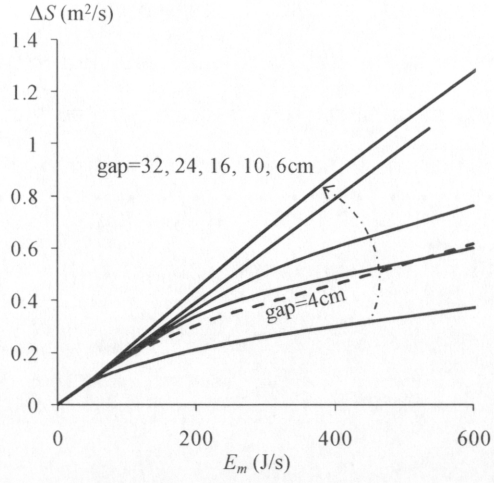

Figure 7.6 Moment work rate, E_m versus increased surface (per second), ΔS

First, for any given rate of work E_m, the maximum surface flux ΔS is achieved when the roller's gap is 6cm. In our present investigation, the optimum gap in terms of maximizing the new surface created is of interest. As comparing with other cases given the same moment work, the case of 6cm gap always produces a maximum surface flux. The existence of the optimum gap is reasonable and can be explained as follows. The newly created surface flux, ΔS (calculated in Section 3 A1) is relevant to two competing factors: the amount of product grains (or flux of grain mass) ejected from the rollers, and the degree to which those grains are crushed. Both factors are dependent on the width of the rollers' gap. In detail, in the case of a very large gap, ΔS is obviously very small as the feed grains undergo little crushing after comminution although the quantity of grain is very large. However, in the case of a very small gap, ΔS is also very small because only a small quantity of product grains is ejected, although those grains undergo very severe crushing. Therefore, there is an optimum gap to allow maximum surface generated with least work consumed, as indicated in Figure 7.6.

Second, the slope of the curves, i.e. the proposed index γ of grindability, gets smaller with increasing rate of work E_m in all cases of various gaps. Since the increasing E_m was caused by the increased rotating (grinding) speeds, it can be said that less surface area is produced as grinding speeds increase. In other words, the energy efficiency to create new surface areas reduces with increasing grinding speed. This agrees with the observation in comminution industry (e.g. Stamboliadis 2007).

Figure 7.7 gives an example of the predicted cumulative GSDs regarding different roller gaps, which corresponds to E_m=600J/s. Unlike the cumulative GSDs in Figure 7.2 where the initial maximum grain size, D_{M0} is less than the gap, here D_{M0} is taken as 20cm so that it is larger than or equal to the modelled gaps of 20cm, 10cm and 6cm. One can see that in the cases of 10cm and 6cm gaps, the product cumulative GSDs are entirely shifted, including the maximum size as well.

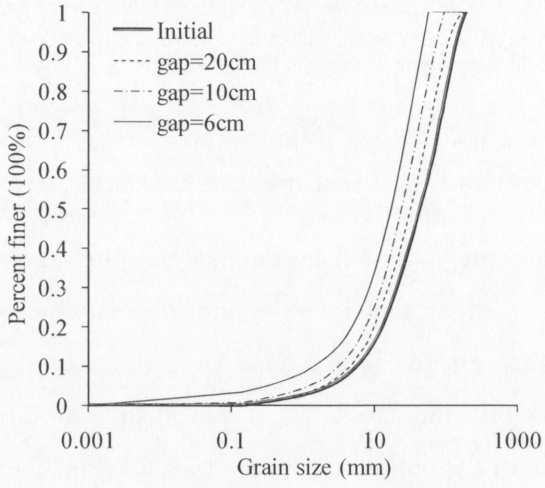

Figure 7.7 An example of product cumulative GSDs predicted by the proposed method

6 Conclusions

This chapter makes the first use of a continuum breakage model to study the energy-size reduction relationship in comminution in a roller mill. This model places the focus on connecting the evolution of the GSD with the macroscopic granular behaviour, which enables monitoring of the breakage distribution during the passage of grains through the rollers. The present study validates the capability of this model by relatively well predicting the product cumulative GSDs and associated (moment) work input in the corresponding experiments.

Despite the fact that the studied problem is a roller mill, applications of breakage mechanics theory to other comminution problems, for example a ball mill, is rather straightforward. Variations of geometry, initial/boundary conditions, and model parameters for a milling problem can be readily taken into account in a Finite Element

model, as shown in this study. This opens a new potential for the optimization of grinding operations for better energy efficiency.

Chapter VIII

Summary and further research

1. Summary

This thesis opens a new domain of applications of breakage mechanics theory using Finite Element Method (FEM). Throughout the work for this thesis, it became clear that different optimal numerical schemes might be needed to find the solutions for various problems. Therefore, the main contributions in this thesis involve three distinguishable methods for the solutions:

- A Lagragian FE model is developed and used to deal with the undrained cavity expansion problem in the brittle granular medium, and the generation/dissipation of excess pore pressures.
- An Arbitrary Lagragian Eulerian (ALE) FE model is developed and used to study the cone-ended pile penetration into crushable granular soil, with a focus on GSDs in space and time.
- An Eulerian FE model is developed and used to simulate grain crushing effects on granular material flow in highly constrained geometries, including the end-bearing capacity of a flat-ended pile in crushable soils and energy-size reduction relationships in mineral comminution.

The main contributions and suggestions for future improvements are summarised in the following sub-sections.

1.1 End-bearing capacities of piles in crushable soils

A new formula for the end-bearing capacity of piles penetrating into crushable soils was proposed in Chapter V. The formula is based on the linear elastic breakage model (Chapter III) that accounts for the evolution of the grain size distribution (GSD) due

to grain crushing with only physically meaningful parameters. The model is integrated using the FEMs (both ALE and Eulerian methods) to study the penetration problem. Predictions of GSDs surrounding piles and pile end-bearing capacities are validated against experiments. This is followed by a parametric study carried out to quantify the effects of grain crushing on the end-bearing capacity and then to establish the formula.

This new equation treats the end-bearing capacity from a more comprehensive and physical perspective. Unlike the conventional or other existing formulae that mainly or solely rely on the granular frictional angle, the new equation considers the confining pressure p_0, GSD (via ϑ), critical breakage energy E_c, elastic Young's modulus (E) and Poisson's ratio (ν), and the friction coefficient M (via friction angle). All those parameters are easy to measure using regular soil tests (e.g., isotropic or 1-D compression tests followed by a conventional drained shear test) without any unusual technique.

Comparing the proposed equation to several other equations indicates the advantages of the new formula in predicting the end-bearing capacities of piles in crushable sands. In addition, the new formula enables us to quantify the influence of initial GSDs on end-bearing capacities (see Figure 5.10, Chapter V). This issue has been emphasised widely but was missing from previous equations.

1.2 Generation and dissipation of excess pore pressure in cavity expansion

Chapter VI studies the excess pore pressure generated and then dissipated from expanding perforations in brittle granular soils. This linear elastic breakage model has been implemented in a Finite Element package for the analysis of a cylindrical cavity, under undrained followed by drained (i.e. consolidation) conditions. This analysis shows the significant effects of grain crushing on the dissipation time of pore pressures, thus highlighting the importance of tracking the evolving GSD in modelling the hydro-mechanical response of granular materials. On the basis of this analysis, formulae are proposed for predicting the generation and dissipation of the pore pressure at the cavity interface. The predictions are correlated with the initial confining pressure, initial GSD, comminution pressure that defines yielding, the friction coefficient and the elastic stiffness of the material.

The results of this analysis may be useful for the interpretation of CPTU tests, which are often used to estimate the in situ horizontal coefficient of consolidation and coefficient of permeability. In contrast to previous theoretical interpretations (e.g., using the cavity expansion theory and the strain-path approach) that focus on clay, the proposed approach enables us to quantify the effects of grain crushing on the excess pore pressure dissipation in crushable soils.

Note that the mobility of the fragments, i.e., the erosion, has not yet been considered. After grains have been broken in undrained followed by fluid dissipation, the fragments may migrate and clog. As a result, local permeability can change because the fragments start to move. This is the real physical phenomenon that so far we have been unable to take into account. We have to assume that: the fragments remain in the same places, there is no erosion, and the whole mass of the material is retained.

Despite these assumptions, simplifications and limitations, this research, by accounting for grain crushing in interpreting the hydro-mechanical response in undrained cavity expansion is pioneering.

1.3 The energy-size reduction relationship in comminution in a roller mill

A new continuum approach for predicting the energy-size reduction relationship in comminution is proposed in Chapter VII. The approach is based on a breakage mechanics model that accounts for the evolution of the GSD due to granular comminution with only five parameters, all of which are physically meaningful. The model is implemented and used in FEA to study the energy-size reduction relationship in a roller mill. Predictions of product GSDs and energy consumption are validated against experimental counterparts. On this basis, a series of parametric studies in terms of various rollers' gaps and grinding speeds are carried out in order to explore: 1) the optimum roller gap, which is the maximum area of new surface that can be created with the least input work; and 2) the influence of increasing grinding speeds on new surface creation.

A challenge in the current modelling is that the rollers' horizontal force and movements have not been included, while such horizontal compaction is an important feature for high-compression roller mills. A possible solution might be to introduce a

spring element to replace the horizontal constraint, and then apply horizontal force to this spring element.

2. Further research

2.1 Enhancements in the model behaviour

The problems solved in this thesis involve complexity on different levels, from material modelling complexity to geometric complexity. In this author's opinion, it is not feasible to include all of the complexity at once. A practical approach is to take one step at a time. For that purpose, this thesis has used the linear elastic breakage model. This is a simplification that should be noted. Considering the complex geometric factors in the studied models, this linear elastic breakage model may yield reasonable results that may be of benefit to engineering applications.

Future work may use a more complicated model with a refined assumption that may enhance the model's performance. For instance, the breakage model based on nonlinear elasticity (Section 6.2, Chapter III) that accounts for Hertz contact among particles.

In addition, the porosity-dependent behaviour of the granular materials is another important concern. We can deal with porosity dependence now in a very simple way by introducing a porosity-dependent bulk modulus (Einav 2007d). For example, in studying pile penetration problems, if the porosity-dependent bulk modulus is introduced, the pile end-bearing capacity is also considered as porosity dependent (due to p_c relevant to porosity), nevertheless this is very simplified. A more satisfactory future approach may be to implement an advanced model that rigorously accounts for porosity (i.e., the model in Rubin and Einav 2011).

It is also realised that the breakage model assumes one unique evolutionary path that the GSDs follow as they propagate from initial to ultimate curves. This is a simple assumption, which may not necessarily reflect the real situation because the evolving GSDs may also depend on load paths. In other words, patterns of grain crushing—for instance, during shearing and compression—are varied: the grain crushing is due mainly to attrition in shearing while to bulk failure in compression. A more rigorous

assumption regarding GSD's evolutionary path might be helpful in order to better capture the change of microstructures of granular assemblies. This may improve the model's capability to better predict the granular macroscopic response due to grain crushing.

2.2 Engineering application aspects

An interesting topic in the future would be to examine the capacity of the proposed new formula for predicting the end-bearing capacity of piles. This would require collecting more data on the end-bearing capacities of piles in order to further verify the proposed new equation. Such a collection may by no means be restricted to calcareous/carbonate brittle materials. Relatively hard granular materials, i.e. quartz and silica sands, may also be useful, as those will break under high stress levels. However, it might not be an easy task because the critical comminution pressure, p_c, which marks isotropic yielding, is usually missing in measurements of model pile or in situ tests. Consequently, it would be worthwhile conducting many new model pile tests of various sands, provided that the following parameters are known beforehand: the p_c, Poisson's ratio ν, the effective friction angle ϕ, and the shear modulus G.

It may also be worthwhile to continue modelling the mineral comminution in the mining industry. Chapter VII presents a demonstration in a roller mill; however, there are many more mills worth studying, like ball mills. This author plans to introduce a nonlinear elastic breakage model to further model the granular behaviours in comminution in various mills. Considering the high demand for reducing mineral comminution energy costs in the mining industry, further studies, as outlined above, would be highly beneficial.

Another challenging future project is to improve the numerical technique to model the large granular flow problem. The current models are based on Eulerian or ALE FE methods, which would unavoidably cause some oscillation in output results due to the remeshing technique. Alternative models may include the Material Point Method (MPM) (Sulsky et al. 1994; Daphalapurkar et al. 2007), which is very rigorous in modelling the flowing problems; and the mesh free method (Arroyo and Ortiz 2006; Netuzhylov and Zilian 2009; Liu 2010) without being concerned about mesh

distortion. Current work is being carried out in the Particles and Grains Laboratory led by Dr Nguyen at the University of Sydney.

In addition to the topics in this thesis, there are extensive applications for breakage mechanics theory and its various models.

Consider the coffee bean grinder: the first example presented in the literature review. The coffee bean crushing process can be modelled through the Eulerian FE technique or MPM. This process is the same as used in the modelling of the roller mill in Chapter VII. The necessary changes may include the boundary conditions (grinder's size, speeds, and gap width) and the mechanical parameters used in the breakage model. It is expected that the numerical results of product GSDs and grinding energy would benefit for optimising the design of various grinders. Similar modelling can be used to study other examples of comminution including grinding wheat, corn, and rice into a floury endosperm.

In Geotechnical Engineering, the solids may break under the high pressure at the bottom of rockfill dams (Alonso and Cardoso 2010). Using the breakage model, the dam's deformation can be studied by accounting for the influence of grain crushing. The evolving GSDs may be connected with granular's creep behavior in order to better predict the long-term deformation of the dam. In addition, the FE modelling of such a geotechnical problem with commercial software is relatively easy.

Studying the shallow foundation is another practical application for the breakage mechanics theory. Similar to pile end-bearing capacity, the resistance of shallow foundation is also affected by grain crushing (Poulos 1985). No existing studies examine the relationship between the bearing capacity of shallow foundation and soil crushability. Using the breakage mechanics theory and associated models, this topic can be explored by establishing appropriate FE models. The results of these models might be incorporated into upper bound or lower bound theory, such that a more rigorous and physical end-bearing equation can be derived for shallow foundations on brittle granular materials.

Anchors have been often used as a valid solution to secure offshore structures to the seabed (Andresen et al. 2008). The anchors may slide away when large quantities of

sediments around the tip of anchors break away. On such occasions, the study of grain crushing due to the anchors' penetration is of interest. This provides another application of the breakage mechanics theory. Using breakage models and FE modelling of the interaction between the anchor and brittle sediments may be useful for anchor design, to achieve the best holding effect.

A considerable amount of grain crushing would occur during the shearing process in landslides. This may generate high excess pore pressures and lower the pore-pressure dissipation rate (Okada et al. 2004). A subsequent disaster, which has been reported around the world, is the liquefaction failures of slopes. Therefore, modelling the grain crushing in various drained shearing conditions may be helpful to gain an appropriate understanding of the problems caused by landslides. In such a study, the breakage model for unsaturated granular material may be especially applicable.

References

ABAQUS/Explicit Users Manual, Version 6.10 (2010). Simulia.

Abbo, A. J., and Sloan, S. W. (1996). "An automatic load stepping algorithm with error control." *International Journal for Numerical Methods in Engineering*, 39, 1737-1759.

Abouzeid, A.-Z. M., and Fuerstenau, D. W. (2009). "Grinding of mineral mixtures in high-pressure grinding rolls." *International Journal of Mineral Processing*, Elsevier B.V., 93(1), 59-65.

Abouzeid, A.-Z.M., and Fuerstenau, D. W. (2000). "Mixture grinding in the high-pressure roller mill." *Proceedings of the XXI International Mineral Processing Congress*, Rome, Italy, A4-60-68.

Adler, P.M. (1988). "Transp. Fractal porous media III: Transversal Stokes flow through random and Sierpinski carpets." *Porous Media*, 3, 185.

Alawaji H, Runesson K, Sture S (1992). Implicit integration in soil plasticity under mixed control for drained and undrained response. *International Journal for Numerical and Analytical Methods in Geomechanics*, 16:737–756.

Al-Awquati, A. (1975). "On problems of soil bearing capacity at depth". Duke University.

Al-Awquati, Z., and Vesic, A. S. (1972). "Effect of lateral pressure on penetration resistance and bearing capacity of piles". *ASCE Annual meeting*, Houston.

Alba, J. L., and Audibert, J. M. E. (1999). "Pile design in calcareous and carbonaceous granular materials." *The second international conference on Engineering for calcareous sediments*, K. A. Al-Shafei, ed., Bahrein, pp. 29-43.

Altuhafi, F. N., and Coop, M. R. (2011). "Changes to particle characteristics associated with the compression of sands." *Géotechnique*, 61(6), 459-471.

Alyamani, M. S., and Şen, Z. (1993). "Determination of hydraulic conductivity from complete grain-size distribution curves." *Ground Water*. 31 (4) 551-555.

Alonso, E. E., and Cardoso, R. (2010). "Behavior of materials for earth and rockfill dams: Perspective from unsaturated soil mechanics." *Frontiers of Architecture and Civil Engineering in China*, 4(1), 1-39.

Angemeer, J., Carlson, E., and Klick, J. (1973). "Techniques and Results of Offshore Pile Load Testing In Calcareous Soils." *Proceedings of 5th Annual Offshore Technology Conference*, The Offshore Technology Conference, Houston, Texas, pp. 677–692.

Andresen, L., Jostad, H., and Andersen, K. (2008). "Finite Element Analyses in Offshore Foundation Design." *The 12th International Conference of International Association for Computer Methods and Advances in Geomechanics (IACMAG)*, Goa, India, pp. 1-6.

Arroyo, M., and Ortiz, M. (2006). "Localmaximum-entropy approximation schemes: a seamless bridge between finite elements and meshfree methods." *International Journal for Numerical Methods in Engineering*, 65(13), 2167-2202.

Austin, L. G. (1972). "A Review-Introduction to the mathematical description of grinding as a rate Process." *Powder Technology*, (5), 1-17.

Baligh, M. M. (1985). "Strain path method." *Journal of Soil Mechanics and Foundations Division*, 111(9), 1108–1136.

Baud, P., Klein, E., and Wong, T.-f. (2004). "Compaction localization in porous sandstones: Spatial evolution of damage and acoustic emission activity." *J. Struct. Geol.*, 26(4), 603 - 624, doi:10.1016/j.jsg.2003.09.002.

Benzer, H., Aydogan, N. a, and Dündar, H. (2011). "Investigation of the breakage of hard and soft components under high compression: HPGR application." *Minerals Engineering*, Elsevier Ltd, 24, 301-305.

Ben-Nun, O., and Einav, I. (2010). "The role of self-organisation during confined comminution of granular materials", *Phil. Trans. Roy. Soc. A*, 368, 231-247.

Bitra, V. S. P., Womac, A. R., Chevanan, N., Miu, P. I., Igathinathane, C., Sokhansanj, S., and Smith, D. R. (2009). "Direct mechanical energy measures of hammer mill comminution of switchgrass, wheat straw, and corn stover and analysis of their particle size distributions." *Powder Technology*, Elsevier B.V., 193(1), 32-45.

Borja, R. I., Lin, C.-H., and Montáns, F. J. (2001). "Cam-Clay plasticity, Part IV: Implicit integration of anisotropic bounding surface model with nonlinear hyperelasticity and ellipsoidal loading function." *Computer Methods in Applied Mechanics and Engineering*, 190(26-27), 3293-3323.

Borja, R. I. (1991). "Cam-Clay plasticity, Part II: Implicit integration of constitutive equation based on a nonlinear elastic stress predictor." *Computer Methods in Applied Mechanics and Engineering*, 88(2), 225-240.

Borja R.I., Tamagnini C. and Amorosi A. (1997), "*Coupling Plasticity and Energy-Conserving Elasticity Models for Clays.*" *Journal of Geotechnical and Geoenvironmental Engineering*, 123(10), 948-957

Bond, F. C. (1952). "The third theory of comminution." *Transactions of AIME Mining Engineering*, 193, 484-494.

Bopp, P. A., and Lade, P. V. (1997). "Effects of initial density on soil instability at high pressures." *Journal of geotechnical and geoenvironmental*, (July), 671-677.

Brown, J. H., Mitchell, S. R., and Weissman, M. (1960). "Energy-Size reduction relationship for the grinding of quartz." *Trans. AIME*, 217, 203-206.

Buscarnera, G., and Einav, I. (2012). "The yielding of brittle unsaturated granular soils." *Géotechnique*, 62(2), 147-160.

Burns, S. E., and Mayne, P. W. (1998). "Monotonic and dilatory pore-pressure decay during piezocone tests in clay." *Canadian Geotechnical Journal*, 35(6), 1063-1073.

Carrier, W. D. (2003). "Goodbye, Hazen; Hello, Kozeny-Carman." *Journal of Geotechnical and Geoenvironmental Engineering*, 129(11), 1054.

Carter, J. P., Randolph, M. F., and Wroth, C. P. (1979). "Stress and pore pressure changes in clay during and after the expansion of a cylindrical cavity." *International Journal for Numerical and Analytical Methods in Geomechanics*, 3(4), 305-322.

Campbell, G., Bunn, P. J., Webb, C., and Hook, S. C. W. (2001). "On predicting roller milling performance Part II. The breakage function." *Powder Technology*, 115(3), 243-255.

Charles, R. J. (1957). "Energy-size reduction relationships in comminution." *Transactions of AIME Mining Engineering*, 208, 80-88.

Cheng, Y. P., Bolton, M. D., and Nakata, Y. (2004). "Crushing and plastic deformation of soils simulated using DEM." *Géotechnique*, 54, 131-141.

Cleary, P. (2001) "Modelling comminution devices using DEM." *International Journal for Numerical and Analytical Methods in Geomechanics*, 25(1), 83-105.

Collins, I. F., and Houlsby, G. T. (1997). "Application of thermomechanical principles to the modelling of geotechnical materials." *Proceedings of the Royal Society. A: Mathematical, Physical and Engineering Sciences*, 453(1964), 1975-2001.

Collins, I. F., and Einav, I. (2005). "On the validity of elastic/plastic decompositions in soil mechanics." *Proceedings of the Symposium on Elastoplasticity*. Kyushu University, Japan, pp. 193–200.

Coop, M. R. (1990). "The mechanics of uncemented carbonate sands." *Géotechnique*, 40(4), 607-626.

Coop, M. R., Sorensen, K. K., Freitas, T. B., and Georgoutsos, G. (2004). "Particle breakage during shearing of a carbonate sand." *Géotechnique*, 54(3), 157-163.

Cortellazzo, G., and Simonini, P. (2001). "Permeability evaluation and its implications for consolidation analysis of an Italian soft clay deposit." *Canadian Geotechnical Journal*, 38(6), 1166-1176.

Crisfield, M. A. (1991). "Non-linear Finite Element Analysis of Solids and Structures." *John wiley & sons*, England.

Daphalapurkar, N. P., Lu, H., Coker, D., and Komanduri, R. (2007). "Simulation of dynamic crack growth using the generalized interpolation material point (GIMP) method." *International Journal of Fracture*, 143, 79-102.

Das, A., Nguyen, G. D., and Einav, I. (2011). "Compaction bands due to grain crushing in porous rocks: A theoretical approach based on breakage mechanics." *Journal of Geophysical Research*, 116(B8).

Datta, M., Gulhati, S. K., and Rao, G. V. (1980). "An appraisal of the existing practice of determining the axial capacit of deep penetration piles in calcareous soils." *Proc.12th annual OTC Conf*, Houston, Texas, Vol.4, pp. 119-130.

De, A. K. (1995). "Modeling and optimization of fine grinding of minerals in high-pressure roll mill-ball mill hybrid comminution circuits." University of California at Berkeley.

De Gennaro, V. and Frank, R. (2002). "Insight into the simulation of calibration chamber tests." *Proceedings of 5th European conference: Numerical Methods in Geotechnical Engineering*, Mestat, eds., pp. 169-177.

Dutkiewicz, R. K., Scieszka, S. F., and Fintel, R. H. von. (1986). "A study of the energy-size reduction relationship in impact crushing of coal." *Powder Technology*, 49(1), 83-86.

Durgunoglu, H. T., and Mitchell, J. K. (1975). "Static penetration resistance of soils: I. Analysis." *Proceedings of the Conference on In Situ Measurement of Soil Properties*, New York, pp. 151-171.

Dunne, F., and Petrinic, N. (2005). "Introduction to computational plasticity". Oxford University Press, USA.

Einav, I. (2002). "Applications of thermodynamical approaches to mechanics of soils." *PhD thesis*, Technion – Israel Institute of Technology, Haifa.

Einav, I. (2007a). "Breakage mechanics—Part I: Theory." *Journal of the Mechanics and Physics of Solids*, 55(6), 1274-1297.

Einav, I. (2007b). "Breakage mechanics—Part II: Modelling granular materials." *Journal of the Mechanics and Physics of Solids*, 55(6), 1298-1320.

Einav, I. (2007c). "Fracture propagation in brittle granular matter." *Proceedings of the Royal Society A: Mathematical, Physical and Engineering Sciences*, 463(2087), 3021-3035.

Einav, I. (2007d). "Soil mechanics: breaking ground." *Philosophical Transactions of the Royal Society. Series A, Mathematical, Physical, and Engineering Sciences*, 365(1861), 2985-3002.

Einav, I., and Puzrin, A. M. (2004). "Pressure-Dependent Elasticity and Energy Conservation in Elastoplastic Models for Soils." *Journal of Geotechnical and Geoenvironmental Engineering*, 130(1), 81.

Einav, I., and Randolph, M. F. (2005). "Combining upper bound and strain path methods for evaluating penetration resistance." *International Journal for Numerical Methods in Engineering*, 63(14), 1991-2016.

Einav, I., and Valdes, J. (2008). "On comminution and yield in brittle granular mixtures." *Journal of the Mechanics and Physics of Solids*, 56(6), 2136-2148.

Einav I., Vardoulakis I., and Chan A.H.C. (2011). "Confined comminution and permeability reduction in expanding perforations", to be provided upon request.

Emeriault, F., and Claquin, C. (2000). "Micromechanical modelling of the anisotropic viscoelasticity of granular materials: statistical homogenization." *Granular Matter*, 2(4), 201-210.

Emeriault, F. (2004). "Statistical homogenization for assemblies of elliptical grains: effect of the aspect ratio and particle orientation." *International Journal of Solids and Structures*. 41(21), 5837-5849.

Enderle, U., Kolb, G., Mende, S., Way, H. (2006). "effectively grinding and dispersing nanoparticles using a fine bead mill." NSTI-Nanotech, www.nsti.org, ISBN 0-9767985-6-5 Vol. 1, pp. 493-496.

Endra, S., and Roman, D. H. (2003). "Large displacement FEM modeling of the cone penetration test (CPT) in normally consolidated sand". *Int. J. Numer. Anal. Meth. Geomech.*, 27:585-602.

Epstein, B. (1949). "The mathematical description of certain breakage mechanisms leading to the logarithmico-normal distribution." *J. Franklin Inst*, 244, 471-477.

Farber, B. Y., Durant, B., and Bedesi, N. (2011). "Effect of media size and mechanical properties on milling efficiency and media consumption." *Minerals Engineering*, Elsevier Ltd.

Foray, P., Nauroy, J.-F., and Colliat, J.-L. (1999). "Mechanisms governing the behaviour of foundations in carbonate sands and design parameters from in situ tests." *The second international conference on Engineering for calcareous sediments*, K. A. Al-Shafei, ed., Barhein, pp. 55-68.

Francisco, J.V.P., Alberto, J.O.T., and Jose, A.R., (2009). "Validity of the permeability Carman- Kozeny equation: a volume averaging approach." *Phys. A* 388, 789-798.

Fuerstenau, D., Shukla, a, and Kapur, P. (1991). "Energy consumption and product size distributions in choke-fed, high-compression roll mills." *International Journal of Mineral Processing*, 32(1-2), 59-79.

Gens, A., and Potts, D. M. (1988). "Critical state models in computational geomechanics." *Engineering Computations*, 5(3), 178-197.

Gilvarry, J. J. (1961). "Fracture of brittle solids. I. distribution function for fragment size in single fracture (theoretical)." *Journal of Applied Physics*, 32(3), 391.

Gilvarry, J. J. (1964). "Distribution of fragment size in repetitive fracture of brittle solids." *Solid State Communications*, 2(1), 9-11.

Golightly, C. R., and Hyde, A. F. L. (1988). "Some fundamental properties of carbonate sands." *Proc., Int. Conf. on Calcareous Sediments*, Perth, Australia, pp. 173-184.

Gulhati, S. K., and Datta, M. (2005). *Geotechnical Engineering*, Tata McGraw-Hill Education.

Hagerty, M. M., Hite, D. R., Ullrich, C. R., and Hagerty, D. J. (1993). "One-dimensional high pressure compression of granular materials." *ASCE J. Geotech. Engng*, 119(1), 1-18.

Haque, E. (1991). "Application of size reduction theory to roller mill design and operation." *Cereal food world*, 36, 368-375.

Hardin, B.O. (1985). "Crushing of soil particles." *Journal of Geotechnical Engineering*, 111(10), 1177-1192.

Hardin, B. O., and Black, W. L. (1966). "Sand stiffness under various triaxial stresses". *J. Soil Mech. Found. Engng., ASCE*, 92, 27–42.

Harireche, O., and Mcdowell, G. R. (2002). "Discrete element modelling of yielding and normal compression of sand." *Géotechnique*, 52(4), 299-304.

Hazen, A. (1892). "Some physical properties of sands and gravels, with special reference to their use in filtration." *24th Annual Rep., Massachusetts State Board of Health*, No. 34, pp. 539–556.

Houlsby G.T. (1985), "The use of a variable shear modulus in elastic-plastic models for clays." *Computers and Geotechnics*, 1(1), 3-13.

Houlsby G.T., Amorosi A. and Rojas E. (2005), "*Elastic moduli of soils dependent on pressure: a hyperelastic formulation.*" *Géotechnique*, 55(5), 383–392.

Houlsby, G. T., and Puzrin, A. M. (2000). "A thermomechanical framework for constitutive models for rate-independent dissipative materials." *International Journal of Plasticity*, 16, 1017-1047.

Hukki, R. T. (1962). "Proposal for a solomonic settlement between the theories of von Rittinger, Kick, and Bond." *Trans. AIME*, 223, 403-408.

Hyodo, M., Aramaki, N., Itoh, M., and Hyde, A. F.L. (1996). "Cyclic strength and deformation of crushable carbonate sand." *Soil Dynamics and Earthquake Engineering*, 15(5), 331-336.

Indraratna, B., and Salim, W. (2002). "Modelling of particle breakage of coarse aggregates incorporating strength and dilatancy." *Geotechnical Engineering*, 155(4), 243-252.

Jeremić, B., and Sture, S. (1997). "Implicit integrations in elastoplastic geotechnics." *Mechanics of Cohesive-frictional Materials*, 2(2), 165-183.

Joer, H. A., Jewell, R. J., and Randolph, M. F. (1999). "Cone penetrometer testing in calcareous sediments." *Second International Conference on Calcareous Sediments*, K. A. Al-Shafei, ed., Bahrein, pp. 243-252.

Kapur, P. (1971). "The energy-size reduction relationships in comminution of solids." *Chemical Engineering Science*, 26(1), 11-16.

Kapur, P. (1990). "Energy-size relationship for breakage of single particles in a rigidly mounted roll mill." *International Journal of Mineral Processing*, 29(3-4), 221-233.

Kapur, P., and Fuerstenau, D. (1987). "Energy-size reduction 'laws' revisited." *International Journal of Mineral Processing*, 20(1-2), 45-57.

Kendall, K. (1978). "The impossibility of comminuting small particles by compression." *Nature*, 272(5655), 710-711.

Kick, F. (1885). "Das Gezetz der proportionalen Winderstande und seine Anwendung." Arthur Felix, Leipzig.

Klemm, A., Kimmich, R., Weber, M. (2001). "Flow through percolation clusters: NMR velocity mapping and numerical simulation study." *Phys. Rev. E*, 63, 041514.

Klotz, E. U., and Coop, M. R. (2001). "An investigation of the effect of soil state on the capacity of driven piles in sands." *Géotechnique*, 51(9), 733-751.

Kuwajima, K., Hyodo, Masayuki, and Hyde, Adrian F. L. (2009). "Pile bearing capacity factors and soil crushabiity." *Journal of Geotechnical and Geoenvironmental Engineering*, 135(7), 901-913.

Lade, P. V., Yamamuro, J. A., and Bopp, P. A. (1996). "Significance of particle crushing in granular materials." *Journal of Geotechnical Engineering*, 122(4), 309-316.

Li, G. B., and Xu, X. H. (1992). "Experimental investigation of the energy-size reduction relationship in comminution using fractal theory." *Minerals Engineering*, 6(2), 163-172.

Liu, G. R. (2010). "A G space theory and a weakened weak (W2) form for a unified formulation of compatible and incompatible methods: Part I theory and Part II applications to solid mechanics problems." *International Journal for Numerical Methods in Engineering*, 81, 1093-1126.

Luccioni, L. X., Pestana, J. M., and Taylor, R. L. (2001). "Finite element implementation of non-linear elastoplastic constitutive laws using local and global explicit algorithms with automatic error control." *International Journal for Numerical Methods in Engineering*, 50(5), 1191-1212.

Matyka, M., Khalili, A., and Koza, Z. (2008). "Tortuosity–porosity relation in the porous media flow." *Physical Review E*, 78, 1-8.

McClelland, B. (1974). "Design of deep penetration piles for ocean structures." *ASCE J.Geotech. Eng*, Div. 100(GT7), pp. 705–747.

McClelland, B. (1988). "Calcareous sediments: an engineering enigma." *Proc, Int. Cong. On Calcareous Sediments*, pp. 777–784.

McDowell, G. R., and Bolton, M. D. (1997). "A micro-mechanical model for over-consolidated behaviour in soils." *Proceedings 3rd International Conference on Powders and Grains*, Behringer R.P. and Jenkins J.T., ed., Balkema, Rotterdam, pp. 203-206.

McDowell, G. R., and Bolton, M. D. (1998). "On the micromechanics of crushable aggregates." *Géotechnique*, 48(5), 667-679.

McDowell, G. R., and Bolton, M. D. (1999). "A micro mechanical model for isotropic cyclic loading of isotropically clastically compressed soil." *Granular Matter*, 1(4), 183-193.

McDowell, G. R., and Bolton, M. D. (2000). "Effect of particle size distribution on pile tip resistance in calcareous sand in the geotechnical centrifuge." *Granular Matter*, 2(4), 179-187.

McDowell, G. R., Bolton, M, D., and Robertson, D. (1996). "The fractal crushing of granular materials." *Journal of the Mechanics and Physics of Solids*, 44(12), 2079-2101.

McDowell, G. R., and Daniell, C. M. (2001). "Fractal compression of soil." *Géotechnique*, 51(2), 173-176.

Meyerhof, G. G. (1963). "Some recent research on the bearing capacity of foundations." *Canadian Geotechnical Journal*, 1(1), 16-26.

Miura, N., and O-hara, S. (1979). "Particle crushing of a decomposed granite soil under shear stress." *Soils Found*, 19(3), 1-14.

Mooney, M. A., Finno, R. J., and Viggiani, G. (1998). "A unique critical state for sand?" *Journal of Geotechnical and Geoenvironmental Engineering*, 124, 1100-1108.

Morrell, S. (2004). "An alternative energy-size relationship to that proposed by Bond for the design and optimisation of grinding circuits." *International Journal of Mineral Processing*, 74, 133-141.

Morrell, S. (2006). "Rock characterisation for high pressure grinding rolls circuit design." *Proc International Autogenous and Semi Autogenous Grinding Technology*, Vancouver, vol IV, pp. 267-278.

Morrell, S. (2010). "Predicting the specific energy required for size reduction of relatively coarse feeds in conventional crushers and high pressure grinding rolls." *Minerals Engineering*, Elsevier Ltd, 23(2), 151-153.

Nakata, Y., Hyodo, M., Hyde, A. F. L., Kato, Y., and Murata, H. (2001). "Microscopic particle crushing of sand subjected to high-pressure one-dimensional compression." *Soils Found*, 41(1), 69–82.

Nakata, Y., Kato, Y., Hyodo, M., Murata, H., and Hyde, A. F. L. (1999). "Single particle crushing and the mechanical behaviour of sand." *Proc. 2nd Int. Symp. on Pre-Failure Deformation Characteristics of Geomaterials*, Torino, pp. 221–228.

Nguyen, G. D., and Einav, I. (2009). "The energetics of cataclasis based on breakage mechanics." *Pure and Applied Geophysics*, 166, 1693–1724.

Needleman, A. (1988). "Material rate dependence and mesh sensitivity in localization problems." *Computer Methods in Applied Mechanics and Engineering*, 67(1), 69-85.

Netuzhylov, H., and Zilian, A. (2009). "Space-time meshfree collocation method: Methodology and application to initial-boundary value problems." *International Journal for Numerical Methods in Engineering*, 80(3), 355-380.

Nutt, N.R.F. and Houlsby, G. T. (1991). "Calibration Tests on the Cone Pressuremeter in Carbonate Sand.pdf." *Proceedings of the First International Conference on Calibration Testing*, New York, pp. 265-276.

Ohno, S., Ochia, H., and Yasufuku, N. (1999). "Estimation of pile settlement in calcareou sands." *Engineering for Calcareous Sediments*, Al-Shafei, ed., Balkema, Rotterdam, pp.1-6.

Okada, Y., Sassa, K., and Fukuoka, H. (2000). "Liquefaction and the steady state of weathered granitic sands obtained by undrained ring shear tests: a fundamental study of the mechanism of liquidized landslides." *Journal of natural disaster science*, 22(2), 75–85.

Okada, Y., Sassa, K., and Fukuoka, H. (2004). "Excess pore pressure and grain crushing of sands by means of undrained and naturally drained ring-shear tests." *Engineering Geology*, 75(3-4), 325-343.

Papamichos, E., Vardoulakis, I., and Ouadfel, H. (1993). "Permeability reduction due to grain crushing around a perforation." *International Journal of Rock Mechanics and Mining Sciences & Geomechanics Abstracts*, 30(7), 1223-1229.

Palmer, A. C., and Sanderson, T. J. O. (1991). "Fractal Crushing of Ice and Brittle Solids." *Proceedings of the Royal Society A: Mathematical, Physical and Engineering Sciences*, 433(1889), 469-477.

Perzyna, P. (1963). "The constitutive equations for rate sensitive plastic materials." *Quart. Appl. Mech.*, 20, 321-332.

Perzyna, P. (1966). "Fundamental problems in visco-plasticity." *Advan. Appl. Mech*, 9, 243-377.

Posner, E. S., and Hibbs, A. N. (1997). *Wheat flour milling*. American Association of Cereal Chemistry, Inc., St. Paul, Minnesota, USA.

Poulos, H. G. (1985). "Foundation problems in marine calcareous sands." *Proc. Int. Symp. on Ocean Space Utilization*, Tokyo, pp.485-495.

Poulos, H. G., and Chua, E. W. (1985). "Bearing capacity of foundations on calcareous sand." *11th International Conference on Soil Mechanics and Foundation Engineering*, San Francisco,Calif., Vol. 3, pp. 1619-1622.

Poulos, H. G. (1989). "The Mechanics of Calcareous Sediments." John Jaeger Memorial Lecture. *Aust. Geomechanics*, Special Ed, 8-41.

Prandtl, L. (1921). "Uber die eindrigungsfestigkeit plastischer baustroffe and die festigkeit von schneiden." *Zeitschrift für Angewandte Mathematik und Mechanik (ZAMM)*, 1(1), 15-20.

Prasher, C. (1987). *Crushing and grinding process handbook.* John Wiley, New York., pp. 474.

Purushothama Raj, P. (2007). *Soil Mechanics & Foundation Engineering*, Pearson Education India., pp. 110.

Ramkrishna, D. (2000). *Population balances. Theory and applications to particulate systems in engineering.* Academic Press, San Diego.

Randolph, M. F. (1988). "The axial capacity of deep foundations in calcareous soil." *Engineering for calcareous sediments*, Rotterdam, pp.837-857.

Rittinger, P. R. (1867). *Lehrbuch der Aufbereitungskunde.* 1st edition, Verlag von Ernst & Korn, Berlin.

Robertson, P. K., Sully, J. P., Woeller, D. J., Lunne, T., Powell, J. J. M., and Gillespie, D. G. (1992). "Estimating coefficient of consolidation from piezocone tests." *Canadian Geotechnical Journal*, 29(4), 539-550.

Rubin, M. B., and Einav, I. (2011). "A large deformation breakage model of granular materials including porosity and inelastic distortional deformation rate." *International Journal of Engineering Science*. 49(10), 1151-1169.

Russell, A. R. (2011). "A compression line for soils with evolving particle and pore size distributions due to particle crushing." *Géotechnique Letters*, 1(January-March), 5-9.

Russell, A. R., and Khalili, N. (2002). "Drained cavity expansion in sands exhibiting particle crushing." *International Journal for Numerical and Analytical Methods in Geomechanics*, 26(4), 323-340.

Sammis, C. G., Osborne, R. H., Anderson, J. L., Banerdt, M., and White, P. (1986). "Self-similar cataclasis in the formation of fault gouge." *Pure Appl. Geophys*, 124(1), 53–78.

Sammis, C. G., King, G., and Biegel, R. L. (1987). "The kinematics of gouge deformation." *Pure Appl. Geophys*, 125, 777-812.

Sammis, C. G., and King, G. C. P. (2007). "Mechanical origin of power law scaling in fault zone rock." *Geophysical Research Letters*, Vol. 34, L04312.

Sander, U. (1999). "Operational conditions of a screw-feeder-equipped high-pressure roller mill." *Powder Technology*, 105(1-3), 282-287.

Sassa, K., Fukuoka, H., Scarascia-Mugnozza, G., and Evans, S. (1996). "Earthquake-induced-landslides: distribution, motion and mechanisms." *Soils and Foundations*, (Special Issue for the great Hanshin Earthquake Disasters), 53-64.

Schönert, K. (1988). "A first survey of grinding with high-compression roller mills." *International Journal of Mineral Processing*, (22), 401-408.

Seebach, M. E. (1987). "High-pressure grinding rolls in industrial applications." *Aufbereitungs technik*, 28(10), 591-599.

Semple, R. M. (1988). "Mechanical properties of calcareous soils: state of the art report." *Engineering for calcareous sediments*, Rotterdam, 807-836.

Shepherd, R. G. (1989). "Correlations of Permeability and Grain Size." *Ground Water*, 27(5), 633-638.

Sheng, D. C., Sloan, S. W., and Yu, H. S. (2000). "Aspects of finite element implementation of critical state models." *Computational Mechanics*, 26(2), 185-196.

Sheng, D. C., and Sloan, S. W. (2001). "Load stepping schemes for critical state models." *International Journal for Numerical Methods in Engineering*, 50(1), 67-93.

Sheng, D. C., Eigenbrod, K., and Wriggers, P. (2005). "Finite element analysis of pile installation using large-slip frictional contact." *Computers and Geotechnics*, 32(1), 17-26.

Simo, J. C. (1989). "Strain softening and dissipation: a unification of approaches." *Cracking and damage: strain localization and size effect*, J. Mazara and Z. P. Bazant, eds., Elsevier Applied Science, London, 440-461.

Simo, J. C., and Taylor, R. L. (1985). "Consistent tangent operators for rate-independent elasto-plasticity." *Computer Methods in Applied Mechanics and Engineering*, 48, 10-118.

Simo, J. C., and Hughes, T. J. R. (1997). "*Computational Inelasticity*". Springer, New York.

Simo J. C. (1998). "Numerical Analysis and Simulation of Plasticity". *Vol. VI of Handbook of Numerical Analysis*. Elsevier Science: Amsterdam. 183-499.

Sloan, S. W. (1987). "Substepping schemes for the numerical integration of elastoplastic stress-strain relations." *International Journal for Numerical Methods in Engineering*, 24(5), 893-911.

Sloan, S. W., Abbo, A. J., and Sheng, D. C. (2001). "Refined explicit integration of elastoplastic models with automatic error control." *Engineering Computations*, 18(1/2), 121-194.

Sperry, J. M., and Peirce, J. J. (1995). "A model for estimating the hydraulic conductivity of granular material based on grain shape, grain size, and porosity." *Ground Water*, 33(6), 892-898.

Stamboliadis, E. T. (2002). "A contribution to the relationship of energy and particle size in the comminution of brittle particulate materials." *Minerals Engineering*, 15(10), 707-713.

Stamboliadis, E. T. (2004). "Energy distribution in comminution, a new approach to the laws of Rittinger, Bond and Kick." *Canadian Metallurgical Quarterly*, 43(2), 249-258.

Stamboliadis, E. T. (2007). "The energy distribution theory of comminution specific surface energy, mill efficiency and distribution mode." *Minerals Engineering*, 20(2), 140-145.

Stamboliadis, E. T. (2005). "The fracture of brittle materials as an equilibrium of surface and cohesion energy." *Journal of the Mechanical Behavior of Materials*, 16(6), 363-377.

Stanley, H.E., and Andrade Jr., J.S. (2001). "Physics of cigarette filter:fluid flow through structures with randomly-placed obstacles." *Phys. A*, 95, 17.

Sully, J. P., Robertson, P. K., Campanella, R. G., and Woeller, D. J. (1999). "An approach to evaluation of field CPTU dissipation data in overconsolidated fine-grained soils." *Canadian Geotechnical Journal*, 36(2), 369-381.

Sulsky, D., Chen, Z., and Schreyer, H. L. (1994). "A particle method for history-dependent materials." *Computer Methods in Applied Mechanics and Engineering*, 118, 179-196.

Tamagnini, C., Castellanza, R., and Nova, R. (2002). "A Generalized Backward Euler algorithm for the numerical integration of an isotropic hardening elastoplastic model for mechanical and chemical degradation of bonded geomaterials." *International Journal for Numerical and Analytical Methods in Geomechanics*, 26(10), 963-1004.

Tavares, L. M., and King, R. P. (1998). "Simple-particle fracture under impact loading." *International Journal of Mineral Processing*, 54(1), 1-28.

Tarantino A. (2010). "Basic concepts in the mechanics and hydraulics of unsaturated geomaterials". *Mechanics of Unsaturated Geomaterials*, Ed. Laloui L., Wiley, pp. 3-28.

Teh, C. I., and Houlsby, G. T. (1988). "Analysis of the cone penetration test by the strain path method." *In Proceedings of the 6th International Conference on Numerical Methods in Geomechanics*, Innsbruck, pp. 398-402.

Torstensson, B.-A. (1977). "The pore pressure probe." *In Geotechnical Meeting, Norwegian Geotechnical Society*, Oslo, Norway., pp.34.1-34.15.

Terzaghi, K. (1943). *Theoretical soil mechanics*. Wiley, New York.

Tsoungui, O., Vallet, D., and Charmet, J.-C. (1999). "Numerical model of crushing of grains inside two-dimensional granular materials." *Powder Technology*, 105(1-3), 190-198.

Turcotte. D.L. (1986). "Fractals and fragmentation." *J. Geophys*, Res. 91, 1921-1926.

Ueng, T.-S., and Chen, T.-J. (2000). "Energy aspects of particle breakage in drained shear of sands." *Géotechnique*, 50(1), 65-72.

Valdes, J. R., and Carlos Santamarina, J. (2007). "Particle transport in a nonuniform flow field: Retardation and clogging." *Applied Physics Letters*, 90(24), 244101-1-244101-03.

Vesic, A. S. (1973). "Analysis of ultimate loads of shallow foundations." *International Journal of Rock Mechanics and Mining Sciences & Geomechanics Abstracts*, 11(4), 45-73.

Vesic, A. S. (1977). *Design of pile foundations*. Duke University Press, New York.

Vesic, A. S. (1975). "Principle of pile foundation design." *Soil mechanics series No. 38*, School of Engineering, Duke university, Hurham, NC.

Vesic, A. S., and Clough, G. W. (1968). "Behaviour of granular materials under high stresses." *ASCE J. Soil Mech. Found. Div.*, 94(3), 661–688.

Viggiani, G., & Atkinson, J. H. (1995). "Stiffness of fine-grained soils at very small strains." *Géotechnique*, 45(2), 249–265.

Website 1. (2011). http://chrisvonada.com/category/breathing-life/page/10/

Website 2. (2011). http://www.fotothing.com/ rescue193uk/photo/

Website 3. (2011). http://yufmachine.com/113.html

Website 4. (2011). http://www.german-oilgas-expo.com/e-news-eon-wind.htm

Website 5. (2011). http://www.alaska-in-pictures.com/monopod-oil-platform-3221-pictures.htm

Website 6. (2012). http://www.ceramicindustry.com/articles/print/92186

Walker, D. R., and Shaw, M. C. (1954). "A physical explanation of the empirical laws of comminution." *AIME Trans*, 199, 313-320.

Walsh, S.D.C., and Tordesillas, A. (2004). "A thermomechanical approach to the development of micropolar constitutive models for granular media."*Acta Mechanica*.167 (3-4), 145–169.

Wang, F. W., and Sassa, K. (2000). "Relationship between grain crushing and excess pore pressure generation by sandy soils in ring shear tests." *Journal of Natural Disaster Science*, 22(2), 87–96.

White, D. J., and Bolton, M. D. (2004). "Displacement and strain paths during plane-strain model pile installation in sand." *Géotechnique*, 54(6), 375-397.

Yang, Z. X., Zhu, B. T., Jardine, R. J., Tsuha, C. H. C., and Foray, P. (2010). "Sand grain crushing and interface shearing during displacement pile installation in sand." *Géotechnique*, 60(6), 469-482.

Yamamuro, J. A., and Lade, P. V. (1998). "Steady-state concepts and static liquefaction of silty sands." *Journal of Geotechnical and Geoenvironmental Engineering*, 124, 868-877.

Yasufuku, N., and Hyde, A. F. L. (1995). "Pile end-bearing capacity in crushable sands." *Géotechnique*, 45(4), 663-676.

Yeung, S. K., and Carter, J. P. (1989). "An assessment of the bearing capacity of calcareous and silica sands." *International Journal for Numerical and Analytical Methods in Geomechanics*, 13(1), 19-36.

Yu, H.-S. (2000). *Cavity expansion methods in geomechanics*. Kluwer Academic Pulishers, Netherlands, 298.

Zhang, C. S., Nguyen, G. D., and Einav, I. (2012). "The end bearing capacity of piles penetrating into crushable soils." *Géotechnique*, in revision.

Zhang, C.S., Einav, I and Nguyen, G. D. (2011). "A study of grain crushing around penetrating piles using a micromechanics-based continuum model". *The Second International Symposium on Computational Geomechanics (ComGeo II)*, Pietruszczak and Pande eds., Cavtat-Dubrovnik, pp. 714-720.

Zhang, C.S., Nguyen, G. D., and Einav, I. (2010). "Steady state permeability profiles surrounding penetrating piles in crushable granular media." *Proceedings of the international symposium on Geomechanics and Geotechnics: From Micro to Macro*, Jiang et al., eds., Shanghai, pp. 789-795.

Zhao, J. D., Sheng, D. C., Rouainia, M., and Sloan, S. W. (2005). "Explicit stress integration of complex soil models." *International Journal for Numerical and Analytical Methods in Geomechanics*, 29(12), 1209-1229.

Zhu, W. L., and Wong, T. F. (1997). "The transition from brittle faulting to cataclasitic flow: Permeability evolution." *Journal of Geophysical Research*, 102(B2), 3027-3041.

Ziegler, H. (1977). "*An introduction to thermodynamics*." North-Holland Publishing Co., Amsterdam.

Zytynski M., Randolph, M. F., Nova, R. and Wroth, C. P. (1978). "On modelling the unloading-reloading behaviour of soils." *Int. J. Numer. Anal. Methods Geomech.* 2, 87–93.

Appendix A

```
      Subroutine vumat(
C Read only -
     1 nblock, ndir, nshr, nstatev, nfieldv, nprops, lanneal,
     2 stepTime, totalTime, dt, cmname, coordMp, charLength,
     3 props, density, strainInc, relSpinInc,
     4 tempOld, stretchOld, defgradOld, fieldOld,
     3 stressOld, stateOld, enerInternOld, enerInelasOld,
     6 tempNew, stretchNew, defgradNew, fieldNew,
C Write only -
     5 stressNew, stateNew, enerInternNew, enerInelasNew )
C
      include 'vaba_param.inc'
C All arrays dimensioned by (*) are not used in this algorithm
      dimension props(nprops), density(nblock),
     1 coordMp(nblock,*),
     2 charLength(*), strainInc(nblock,ndir+nshr),
     3 relSpinInc(*), tempOld(*),
     4 stretchOld(*), defgradOld(*),
     5 fieldOld(*), stressOld(nblock,ndir+nshr),
     6 stateOld(nblock,nstatev), enerInternOld(nblock),
     7 enerInelasOld(nblock), tempNew(*),
     8 stretchNew(*), defgradNew(*), fieldNew(*),
     9 stressNew(nblock,ndir+nshr), stateNew(nblock,nstatev),
     1 enerInternNew(nblock), enerInelasNew(nblock)
C
      character*80 cmname
           dimension ds(6),delta(6), D(6,6),sig(6),dptridsigmatri(6),
     1          dqtridsigmatri(6),dystardsigmatri(6),Ttri(6),
     2         dstress(6),MatrixP(6,6),MatrixPinv(6,6),
          3         DevEpsPls(6),epsPls(6),depsPls(6),difgsd(16),
          4         dstrainInc(6),strain(6),gsd0(16),gsd(16),gsdU(16)
           integer k1,k2,k3,i,kk
           real theta,K,G,M,Pc,Ec,Omega,xnu,E,alamda,void0,voidmax,en0,n0,
     1     nmax,nchange,B,dp,dq,p,q,ptri,qtri,ytri,Ebtri,epsEv,epsEs,
     2     epsV,espS,epsEvtri,epsEstri,epsPv,epsPs,alfa,belta,
     3     dytridEbtri,dEbtridB,dEbtridptri,dEbtridqtri,n,depsPv,
     4     dytridptri,dytridqtri,dytridB,dystardEbtri,dystardptri,
     5     dystardqtri,H2,H3,H4,Utri,dL,dB,Rd,Rk,dvoid,void,DH0,DHu,
     6     DH,T0,T,Bmarsal,Rk1,Rk2,Rk3
           parameter ( pi=3.141592653589793)
c
c Input Breakage model parameters
          theta=0.2
          G=14500e3
          K=17800e3
```

```
          M=1.78
          Ec =2e3
c         Pc=sqrt(2.0*K*Ec/theta)
          pc=1300e3
c         Ec=theta*Pc**2.0/(2.0*K)
          omega=30.0*pi/180.0
c Input Elastic parameters
          xnu=(3.0*K-2.0*G)/(6.0*K+2.0*G)
          E=2.0*G*(1.0+xnu)
          alamda=2.0*G*(E-2.0*G)/(6.0*G-2.0*E)
c Define kroneck Matrix and after vectorization
          delta(1:ndir)=1.0
          delta(4)=0.0
          delta(5)=0.0
          delta(6)=0.0
c Define elastic modulus matrix D
     D(1:6, 1:6) = 0.0
          do k1=1,ndir
            do k2=1,ndir
              D(k2,k1)=aLamda
            end do
              D(k1,k1)=2.0*G+aLamda
          end do
          do k3=ndir+1,6
       D(k3,k3)=2*G
          end do
c
     Do K1=1,ndir
           MatrixP(k1,k1)=1.0
           MatrixPinv(k1,k1) = 1.0
          End do
          Do k2=ndir+1, 6
           MatrixP(k2,k2)=2.0
           MatrixPinv(k2,k2) = 0.5
          End do
c-----------------------------------------------------------------
c
     if (stepTime.eq.0) then
          do i=1,nblock
       trace=strainInc(i,1)+strainInc(i,2)+strainInc(i,3)
       stressNew(i,1)=stressold(i,1)+
     *      (1-theta*B)*(2*G*strainInc(i,1)+alamda*trace)
          stressNew(i,2)=stressold(i,2)+
     *      (1-theta*B)*(2*G*strainInc(i,2)+alamda*trace)
          stressNew(i,3)=stressold(i,3)+
     *      (1-theta*B)*(2*G*strainInc(i,3)+alamda*trace)
          stressNew(i,4)=stressold(i,4)+(1-theta*B)*(2*G*strainInc(i,4))
            if (nshr.GE.2) then
       stressNew(i,5)=stressold(i,5)+(1-theta*B)*(2*G*strainInc(i,5))
```

```
      stressNew(i,6)=stressold(i,6)+(1-theta*B)*(2*G*strainInc(i,6))
            end if
    end do
c
        else
c
    do 100 i=1, nblock
          p=STATEOLD(i,1)
          q=STATEOLD(i,2)
          epsV=STATEOLD(i,3)
          epsS=STATEOLD(i,4)
          B=STATEOLD(i,5)
          ytri=STATEOLD(i,6)
          epsPv=STATEOLD(i,7)
          epsPs=STATEOLD(i,8)
          epsEv=STATEOLD(i,9)
          epsEs=STATEOLD(i,10)
          epsPls(1)=STATEOLD(i,11)
          epsPls(2)=STATEOLD(i,12)
          epsPls(3)=STATEOLD(i,13)
          epsPls(4)=STATEOLD(i,14)
c Trial stress
      trace=strainInc(i,1)+strainInc(i,2)+strainInc(i,3)
      sig(1)=stressold(i,1)+
     *      (1-theta*B)*(2*G*strainInc(i,1)+alamda*trace)
          sig(2)=stressold(i,2)+
     *      (1-theta*B)*(2*G*strainInc(i,2)+alamda*trace)
          sig(3)=stressold(i,3)+
     *      (1-theta*B)*(2*G*strainInc(i,3)+alamda*trace)
          sig(4)=stressold(i,4)+(1-theta*B)*(2*G*strainInc(i,4))
           if (nshr.GE.2) then
      sig(5)=stressold(i,5)+(1-theta*B)*(2*G*strainInc(i,5))
      sig(6)=stressold(i,6)+(1-theta*B)*(2*G*strainInc(i,6))
            end if
c
          epsV=epsV+(-trace)  !!
          epsS=epsS+sqrt((2.0/3.0)*((strainInc(i,1)-trace/3.0)**2.0
     *              +(strainInc(i,2)-trace/3.0)**2.0
     *             +(strainInc(i,3)-trace/3.0)**2.0
     *             +2*strainInc(i,4)**2.0))
     *             +2*strainInc(i,5)**2.0
     *             +2*strainInc(i,6)**2.0))
c
        epsEvtri=epsV-epsPv
        epsEstri=epsS-epsPs
c
         ptri=-(sig(1)+sig(2)+sig(3))/3 !!
c deviatoric stresses
          ds(1)=sig(1)-(sig(1)+sig(2)+sig(3))/3
```

```
            ds(2)=sig(2)-(sig(1)+sig(2)+sig(3))/3
            ds(3)=sig(3)-(sig(1)+sig(2)+sig(3))/3
            ds(4)=sig(4)
            if (nshr.GE.2) then
            ds(5)=sig(5)
            ds(6)=sig(6)
            end if
c
            qtri=sqrt(1.5*(ds(1)**2+ds(2)**2+ds(3)**2
     *      +2*ds(4)**2+2*ds(5)**2+2*ds(6)**2))
            Ebtri=theta*(ptri**2/K+qtri**2/(3*G))/(2*(1-B*theta)**2)
            ytri=Ebtri*(1-B)**2/Ec+(qtri/(M*ptri))**2-1
c
            if (ytri. LT.0) then
c Elastic update
           stressNew(i,1)=sig(1)
           stressNew(i,2)=sig(2)
            stressNew(i,3)=sig(3)
            stressNew(i,4)=sig(4)
            stressNew(i,5)=sig(5)
            stressNew(i,6)=sig(6)
            p=ptri
            q=qtri
            epsEv=epsEvtri
            epsEs=epsEstri
            B=B
            EpsPls=EpsPls
c
        else
c Plastic/Breakage calculation
c
            dytridEbtri=((1-B)**2)/Ec
            dEbtridB=(theta**2*(ptri**2/K+qtri**2/(3*G)))/((1-theta*B)**3)
           dEbtridptri=(ptri*theta)/(K*(1-theta*B)**2)
            dEbtridqtri=(qtri*theta)/(3*G*(1-theta*B)**2)
            dptridsigmatri(1:6)=-delta(1:6)/3 !!!
c
        if (qtri==0.0) then
            dqtridsigmatri=0.0
            else
            dqtridsigmatri=1.5*matmul(MatrixP,ds)/qtri
        end if
c
        dytridptri=(-2*qtri**2)/(M**2*ptri**3)
            dytridqtri=(2*qtri)/((M*ptri)**2)
            dytridB=(-2*Ebtri*(1-B))/Ec
            dystardEbtri=2*((1-B)**2)*(cos(omega))**2/Ec
            dystardptri=2*((1-B)**2*Ebtri)*(sin(omega))**2/(ptri*Ec)
            dystardqtri=(2*qtri)/((M*ptri)**2)
```

```
c
        dystardsigmatri(1:6)=dystardptri*dptridsigmatri(1:6)
     *                  +dystardqtri*dqtridsigmatri(1:6)
c
c Obtain Ttrial and Utrial
        Ttri=(dytridEbtri*dEbtridptri+dytridptri)*dptridsigmatri
     *          +(dytridEbtri*dEbtridqtri+dytridqtri)*dqtridsigmatri
c
        H2=dot_product(Ttri,(1.0-theta*B)*matmul(D,dystardsigmatri))
        H3=dytridB+dytridEbtri*dEbtridB
        H4=(theta/(1.0-theta*B))*dot_product(Ttri,matmul(MatrixP,sig))
c
        Utri=H2-(H3-H4)*dystardEbtri
        dL=ytri/Utri
c  Update plastic/breakage stress and strain increments
        dB=dL*dystardEbtri
        depsPls(1:6)=dL*dystardsigmatri(1:6)
        dstress(1:6)=-(1.0-theta*B)*matmul(D,depsPls)
     *                  -theta*(sig/(1.0-theta*B))*dB
c
        epsPls(1:6)=epsPls(1:6)+depsPls(1:6)
        epsPv = -sum(epsPls(1:Ndir))
        DevEpsPls(1:6)=epsPls(1:6)- sum(epsPls(1:Ndir))*delta/3.0
        epsPs = sqrt((2.0/3.0)*dot_product(DevEpsPls,
     *  matmul(MatrixP,DevEpsPls)))
c
        epsEv=epsV-epsPv
        epsEs=epsS-epsPs
c
        stressNew(i,1)=sig(1)+dstress(1)
        stressNew(i,2)=sig(2)+dstress(2)
        stressNew(i,3)=sig(3)+dstress(3)
        stressNew(i,4)=sig(4)+dstress(4)
        stressNew(i,5)=sig(5)+dstress(5)
        stressNew(i,6)=sig(6)+dstress(6)
        B=B+dB
c
        dp=-sum(dstress(1:Ndir))/3
        dq=sqrt(1.5*((dstress(1)+dp)**2
     *          +(dstress(2)+dp)**2
     *          +(dstress(3)+dp)**2
     *          +2*(dstress(4)**2
     *          +dstress(5)**2+dstress(6)**2)))
c
         p=-(stressNew(i,1)+stressNew(i,2)+stressNew(i,3))/3.0  !! Sign convention
        ds(1)=stressNew(i,1)-(stressNew(i,1)+stressNew(i,2)+stressNew(i,3))/3.0
        ds(2)=stressNew(i,2)-(stressNew(i,1)+stressNew(i,2)+stressNew(i,3))/3.0
        ds(3)=stressNew(i,3) -(stressNew(i,1)+stressNew(i,2)+stressNew(i,3))/3.0
        ds(4)=stressNew(i,4)
```

```
            ds(5)=stressNew(i,5)
            ds(6)=stressNew(i,6)
            q=sqrt(1.5*(ds(1)**2+ds(2)**2+ds(3)**2+2*ds(4)**2
     *           +2*ds(5)**2+2*ds(6)**2))
c
          End if
c Displaying in abaqus
            STATENEW(i,1)=P
            STATENEW(i,2)=q
            STATENEW(i,3)=epsV
            STATENEW(i,4)=epsS
            STATENEW(i,5)=B
            STATENEW(i,6)=ytri
            STATENEW(i,7)=epsPv
            STATENEW(i,8)=epsPs
            STATENEW(i,9)=epsEv
            STATENEW(i,10)=epsEs
            STATENEW(i,11)=epsPls(1)
            STATENEW(i,12)=epsPls(2)
            STATENEW(i,13)=epsPls(3)
            STATENEW(i,14)=epsPls(4)
c
100     continue
    End if
        Return
        End
```